Development of a thin scintillation counter hodoscope for detecting the lowest energy cosmic-ray antiprotons

Atsushi Horikoshi

Department of Physics, Osaka University

February, 2010

Development of a thin scintillation counter hodoscope for detecting the lowest energy cosmic-ray antiprotons

(低エネルギー宇宙線反陽子観測の為の薄型 TOF カウンターの開発)

Atsushi Horikoshi

Department of Physics, Osaka University
February, 2010

Development of a thin scintillation counter hodoscope for detecting the lowest energy cosmic-ray antiprotons

Atsushi Horikoshi

Department of Physics, Osaka University

February, 2010

Abstract

The BESS-Polar Experiment has been carried out to search for novel primary origin of cosmic-ray antiprotons with high statistics and high sensitivity for cosmic-ray antiprotons with a novel primary origin. Measurement in the low energy region is emphasized as this is the region where possible primary antiprotons are most easily distinguished from secondary antiprotons. The BESS-Polar spectrometer has been developed to realize long duration flight over Antarctica. A significant effort has been made minimize material thickness in the spectrometer in order to maximize the sensitivity in measurement of the low energy particles. A Middle Time-of-Flight (TOF) detector which has been newly introduced from BESS-Polar experiment has been indispensable to the detection of low energy cosmic-ray antiprotons until 0.1 GeV.

In the BESS-Polar I flight which was carried out in 2004, the performance of the Middle TOF was limited because of the single-sided readout. This in turn determines the lower energy limit of performance for the antiproton identification. Based on the result of the BESS-Polar I experiment, we newly developed the double-sided readout Middle TOF for the BESS-Polar II experiment. The difficulty in design and construction of the BESS-Polar Middle TOF mainly comes from the spatial restriction in the magnet bore. We carefully developed the double-sided readout Middle TOF for BESS-Polar II.

The BESS-Polar II experiment was carried out with a NASA long duration balloon flight over Antarctica in December 2007 through January 2008. The newly developed spectrometer enabled more than 20 days flight. During this successful flight, the BESS-Polar II superconducting spectrometer collected 4.7 billion cosmic-ray events without any online event selection cuts.

BESS-Polar II Middle TOF worked well during the flight. We acquired about five times the statistics, in the solar minimum period of BESS-Polar II, than that acquired by BESS-Polar I flight. The performance of the Middle TOF realized the improvement of the performance because of double-sided readout, and it has made an essential contribution to maximizing sensitivity of the BESS-Polar II spectrometer in the low energy region of 0.1 GeV.

Acknowledgments

I would like to express my great appreciation to Prof. Yoshitaka Kuno. He accepted and encouraged me to study cosmic-ray physics.

I would like to express gratitude to Prof. Akira Yamamoto and Prof. Koji Yoshimura for accepting my participation to the BESS-Polar II experiment.

I thank you for all people in BESS-Polar II group. All detectors are extremely beautiful and have high accuracy. The Upper and Lower TOF counters are developed by Dr. J.W. Mitchell, Dr. T. Hams and Ms. N. Thakur. The PMT housing of TOFs are carefully developed by Dr. R. Orito and Mr. Y. Matsukawa. The Aerogel Cherenkov Counter is developed by Mr. K. Sakai and Dr. M. Hasegawa with their great effort and careful investigations. The superconducting solenoid magnet has been realized with a lot of effort by Prof. Y. Makida and Ms. R Shinoda. The data acquisition system is developed by Dr. M. Sasaki and Mr. A. Kusumoto. The compact solar power system is developed and designed by Dr. M. Hasegawa and constructed by the effort of Mr. Y. Matukawa and everyone.

Middle TOF is developed by great support of everyone. Dr. Fuke introduced the detail of BESS-Polar I Middle TOF. Dr. R. Orito give me the various knowledges and advices about the basic structure of Middle TOF. About the spacing in the magnet bore and knowledge of quite many things, Dr. S. Matsuda helped me with great kindness. The structure of Middle TOF is consists of the advices of Mr. M. Gotou (G-tech) who has the great machining technique, and Mr. F. Sebastian who is the great teacher of machining and show me the most skillful machining technique. BESS-Polar II Middle TOF is realized by their support.

I thank you for Prof. A. Yamamoto, Prof. K. Yoshimura, Dr. M. Sasaki, Dr. M. Hasegawa, and Mr. K. Sakai about the analysis. They supported and introduced quite many scheme of analysis. The performance of Middle TOF is consists of their support.

I greatly appreciate helpful suggestions from Prof. J. Nishimura Prof. T. Yoshida, Prof. M. Nozaki, and Dr. S. Haino. It is a pleasure to express my appreciation to Dr .J. Ormes, Dr A. Moiseev, Dr R. Streitmatter, Dr J. Mitchell, Prof. T. Yamagami, and Dr .E. S. Seo, with whom I have been collaborating on the BESS-Polar experiment.

I also thank to our secretaries Ms. W. Oda, Ms. M. Torikoshi, Ms. S. Tanaka, Ms. E. Kotaki, and Ms. K. Nagai for their helpful and kind supports.

The BESS-Polar experiment is carried out as a Japan-U.S. collaboration, and supported by a Grant-in-Aid for Specially Promoted Research, in Japan, and by NASA in US. The balloon fight operation were carried out by Columbia Scientific Balloon Facility as part of the NASA's scientific balloon program. The activity in Antarctica was operated by the National Science Foundation, USA. I would like to express my sincere thanks for their continuous professional support, which was essential to realize this experiment in Antarctica.

Finally, I would like to express the special appreciation to my parents. I could complete my graduate course with their continuous support.

Contents

List of Figures

List of Tables

Chapter 1

Introduction

The measurement of cosmic-ray provides not only understanding of propagation [1], and acceleration of cosmic-rays in the galaxy but also offers the possibility of understanding the origin and early history of the Universe from a view point of elementary particle physics. The possible sources of cosmic-rays are novel process, such as evaporating primordial black holes (PBHs) [2] which are generated in the early Universe and the annihilation of neutralino dark matter [4, 5, 7].

A probe for such novel processes is to search for antiprotons, positrons and anti-matter nuclei which are heavier than antiprotons. Gamma-rays from antimatter annihilation might also provide a signature. The main component of antiprotons and positrons is expected to be secondary cosmic-rays which come from collisions of primary cosmic-rays with the interstellar matter. The production of low energy secondary antiprotons whose kinetic energy is lower than 1 GeV is strongly restricted by the kinematics [8–10]. On the other hand, the energy spectra of primary antiprotons is expected to peak lower than 1 GeV [11]. From these reasons, the measurement of low energy cosmic-ray antiprotons is expected to be an effective probe for the primary sources.

1.1 BESS-Polar project

The Balloon-borne Experiment with a Superconducting Spectrometer, BESS, has been carried out as a US-Japan scientific balloon program since 1993. It aims at studying elementary particle phenomena in the early history of the universe. It also provides very precise measurements of absolute fluxes of cosmic-rays as fundamental references in cosmic-ray physics.

The BESS experiments previous to the BESS-Polar experiment reduced the systematic errors by the annual improvement of detectors and beam test of the entire spectrometer [12]. Because the systematic errors were thus well reduced, the requirement of further precise measurement of antiprotons by subsequent BESS experiment simplified to "improvement of the statistics with long duration flight" and "enhancement of sensitivity for the low energy antiprotons" whose energy region is expected to be that of the primary sources.

From these purposes, the BESS-Polar program was proposed [13–15]. The BESS flight in Antarctica gives long duration balloon flight with high sensitivity in low energy region below ~0.3 GV. The wind over Antarctica circulated around the South Pole. This allows the long duration balloon flights over 20 days. To realize the long duration flight over Antarctica, the experiment is equipped with new systems such as the long life solenoid magnet [16] and the solar battery system. Furthermore, to enhance the sensitivity for low energy region, the material thickness is reduced as low as possible. The improvements for the reduction of material thickness are the development of extremely thin wall superconducting magnet, the removal of outer pressure vessel, and the addition of new TOF counter which is called "Middle TOF". The Middle TOF is placed just under central trackers in the magnet bore. It makes the detection of the low energy cosmic-rays which cannot reach Lower TOF. Figure 1.1 shows the comparison of the previous BESS spectrometer and the BESS-Polar spectrometer. The detectable lowest kinetic energy of the previous BESS experiment is 0.18 GeV [17]. The detectable lowest kinetic energy of BESS-Polar experiment by the trigger of Upper TOF and Middle TOF is 0.1 GeV [18]. To enhance the sensitivity for low energy antiprotons, the Middle TOF is "indispensable" detector for BESS-Polar spectrometer.

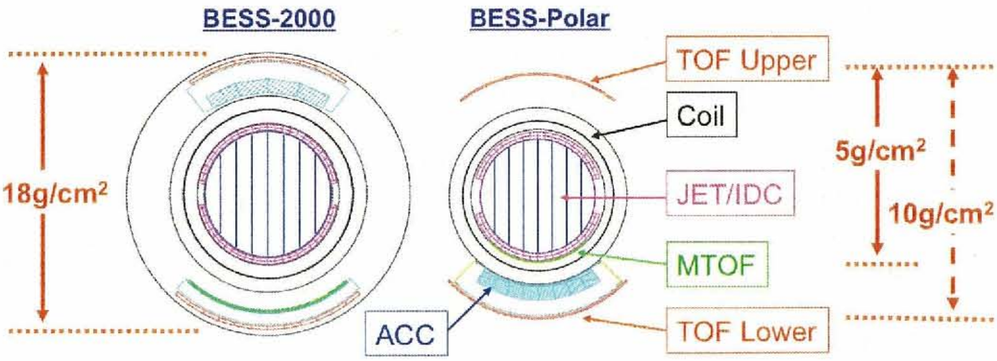

Figure 1.1: Cross sectional view of the BESS (left) and BESS-Polar (right) spectrometer.

Figure 1.2 shows the energy spectra of BESS95+97 [19] around the previous solar minimum and the expected energy spectra by BESS-Polar II experiment.

The energy spectra of BESS-Polar experiment is expected to be the precise measurement with high statistics and high sensitivity for low energy region which comes from the contribution of Middle TOF. The difference of energy spectra between only secondary sources and secondary + primary sources is very large for low energy region.

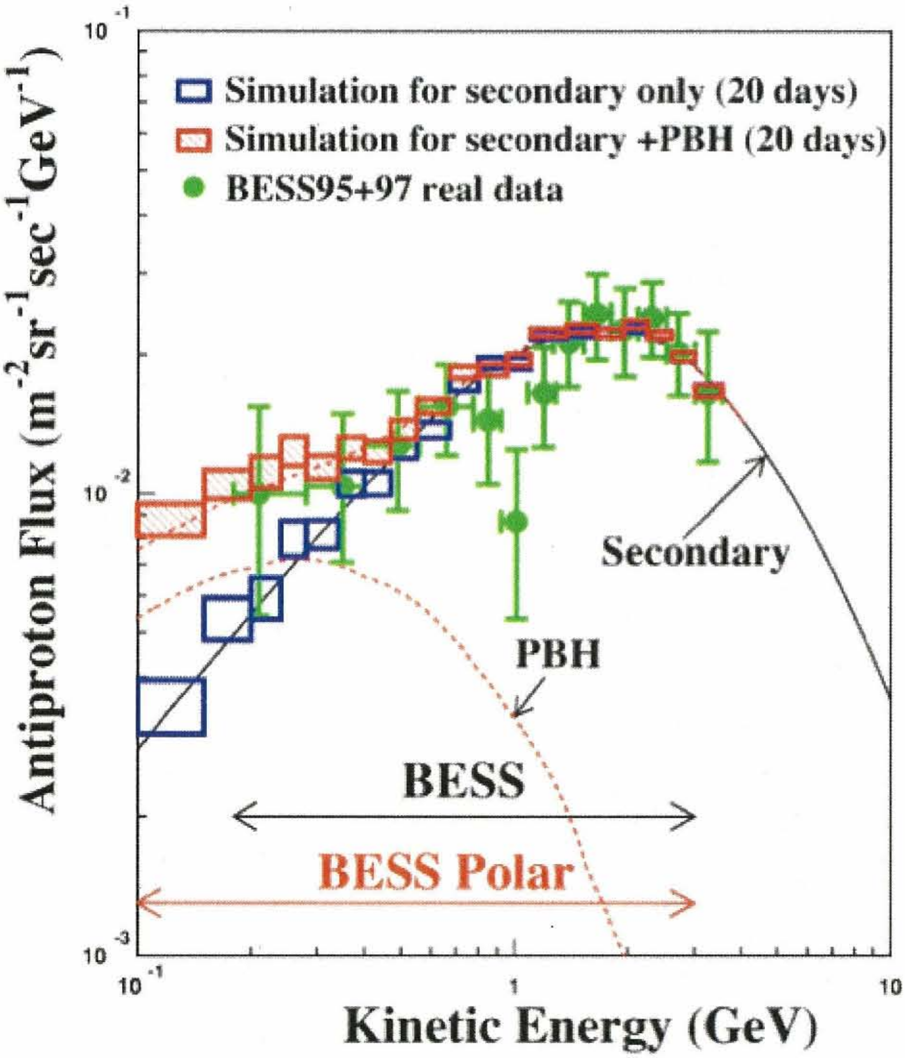

Figure 1.2: The expected energy spectra of BESS-Polar experiment together with the previous BESS antiproton spectra at the previous solar minimum period (1995+1997) [19]. The solid line indicates the theoretical calculation of secondary antiprotons. The dashed line shows the theoretical calculation of primary antiprotons.

1.2 Performance limited with BESS-Polar I Middle TOF

The BESS-Polar project consists of two flights. The BESS-Polar I experiment was successfully carried out in 2004 [20]. The BESS-Polar I Middle TOF used a single-sided readout because of the strong spatial restriction. The single-sided readout Middle TOF limited performance and event quality. Figure 1.3 shows the time resolution of BESS-Polar I Middle TOF. The time resolution of BESS-Polar I Middle TOF changes from 300 ps to 650 ps depend on the axial position. The upper limit of antiproton identification is limited by $1/\beta$ which is calculated by the Time-of-Flight. Therefore, the upper limit of antiproton identification is determined by the time resolution of Upper TOF and Middle TOF. In BESS-Polar I, the upper limit of antiproton identification is about 0.65 GV.

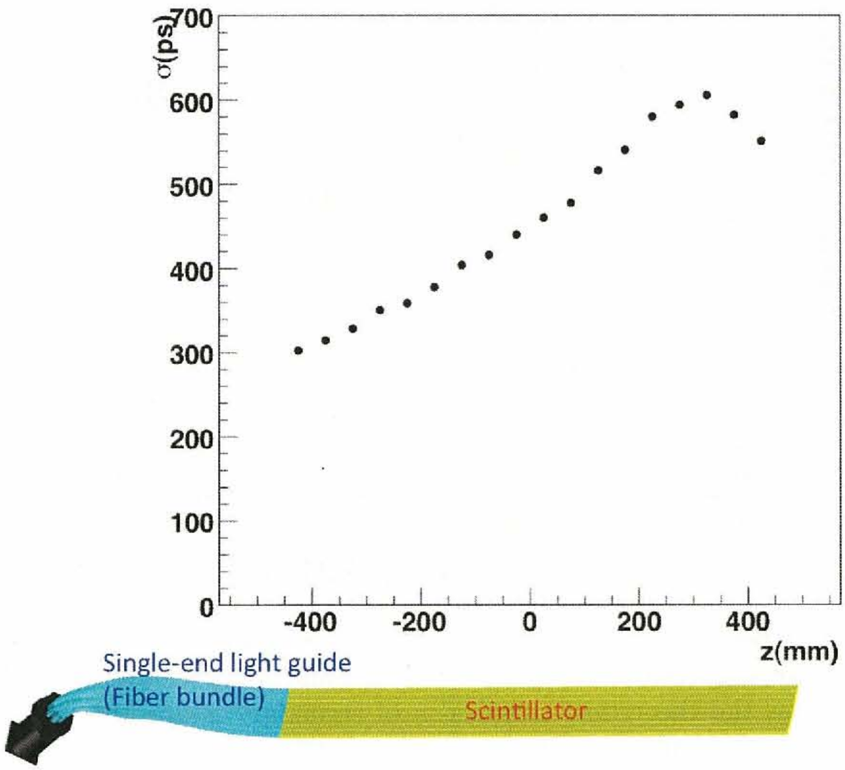

Figure 1.3: The time resolution of BESS-Polar I Middle TOF depends on the axial position.

In the BESS-Polar spectrometer, the track of cosmic-ray is reconstructed by the tracker. To keep the quality of the track reconstruction, we check the consistency of the hit information from the tracker and hit position from TOF counters. For the axial hit position, the hit position from TOF counter is calculated by the time information of double-sided readout. Therefore, the BESS-Polar I Middle TOF cannot acquire the axial hit position information because the BESS-Polar I Middle TOF is single-sided readout. In the BESS-Polar spectrometer, the track consistency of the axial position is very important to keep the event quality. Figure 1.4 shows the particle identification plot by the Upper TOF and the Middle TOF.

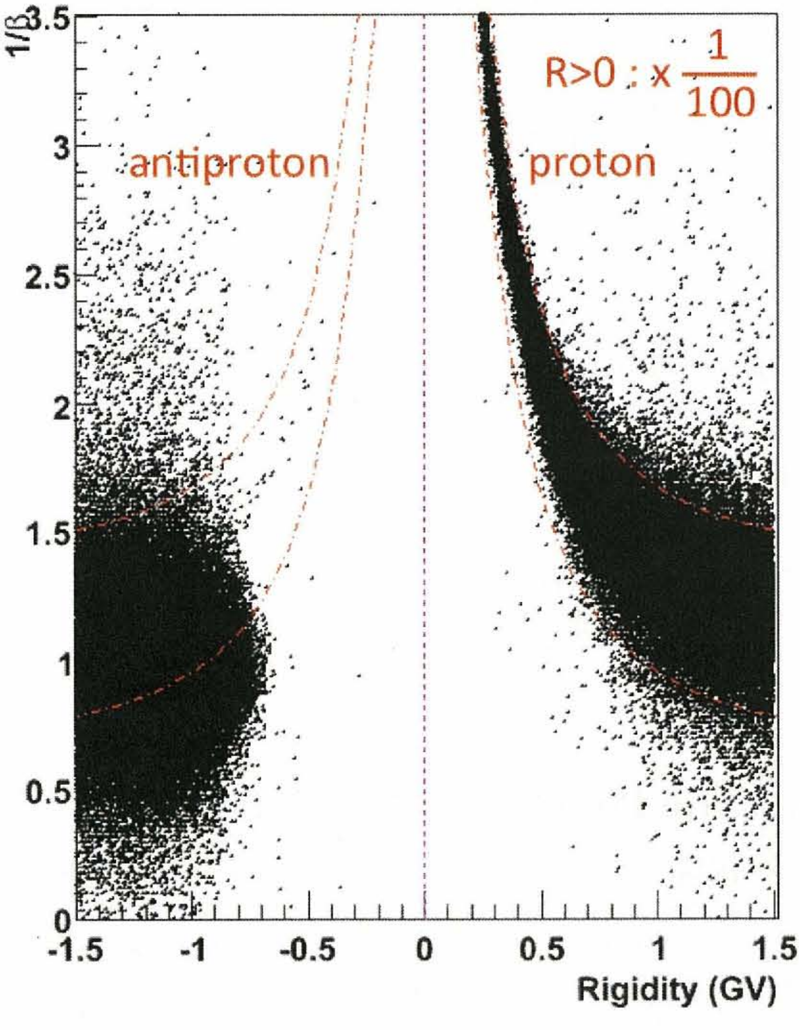

Figure 1.4: The particle identification plot of BESS-Polar I by Upper TOF and Middle TOF. In this ID-plot, the positive charge particles (R > 0) are selected once every 100 events. There are noise event outside of particle identification band.

There are events which exceed the light speed ($1/\beta < 0.5$). It is very difficult to guess the reason of these events. However, such kind of events come from the measurement of Time-of-Flight. One of the candidate of the mistake is the noise trigger event. If there are the noise trigger event before the signal, the hit time of Middle TOF is much faster than actual hit time. It makes the very fast velocity which exceed the light speed. If the Middle TOF is double-sided readout, such kind of events are clearly excluded by the consistency of the axial hit position between the tracker and TOF counters.

To realize more precise measurements with Middle TOF, the double-sided readout Middle TOF was desired. Based on the experience of BESS-Polar I experiment, each component of the BESS-Polar II spectrometer has been improved or newly developed [21]. The development of double-sided readout Middle TOF for BESS-Polar II is one of the most important improvement of the BESS-Polar II spectrometer.

All detector which are loaded in BESS-Polar II spectrometer have been improved or newly developed to enhance the performance. Table 1.1 shows the list of improvement about each detectors.

Table 1.1: The performance of the BESS-Polar I and the BESS-Polar II detectors. All detectors have been improved or newly developed to enahance the performance.

	BESS-Polar I	BESS-Polar II
JET/IDC (improvement)		
r-ϕ	119 μm	116 μm
z	45 mm	25 mm
Upper/Lower TOF	156 ps	120 ps
Middle TOF	445 ps	306 ps
ACC	6 photo-electron	11 photo-electron

Upgrading Middle TOF in BESS-Polar II

I joined the BESS-Polar II team from the beginning of the BESS-Polar II experiment. My main contribution is the development of BESS-Polar II Middle TOF. I also contributed to the construction of BESS-Polar II spectrometer, compatibility test, balloon flight over the Antarctica, and the data analysis with Middle TOF.

Chapter 2 gives the physics motivation of the BESS-Polar II experiment. Chapter 3 gives a brief description of BESS-Polar spectrometer. Chapter 4 gives the development of BESS-Polar II Middle TOF. Chapter 5 describes the balloon flight over Antarctica. Chapter 6 gives the detector performance of Middle TOF using the flight data. Chapter 7 is the discussion of the performance. Chapter 8 is the conclusion of the development of BESS-Polar II Middle TOF.

Chapter 2

Physics motivation

The measurement of cosmic-rays can be a good probe to investigate phenomenon in the early Universe such as primordial black holes (PBHs), the annihilation of neutralinos which is predicted by Supersymmetry (SUSY), and the possible existence of antimatter Galaxies with heavy anti-matter.

The BESS experiment has high sensitivity for such kinds of novel process physics. In this chapter, we concentrate on the PBHs which correspond to the main physics motivation of BESS-Polar II experiment [3].

2.1 Search for Primary Antiprotons in Cosmic-rays

The PBHs, which are thought to be formed from density fluctuations during the radiation dominant era of the early Universe, may be a useful tool offering clues about the early Universe. The PBHs typically have masses much smaller than astrophysical holes thereby acquiring high enough Hawking temperature to emit various cosmic-rays through the Hawking process [2], possibly yielding an observable effect.

The expected spectrum of primary antiprotons has been calculated with several methods and propagation models. Basically all the results expect the 'soft' spectra extending toward the low energy with a peak around 0.2 GeV, as shown in Figure 2.1 [5]. Thus, if they exist, the contribution of primary antiprotons can be seen in the spectrum of low energy region as an excess of the flux.

The primary antiprotons are stored in the Galaxy for $10^7 \sim 10^8$ year because of the turbulent magnetic field in the Galaxy. Therefore antiprotons are the good probe to search for the primary source.

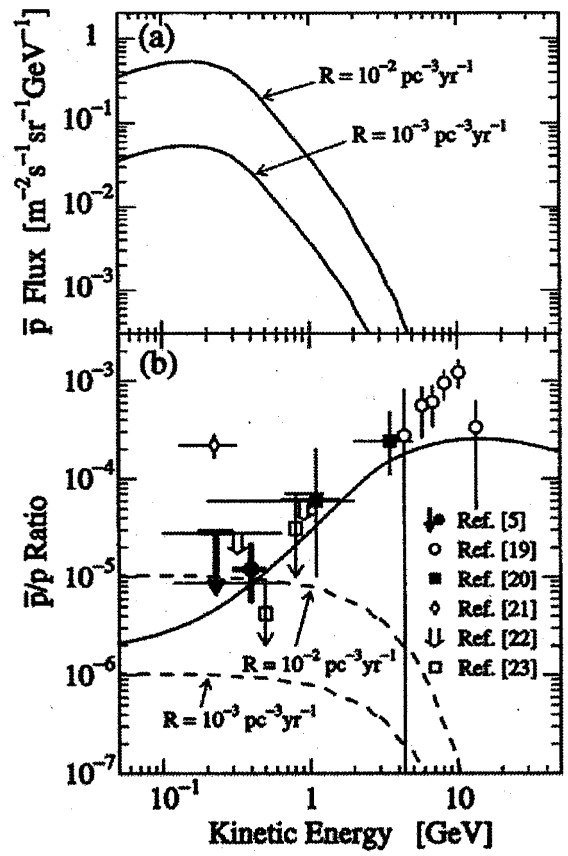

Figure 2.1: (top) The expected flux of primary antiprotons and (bottom) antiproton/proton ratio [5]. R is the evaporation rate of PBHs.

On the other hand, the flux of secondary antiprotons is constrained by the kinematics. The production of secondary antiprotons requires high energies. The secondary antiprotons are produced through the following reactions.

$$
\begin{aligned}
p_{\text{cosmic-ray}} + p_{\text{gas}} &\rightarrow \overline{p} + X \\
p_{\text{cosmic-ray}} + p_{\text{gas}} &\rightarrow \overline{n} + X, \\
&\qquad\quad \overline{n} \rightarrow \overline{p} + e^{+} + \nu_e
\end{aligned}
$$

where X represents other particles which emerge with antiproton from the interaction. The minimum threshold comes from kinematic constrains of the following process.

$$pp \rightarrow ppp\overline{p}$$

The center of mass threshold for antiproton production is

$$E_{\text{th}} = 4m_p/2 = 2m_p$$

The threshold energy of laboratory system E'_{th} is calculated by Lorenz invariance

$$m_p E'_{\text{th}} = E^2_{\text{th}} + |\overrightarrow{p}|^2 = 7m_p^2$$

$E'_{\text{th}} = 7m_p \approx$6.5 GeV is the minimum threshold energy that incident proton must have in the laboratory system to produce an antiproton. The kinetic energy of the antiproton could be lower than 1 GeV in the laboratory system when the cosmic-ray proton has a higher energy and the antiproton is produced in the backward direction to the incoming cosmic-ray proton in the center of mass system. However the probability of this state is reduced by its small phase space factor in antiproton production.

The source spectrum of secondary antiprotons is expected to have a peak around 2 GeV and decline steeply on both side of energy as shown in Figure 2.2 [8]. This peak structure is obtained by the combination of antiproton production kinematics and power low spectra ($\propto E^{-2.7}$) of primary protons. If there are the contributions of primary antiprotons, we can measure the excess of flux comparing with secondary model as shown in Figure 1.2 because the flux of primary antiprotons is expected around 0.2 GeV.

However, the low energy antiprotons are strongly affected by the out flowing solar wind. The strength of the flux is strongly depends on the solar modulation. The intensity of low energy cosmic-ray is the highest during the solar minimum whose cycle is 11 years. Thus, the chance of the investigation of primary antiprotons should be only enhanced in once in every 11 year period.

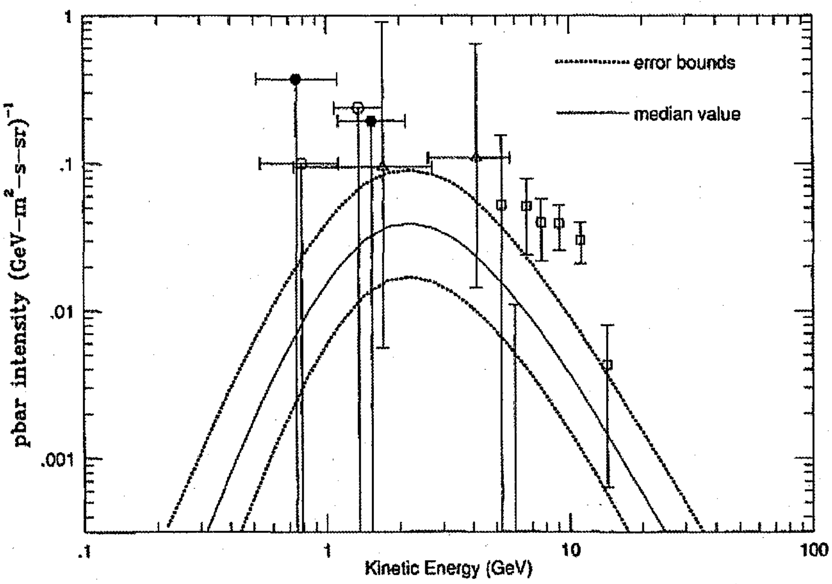

Figure 2.2: The calculated flux of secondary antiprotons and experimental results before the BESS experiment. The peak of secondary flux is expected around 2 GeV. (filled-circle) upper limit of antiprotons with PBAR experiment (1990), (open-circle) LEAP experiment (1990), and (triangle) Bogomolov (1987) and (square) Golden (1984).

2.2 Precise Measurement of primary antiprotons with BESS-Polar Experiments

To investigate primary antiprotons, the BESS-Polar project was planned. The BESS-Polar experiment provides the precise measurement of antiprotons with long duration balloon flight as described in Chapter 1. If there are primary antiprotons, the flux during solar minimum should have an enhancement around low energy region compared to the flux before the solar minimum. Thus, the BESS-Polar project consists of two experiments to compare the difference of flux before the solar minimum and during the solar minimum.

1. Before the solar minimum

   The BESS-Polar I experiment (2004-2005) was carried out before the solar minimum. The solar activity before the solar minimum restricts all low energy antiprotons, making it difficult to distinguish any excess flux due to primary antiprotons. Nonetheless, making reasonable assumptions about the solar activity, a calculation may be made of the expected flux for both the case of all secondary antiprotons and the case of both secondary plus primary antiprotons as shown in Figure 2.3.

2. During the solar minimum

   On the other hand, the BESS-Polar II experiment was carried out during the solar minimum (2007-2008). If we acquire the flatter antiproton spectra compare to BESS-Polar I result, we can estimate the contribution of primary antiprotons.

Figure 2.3 [27] shows the results of previous BESS experiment and BESS-Polar I experiment with the theoretical models. The result of BESS 95+95 shows the flatter energy spectra at the low energy region compared to secondary models. However, the data around low energy region has large errors which come from the statistics. On the other hand, the result of BESS-Polar I is consistent with the secondary model.

The lowest energy of BESS-Polar I result extends down to $\sim$0.1 GV because there is Middle TOF in BESS-Polar I spectrometer. The difference of the antiproton spectra between secondary and primary + secondary is very large at the low energy region. Thus, Middle TOF is indispensable for the investigation of primary antiprotons.

The measurement of cosmic-ray antiprotons during the solar minimum is very important as shown in these results. Thus, the BESS-Polar II experiment during the solar minimum is the most important for the investigation of primary antiprotons.

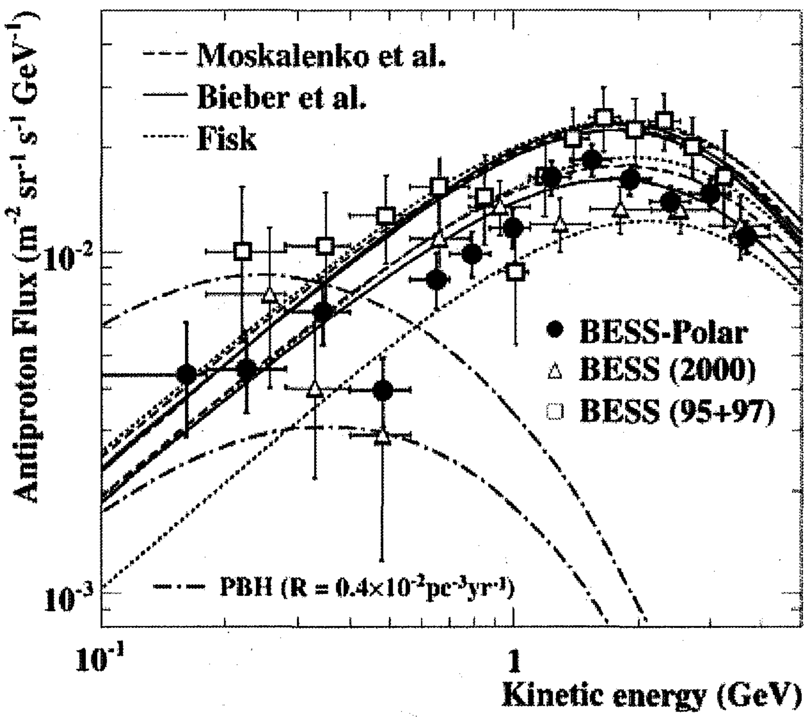

Figure 2.3: The measurements by BESS at several different solar modulations. BESS 95+97 [19] : previous solar minimum, BESS-Polar I (2004) [27] : before the solar minimum. The antiproton spectra of the BESS-Polar I reaches down to ~0.1 GeV because Middle TOF can acquire the low energy particles. The dash-dot curves are calculations of antiproton spectra from the evaporation of PBHs with the effect of solar modulation during each flight. The antiproton spectra is expected to enhance during the solar minimum.

2.3 Features of BESS-Polar experiment compared with other experiments

The BESS-Polar experiment is unique and complementary to two space experiments, PAMELA and AMS. The PAMELA spectrometer was launched on a satellite in near-polar orbit in June, 2006. Therefore, the PAMELA experiment also samples ranges of geomagnetic cutoff similar to the BESS-Polar experiment, but because the geometry factor of PAMELA spectrometer is limited to be ~ 21 cm^2 sr, BESS-Polar experiment has great advantage at low energies by about an order of magnitude.

The AMS experiment is in preparation for a long term observation on the International Space Station (ISS). The AMS spectrometer has a similar geometrical acceptance to BESS-Polar spectrometer and may have the major advantage of an exposure as long as three years on the ISS. However, a strong constraint is the flight profile of 0$\sim$52 degrees in latitude in comparison with the BESS profile staying at $\sim$80 degrees. Figure 2.4 shows the comparison of orbit and the exposure sensitivity (defined by geometrical acceptance $\times$ exposure time) of the BESS-Polar experiment as a function of the energy in comparison with those for the PAMELA experiment and the AMS experiment. Thus a 20-days BESS-Polar II flight would exceed the sensitivity of AMS experiment for antiproton energies below $\sim$ 250 MeV. Table 2.1 shows the BESS-Polar experiment in comparison with the PAMELA experiment and the AMS experiment.

In the next chapter, we will describe the BESS-Polar II detector in detail.

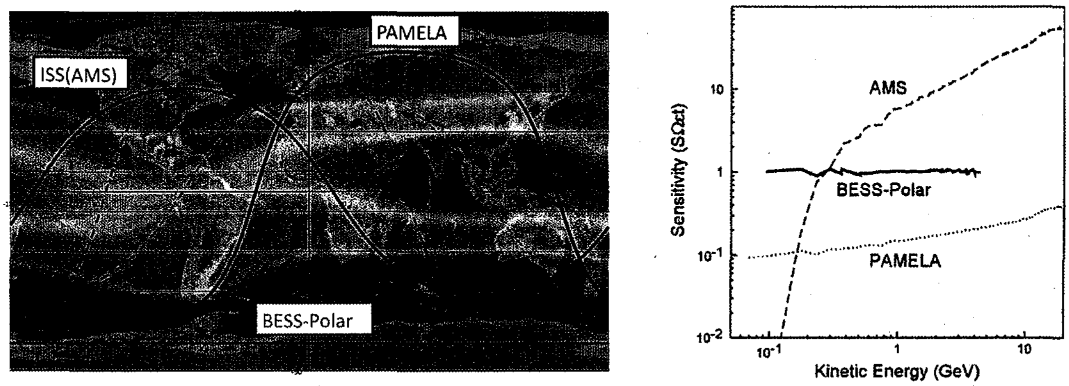

Figure 2.4: (left) Flight profiles of BESS-Polar, AMS on the Space Station and PAMELA on a polar orbit with rigidity cut-off distribution. (right) Sensitivity for antiprotons for each experiment.

Table 2.1: The BESS-Polar experiment in comparison with the PAMELA and AMS.

Project	BESS-Polar	PAMELA	AMS
Geometrical acceptance	$\sim$0.27 m^{2}sr	$\sim$0.0021 m^{2}sr	$\sim$0.3 m^{2}sr
Max. detectable rigidity	$\sim$270GV	$\sim$385GV	$\sim$1TV
Flight duration	8.5 + 24.5 days	>3.5 years	$\sim$3 years
Flight altitude	36 km	690 km	320$\sim$390 km
Residual air	$\sim$6 g/cm^2	-	-
Flight latitude	$\sim$80 degrees	$\sim$+/- 80 deg.	$\sim$+/- 51.7 deg.
Energy region	0.1$\sim$4GeV	>0.1GeV	>0.5 GeV
Flight vehicle	Balloon	Satellite	Space Station
Launch	2004, 2007	2006 (still working)	2010

Chapter 3

BESS-Polar II detector and Middle TOF

This chapter provides an short description of the BESS-Polar II spectrometer. The detail overview of BESS-Polar II spectrometer is shown in Appendix B. In order to realize long duration and precise measurement over Antarctica, almost all of the BESS-Polar II detector is newly developed [21]. We use hereafter a cylindrical coordinate system : r, ϕ, and z, and a Cartesian coordinate x, y, z, where y and z are the vertical axis and the axis of the solenoid, respectively.

3.1 Overview of BESS-Polar II detector

The detector components are arranged concentrically as shown in Figure 3.1. A particle traversing the apparatus passes through, from outside to inside, the upper plastic scintillator hodoscope (Upper TOF), a superconducting solenoid (MAG), two layers of inner drift chambers (IDC), before entering a central jet-type drift chamber (JET). An aerogel Cherenkov

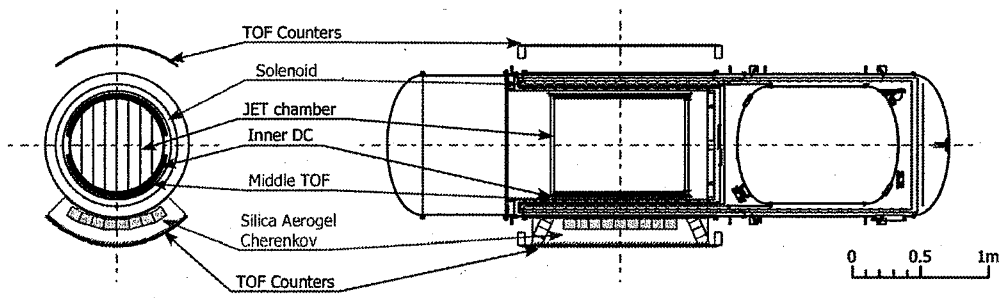

Figure 3.1: Cross sectional view of BESS-Polar II spectrometer

counter (ACC) sits between cryostat and the lower TOF hodoscopes (Lower TOF). Furthermore, the Middle TOF is placed between lower IDC and the magnet bore for the detection of the lowest energy particle. Among these components, the JET/IDC, and the Middle TOF are contained in a magnet whose wall is also used as the pressure vessel. The Upper and Lower TOF and the ACC are placed outside of the pressure vessel, i.e., in the vacuum during the flight.

The most distinctive feature of the BESS-Polar II detector is the cylindrical configuration with a solenoid magnet. Solenoid magnet configuration has been disfavored in previous cosmic-ray experiments because of the unavoidable material in the particle passage. However, a thin superconducting solenoid developed at KEK enabled us to adopt this concentric configuration, which has many advantages in application to the cosmic-ray measurements, as well as in the high energy collider experiments.

This cylindrical configuration gives a large geometrical acceptance while keeping the whole detector size compact. The uniform magnetic field of 0.8 T over the large tracking volumes assures an almost constant geometrical acceptance for a wide energy region. The acceptance changes only a few percent from the lowest detectable energy ($\sim$ 100 MeV) up to greater than 100 GeV. A large and transparent tracking system can be installed inside the solenoid. This tracking system can fully 'visualize' the incident track or any interaction inside the apparatus (Figure 3.3). The detector performance changes little for various hit positions and incident angles. This characteristic is essential in the reliable determination of the absolute flux of the cosmic radiation.

Figure 3.2 shows the BESS-Polar DAQ system [34]. The time-to-digital converter and discriminator modules (TDC/Discriminator) discriminate signals from the Upper/Lower TOF and the Middle TOF, and send hit patterns of those detectors to a trigger boards. The trigger board generates event trigger in accordance with those hit patterns. A trigger signal is sent to all other modules to start data digitization. Charge of incident particles in the Upper TOF, the Lower TOF, the ACC, and the Middle TOF are digitized by charge-to-digital converter (QDC) modules.

These modules (TDC/Discriminator, QDC, and Trigger) have a digital signal processor (DSP) units on each board (TI TMS320) so that they can individually proceed digitization processes and prepare for the next trigger.

All data from these modules are assembled by MU2 (McBSP to USB 2.0 converter) modules. A MU2 module receives data from DSPs via multichannel buffered serial ports (McBSPs), and then transmit them to the data processing part via USB 2.0. Data from JET/IDC are sent to FADC modules [35] and sent to the next data processing part.

Acquired data from MU2 and FADC are processed by DAQ programs on the Compact-PCI boards, and in here the event data are finally constructed. All cosmic-ray event data which issue trigger during the flight are stored on 16 hard disk drives, with a capacity of 1 TB. Compact- PCI boards are also connected to the following communication boards by TCP/IP to transfer some event data to the ground station.

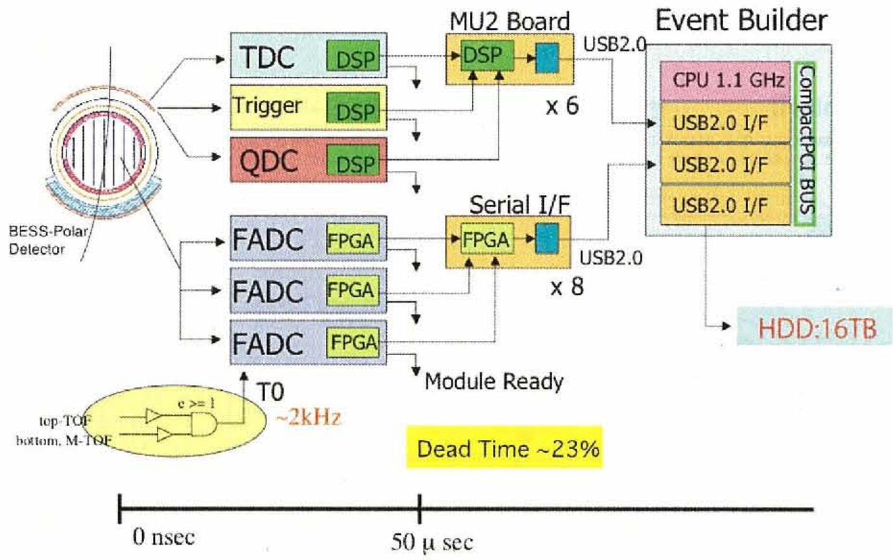

Figure 3.2: Block diagram of the BESS-Polar II DAQ system.

3.2 Time of Flight measurements

Particle identification in the BESS-Polar experiment is performed by mass reconstruction according to the relation

$$m = ZeR\sqrt{1/\beta^2 - 1}$$

The rigidity, momentum per charge (R≡pc/Ze), is precisely measured by the reconstructed particle trajectory. The velocity, β, is derived from the path length and the time-of-flight between the Upper TOF and the Lower/Middle TOF. The energy deposit in the TOFs provides the magnitude of the charge, Z, and additional information on the velocity according to the relation.

$$dE/dx \approx (Ze/\beta)^2 f(\beta)$$

The sign of charge is determined by the deflection measured by the JET/IDC and the particle direction, up-going or down-going, determined by the TOF. The mass is finally calculated from these measurements. From next section, we introduce how to acquire these information from TOFs. At first, we describe the structure of each TOF. After that, we describe how to acquire the time-of-flight and energy loss from TOFs.

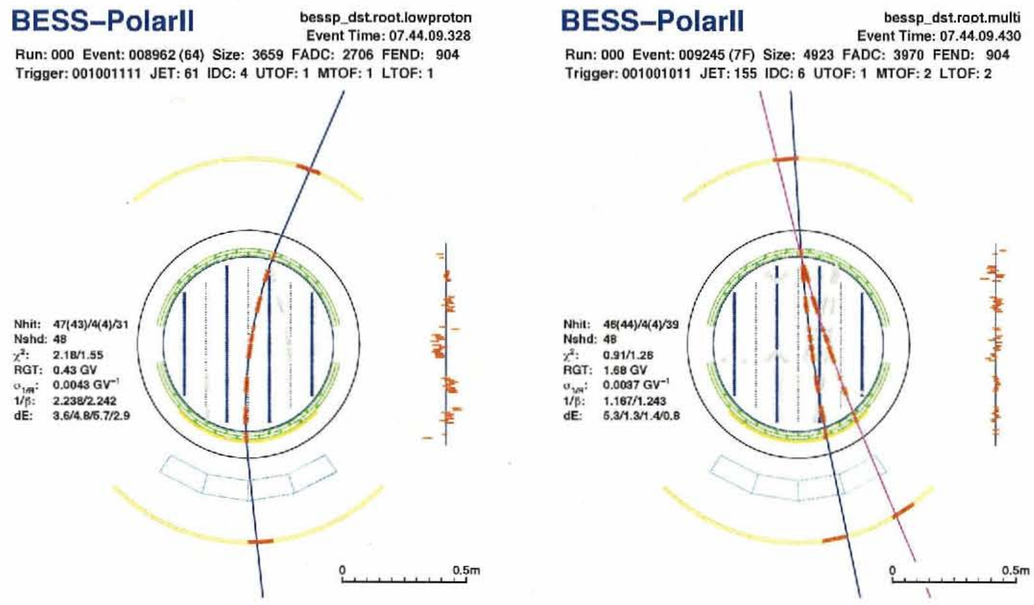

Figure 3.3: Examples of event display collected during the flight. left : a typical single-track event. right : two-track event showing the interaction.

3.3 Upper and Lower TOF

In this section, we describe the Upper TOF and the Lower TOF [28]. The Upper TOF and the Lower TOF consist of ten upper- and twelve lower- plastic scintillation counter paddles (945 × 100 × 12 mm, Eljen EJ-204). A light guide (Figure 3.4) made of UV-transparent acrylic plate (Mitsubishi Rayon) is affixed to the scintillator connecting each end of a counter to a 2.5-inch fine-mesh magnetic-field-resistant photomultiplier tube (FM-PMTs), i.e., a Hamamatsu R6504S assembly type. To minimize the loss of photo-electrons in the PMT caused by the magnetic-field, PMTs are placed tangential to the acrylic plate such that the angle between their axis and magnetic field lines is minimized.

The 2.5-inch FM-PMT (Hamamatsu R6504S) has the bi-alkali (Sb-Rb-Cs, Sb-K-Cs) photocathode of which the effective diameter is typically 52 mm. Electrons are accelerated by parallel electric fields between the dynodes; hence allowing the device to be used in a magnetic field if the direction of the magnetic field is parallel to the PMTs longitudinal axis. PMT and counters itself were placed in the vacuum since BESS-Polar spectrometer had no outer pressure vessel [29]. The signal from the anode provides timing information and those from 13th and 18th dynodes are used to obtain the energy loss (dE/dx) of incident particles.

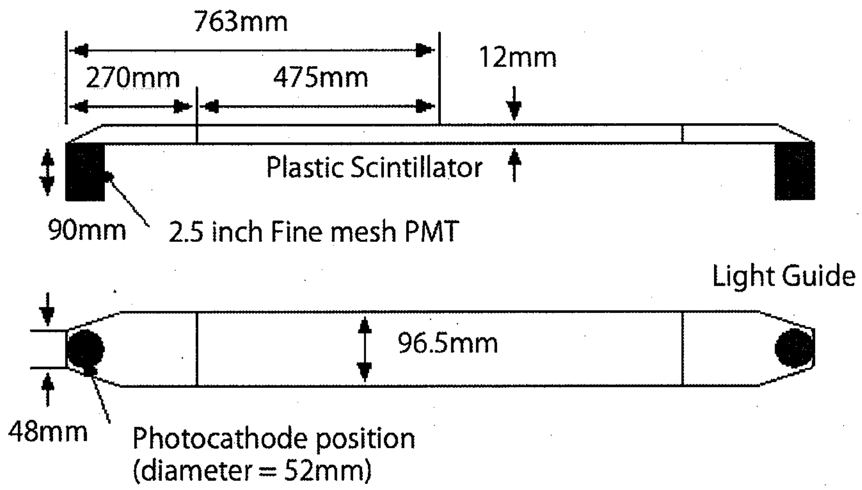

Figure 3.4: Overview of the Upper TOF and the Lower TOF.

3.4 Middle TOF

In addition to the Upper and the Lower TOF, a newly developed thin detector, the Middle TOF is installed on the lower half of the solenoid bore to the detection of low energy particles. The Middle TOF consists of 48 plastic scintillator bars. Each bar has a cross section of 5.6 $\times$ 13.3 mm read by eight anode photomultipliers (Hamamatsu R6504MODX-M8) through light guide of clear fiber (KURARAY CLEAR-PS 1.0 mm SQ) from double-sided. Figure 3.5 shows the overview of BESS-Polar II the Middle TOF. The length of BESS-Polar II light guide are 700 mm and 3000 mm. The structure of the BESS-Polar II Middle TOF comes from the spatial restrictions and the scheme of installation. The detail and development of the Middle TOF will be described in Chapter 4.

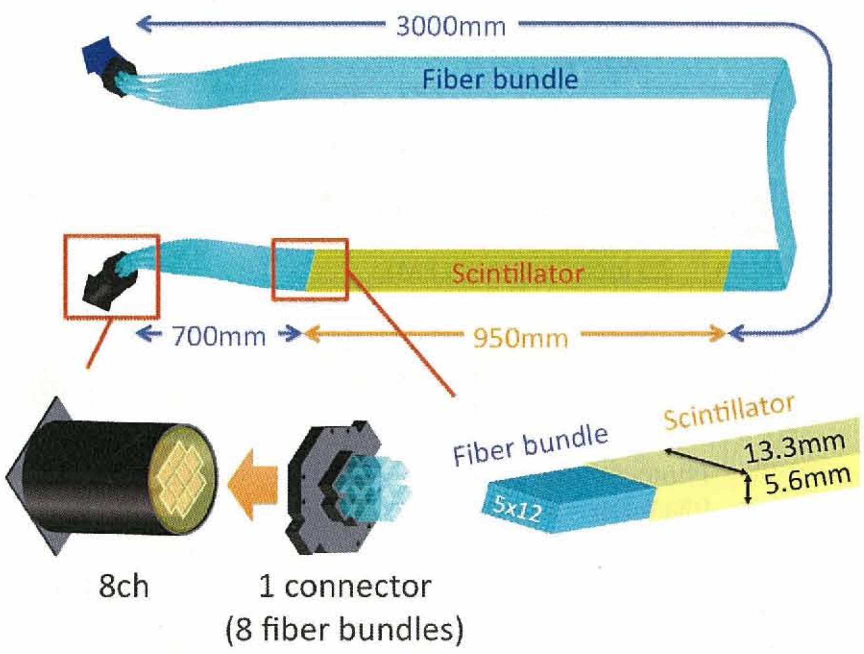

Figure 3.5: The overview of the BESS-Polar II Middle TOF. The 8 fiber bundles coming from the scintillator strips are joined in one connector which attaches to the PMT. The total length of the Middle TOF is 4.65m.

3.5 Signal Processing of TOFs

The output signals from each TOF are used for two different purposes: timing measurement and charge measurement. These measurement are used to reconstruct the mass of particle as described in section 3.2. To avoid the interference in the electronics with each other, three signals extracted from the anode and dynodes were utilized for the above purposes, respectively.

The signal processing of the Upper/Lower TOF and the Middle TOF are different because of the difference of PMT. The PMT of the Middle TOF is 8 channel multi-anode PMT.

3.5.1 Signal Processing of Upper and Lower TOF

1. The measurement of time-of-flight

   The anode signals are used to issue START pulses for timing measurements, because they have the largest pulses suitable for the discrimination. The time-to-digital converter (TDC) incorporate fast discriminators and common-stop time digitizers directly coupled to the anodes of PMT and measure arrival time of signals from TOF. The threshold levels were set to 12 mV, that are about 1/60 compared to the anode pulse-heights of minimum ionizing particles (MIPs). TDC modules had a full range of 150 nanoseconds and a resolution of better than 43 picoseconds.

2. The measurement of dE/dx with TOF

   Every 13th and 18th dynodes signal is distributed, to the charge-to-digital converters (QDC), and integral charge of them were measured.

3.5.2 Signal Processing of the Middle TOF

1. The measurement of time-of-flight

   The 19th dynode signals are used to TDC to save the power consumption of electronics for the Middle TOF. The dynode is common channel in PMT. The dynode signals are coupled to TDC modules through an inverting amplifier with a gain of ten and bandwidth of more than 1 GHz. The threshold levels are set to 160 mV, that are about 5 % compared to the dynode pulse-heights of MIPs.

2. The measurement of dE/dx with TOF

   The PMT of the Middle TOF have 8 channel anode. The anode signals is used to the QDC. The hit channel of the Middle TOF is selected by the QDC value from 8 channels of PMT.

Table 3.1 shows the summary of signal processing for TOFs.

Table 3.1: Summary of signal processing of TOFs.

	Upper/Lower TOF	Middle TOF
PMT	single-anode single-dynode	8 channel multi-anode single-dynode
TDC	anode 1ch for 1 paddle	19th dynode + 10×amplifier 1ch for 8 paddle
QDC	13th and 18th dynode 1 ch for 1 paddle	anode 1 ch for 1 paddle

3.6 Method of timing measurement

We discuss here on the hit time of a particle and time-of-flight, i.e., its difference between the Upper TOF and the Middle TOF of the BESS spectrometer including the details of their deriving processes. In the following discussion, PMTs number are assigned 1 to 4 as shown in Figure 3.6.

PMT signals have the time jitter associated with pulse heights, so called the 'time-walk' effect [30, 31]. Therefore, the measured TDC time must be corrected for the time-walk effect (the time-walk correction). The time-walk corrected timing for PMT i, t_{ic} is expressed as,

$$t_{\rm ic} = t_i - W_i/\sqrt{q_i} \tag{3.1}$$

where t_i, q_i and W_i are respectively the measured TDC time, the measured charge of the PMT signal, and a correction parameter fitted from data. Using the time-walk corrected timings for each PMT, we then define the hit time based on the hit position and the timing information. The hit position of the counter is defined using z coordinate along the counter's longitudinal direction as shown in Figure 3.6 where the counter center is defined as $z = 0$. The hit time of a particle in this paper is the timing based on the reference timing, T_{ref} which is subtracted as the offset timing and determined by the TDC common stop. We define the hit time for PMT1,2(3,4) of a counter, $T_{1(3)}(z)$ and $T_{2(4)}(z)$ to be

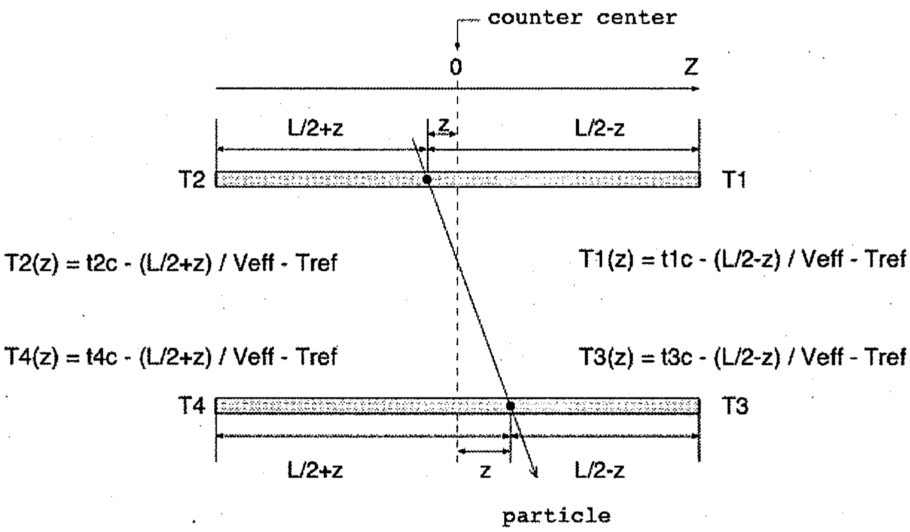

Figure 3.6: The definition of z coordinate and hit time.

$$T_{1(3)}(z) = t_{1c(3c)} - \left(\frac{L}{2} - z\right)/V_{\text{eff}} - T_{\text{ref}} \tag{3.2}$$

$$T_{2(4)}(z) = t_{2c(4c)} - \left(\frac{L}{2} + z\right)/V_{\text{eff}} - T_{\text{ref}} \tag{3.3}$$

where $t_{1c\sim 4c}$, and T_{ref} are respectively the time-walk corrected timings, reference timings; while z is the hit position of the counter, L the length of the scintillator, and V_{eff} the effective velocity of light in the scintillator. The measured rms of $T_{1(3)}(z)$ and $T_{2(4)}(z)$ are denoted as $\sigma_{1(3)}(z)$, $\sigma_{2(4)}(z)$, respectively. We use $1/\sigma_{1(3)}(z)^2$ and $1/\sigma_{2(4)}(z)^2$ as the weight of the combination of $T_{1(3)}(z)$ and $T_{2(4)}(z)$, respectively, for hit time measurements.

We then construct the weighted average [32] of hit time measurements, $T_{w.a}(z)$ as follows:

$$T_{\text{w.a}}(z) \equiv \frac{T_{1(3)}(z)/\sigma_{1(3)}(z)^2 + T_{2(4)}(z)/\sigma_{2(4)}(z)^2}{1/\sigma_{1(3)}(z)^2 + 1/\sigma_{2(4)}(z)^2} \tag{3.4}$$

The resolution of weight average of time measurements are better than normal average of hit time measurement, T_{ave}:

$$T_{\text{ave}}(z) \equiv \frac{T_{1(3)}(z) + T_{2(4)}(z)}{2} \tag{3.5}$$

The difference of resolution will described in Section 6.1. For the Upper TOF and the Middle TOF of the BESS spectrometer, the hit times are calculated as combined timing of two PMTs of a TOF counter by using Eq.(3.4) together with z-position. The TOF of the BESS spectrometer obtained from the data for TOF counter PMTs, T_{tof} , is expressed as,

$$T_{\mathrm{tof}} = T_M - T_U \tag{3.6}$$

where T_U and T_M are weighted averages (Eq. (3.4)) of the Upper TOF and the Middle TOF, respectively.

3.6.1 Calculation of time resolution

TOF data are analyzed with time-walk correction for Time-of-Flight of incident particle.

The ΔT is the difference between the TOF obtained from the data of TOF PMTs, T_{tof} (Eq. (3.6)), and the TOF calcullated from the tracking information, T_{trk}, i.e.,

$$\Delta T = T_{\mathrm{tof}} - T_{\mathrm{trk}} \tag{3.7}$$

$$T_{\mathrm{trk}} = \frac{L_{\mathrm{path}}}{c}\beta_{\mathrm{trk}}(R,m) = \frac{L_{\mathrm{path}}}{c}\frac{p}{E} = \frac{L_{\mathrm{path}}}{c}\sqrt{(ZR)^2/((ZR)^2+m^2)} \tag{3.8}$$

where L_{path} is the path length of the incident particles from the Upper TOF and the Middle TOF, Z the electric charge of the incident particles, R the rigidity of the incident particles, and c the velocity of light. Due to the error in R being small, the error in T_{trk} (Eq. (3.8)) is also small and the rms of ΔT represents the resolution of the TOF hodoscopes. There is a relationship among the ΔT and the time resolution of each counters,

$$\sigma(\Delta T)^2 = \sigma_M^2 + \sigma_U^2 + \sigma_{\mathrm{Trk}}^2 \tag{3.9}$$

$$\sigma_M^2 \approx \sigma(\Delta T)^2 - \sigma_U^2 \tag{3.10}$$

The time resolution of the Middle TOF (σ_M) is estimated by ΔT and σ_U.The performance of the Middle TOF will be described in Chapter 6.

3.7 dE/dx Measurement with TOFs

QDC data are normalized for the gains of the PMTs and the QDCs after subtracting its pedestals. The dE/dx in a scintillator is obtained from the average of each PMT signals which is calculated by dividing by the transverse length in the scintillator and by correcting for the attenuation of light in the scintillator. Figure 3.7 shows scatter plot of dE/dx versus rigidity for the Upper TOF, the Lower TOF, and the Middle TOF obtained in the process of the BESS-Polar II data analysis [33]. It may be clearly understood that the detectable lowest energy of the Middle TOF is much lower than that of the Lower TOF. The dE/dx distributions will be used for the antiproton identification in the performance analysis to be described in Chapter 6.

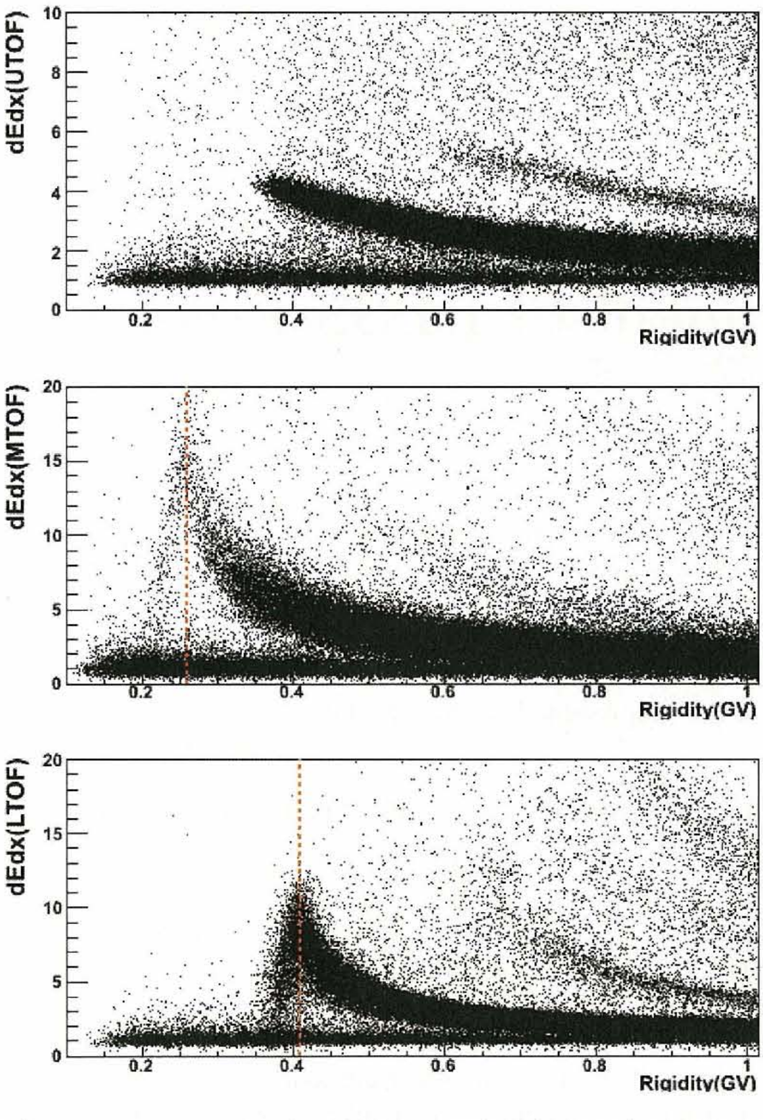

Figure 3.7: dE/dx measurement by (top) Upper TOF, (middle) Middle TOF, and (bottom) Lower TOF. The dashed lines are the detectable lowest rigidity of protons for each TOF. The Middle TOF acquires the low rigidity (~0.25 GV) particles which cannot penetrate to the Lower TOF [33].

Chapter 4

Development of BESS-Polar II Middle TOF

The Middle TOF has been added to the BESS-Polar spectrometer in order to improve the antiproton statistics in the lowest energy region. The place of the Middle TOF is just below the JET/IDC. It makes the trigger for particles which cannot penetrate to the Lower TOF. The BESS-Polar I Middle TOF is single-readout because of strict spatial restriction. It limited the performance of the Middle TOF. To enhance the performance of the Middle TOF, we developed the double-sided readout Middle TOF for BESS-Polar II.

4.1 Spatial restrictions and limit of performance with BESS-Polar I Middle TOF

In this section, we describe the strong spatial restrictions of the BESS-Polar I Middle TOF. Figure 4.1 shows the schematic view of BESS-Polar I spectrometer inside the magnet. The place of the Middle TOF is the space between the JET/IDC and magnet bore. The radial clearance between the JET/IDC and magnet bore is 13 mm. The axial clearance between the JET/IDC and the wall of liquid helium tank side is only 7 mm. All electronics and high-voitage system inside the magnet bore should be placed in the opposite side of liquid helium tank. If we consider the double-sided readout Middle TOF, we have to bring the tank side light guide to the opposite side. The magnet bore and the wall of liquid helium tank side is crossing vertically with very narrow space.

The BESS-Polar I Middle TOF was carefully developed for all components including scintillator, light guide, and PMT. The BESS-Polar I Middle TOF realized the installation in the strongly restricted area. During the BESS-Polar I flight, the Middle TOF worked well and showed the good confidence in the strict environment of balloon experiment.

However, the BESS-Polar I Middle TOF did not show good performance due to the single-sided readout. The time resolution of the Middle TOF had strong axial position dependence from 300 ps to 650 ps as shown in Figure 1.3. The single-sided readout Middle TOF also could not acquire the axial position information. The axial position information is very important to reject the noise event. Thus, the double-sided readout Middle TOF is developed for BESS-Polar II.

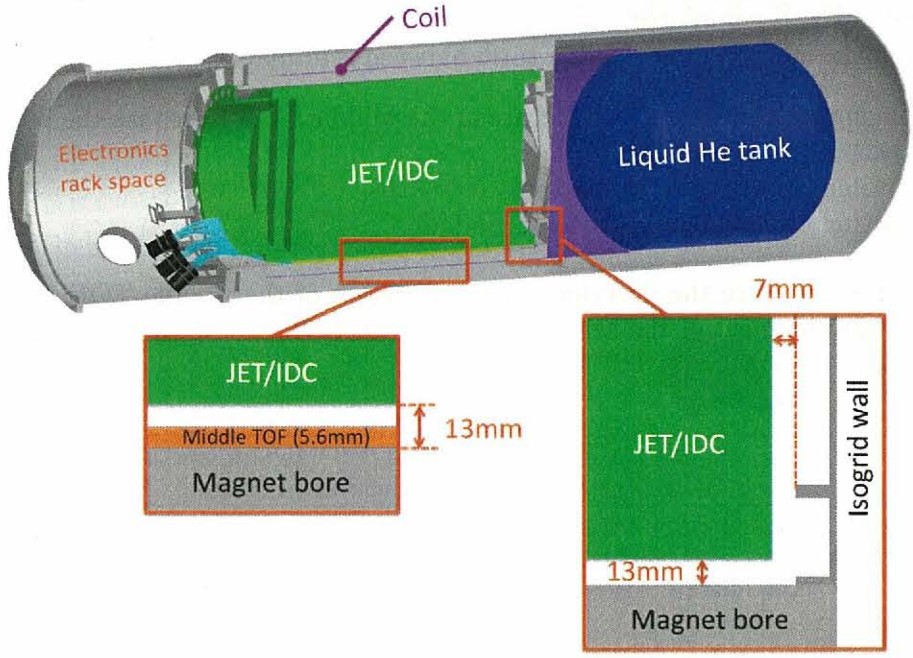

Figure 4.1: The schematic view of BESS-Polar I spectrometer inside the magnet. The radial clearance between the JET/IDC and magnet bore is 13 mm. The axial clearance between the JET/IDC and the wall of isogrid is only 7 mm.

4.2 Development of BESS-Polar II Middle TOF

In this section, we describe the development of the BESS-Polar II Middle TOF. The development of the BESS-Polar II Middle TOF consist of two categories as following.

1. Enhancement of the number of photo-electron (time resolution)
   A. Selection of scintillator
   B. Enhancement of cross section ratio between scintillator and light guide
2. Development of mechanical structure of the Middle TOF to realize the both-end readout
   A. Development of fiber connectors
   B. Routing of fiber bundle for new readout

At first we introduce the overview and comparison of the Middle TOF. After that, we describe the development of the Middle TOF.

4.2.1 Comparison of the BESS-Polar I Middle TOF

Figure 4.2 shows the summary of the BESS-Polar I and the BESS-Polar II Middle TOF. Basically, each component of the BESS-Polar II Middle TOF is same as BESS-Polar I. Each difference will be described from next section.

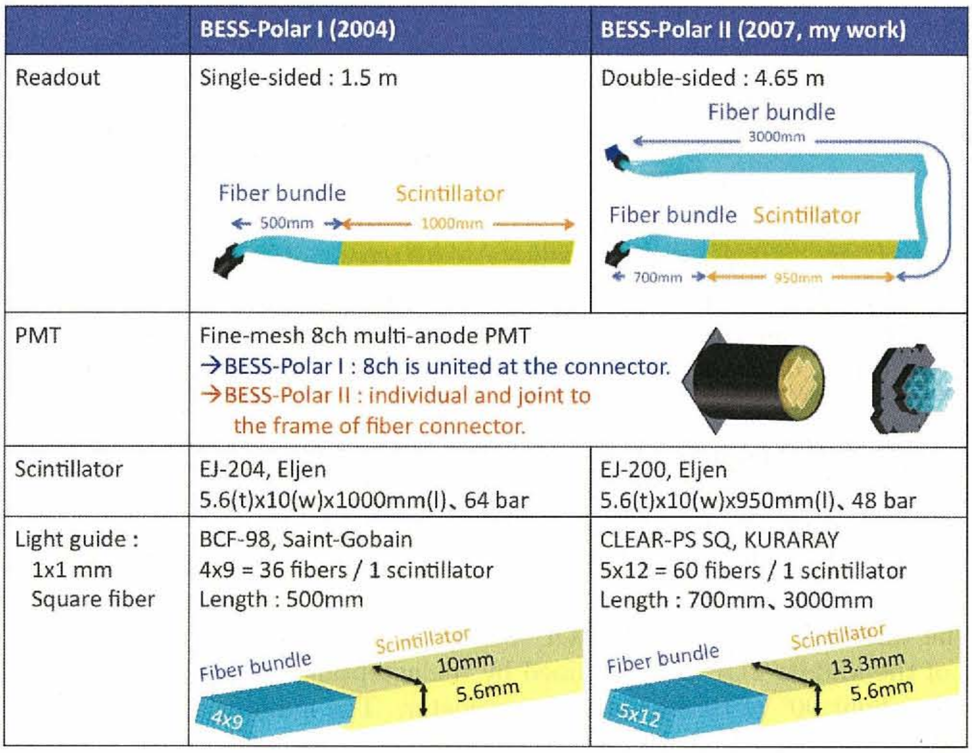

	BESS-Polar I (2004)	BESS-Polar II (2007, my work)
Readout	Single-sided : 1.5 m Fiber bundle Scintillator 500mm 1000mm	Double-sided : 4.65 m Fiber bundle 3000mm Fiber bundle Scintillator 700mm 950mm
PMT	Fine-mesh 8ch multi-anode PMT →BESS-Polar I : 8ch is united at the connector. →BESS-Polar II : individual and joint to the frame of fiber connector.	
Scintillator	EJ-204, Eljen 5.6(t)x10(w)x1000mm(l)、64 bar	EJ-200, Eljen 5.6(t)x10(w)x950mm(l)、48 bar
Light guide : 1x1 mm Square fiber	BCF-98, Saint-Gobain 4x9 = 36 fibers / 1 scintillator Length : 500mm Fiber bundle Scintillator 4x9 10mm 5.6mm	CLEAR-PS SQ, KURARAY 5x12 = 60 fibers / 1 scintillator Length : 700mm、3000mm Fiber bundle Scintillator 5x12 13.3mm 5.6mm

Figure 4.2: The comparison with the BESS-Polar I and the BESS-Poar II Middle TOF.

4.2.2 Scintillator

The scintillator for the Middle TOF is thin scintillator (BESS-Polar I : 950 × 10 × 5.6 mm, EJ-204, Eljen, BESS-Polar II : 950 × 13.3 × 5.6 mm, EJ-200, Eljen). In BESS-Polar II, we selected long attenuation length scintillator for the BESS-Polar II Middle TOF to restrict the axial position dependence of time resolution. Table 4.1 shows the comparison of each scintillator.

Table 4.1: Physical and scintillation constants of each scintillator.

	EJ-204 (BESS-Polar I)	EJ-200 (BESS-Polar II)
Light output (%)	68	64
Wavelength of Max. emission (nm)	408	425
Typical light attenuation length (cm)	160	380
Rise Time (ns)	0.7	0.9
Decay Time (ns)	1.8	2.1
Pulse width, FWHM (ns)	2.2	2.5

The shape of the Middle TOF is determined by the properties of low energy antiproton. The low energy antiproton may annihilate with the BESS-Polar spectrometer. The Middle TOF have to keep the small width to distinguish multi-track which come from annihilation of antiprotons. The width of the BESS-Polar I Middle TOF is selected as 10 mm from this reason. The Middle TOF have to install 13 mm space between the JET/IDC and, magnet bore. The thickness of the Middle TOF is 5.6 mm because of the spatial restriction. The number of the Middle TOF is determined by the acceptance of the Lower TOF. The Lower TOF cover about 90° of BESS-Polar spectrometer. The number of paddles for the BESS-Polar I Middle TOF is 64 to cover 93° of BESS-Polar spectrometer. The number of paddles for the BESS-Polar II Middle TOF is 48 to save the number of QDC board and TDC board for the Middle TOF because the double-sided readout require twice electronics of the single-sided readout. To keep the same acceptance, the width of scintillator for the BESS-Polar II Middle TOF is determined to be 13.3 mm.

4.2.3 Light Guide

The light guide for the Middle TOF is square fiber bundles (BESS-Polar I : BCF-98 Saint-Gobain, BESS-Polar II : CLEAR-PS SQ, KURARAY) because of following reason.

The flexibility for the light guide of the Middle TOF is required by the spatial restriction of the Middle TOF and the scheme of installation. Figure 4.3 shows the scheme of installation for the Middle TOF and the JET/IDC. We have to install the Middle TOF before the JET/IDC to check the alignment of the Middle TOF. We install the JET/IDC after the installation of the Middle TOF. The light guide of the Middle TOF have to avoid the the

JET/IDC during the installation of the JET/IDC. The direction of PMT is restricted by the magnetic field. Thus, the light guide have to change the position to attach the PMT after the installation of the JET/IDC. A flexible bundle of 60 square fibers (1×1 mm) is used as a light guide connecting each end of the scintillator and PMT because of such kind of restrictions. The square fibers are selected to ease their void-free arrangement into a bundle without any gaps as compared to the round fibers. In addition, the glued square fiber bundle have good mechanical strength comparable solid acrylic light guide but are compiling to the complex routing inside the magnet.

4.2.4 Photomultiplier

The Photomultipliers (PMT) for the Middle TOF is a 2.5 inch fine-mesh 8 channel multi-anode PMT (R6504 MODX-M8ASSY, HAMAMATSU PHOTONICS), which is selected for their magnetic field tolerance and small space requirement for 64 channel readout of the BESS-Polar I Middle TOF. The 8 anode channels of one PMT are used for the charge determination of the associated individual scintillator strips. The timing and trigger for 8 strips is derived from the common dynode signal. The direction of PMT have to parallel for the direction of magnetic field. Figure 4.4 shows the magnetic field of BESS-Polar spectrometer. The angle between the PMT and magnetic field is about 4.5°. The strength of magnetic field around the PMT is about 0.145 T.

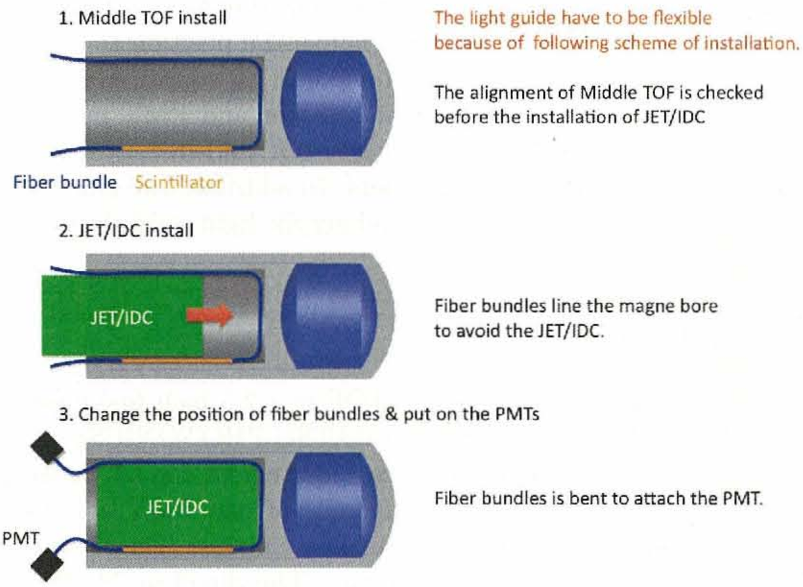

Figure 4.3: The scheme of installation for the Middle TOF and the JET/IDC. The fiber bundles of the Middle TOF have to avoid the JET/IDC when the JET/IDC is installed. After the installation of the JET/IDC, we change the direction of fiber bundles to attach the PMT.

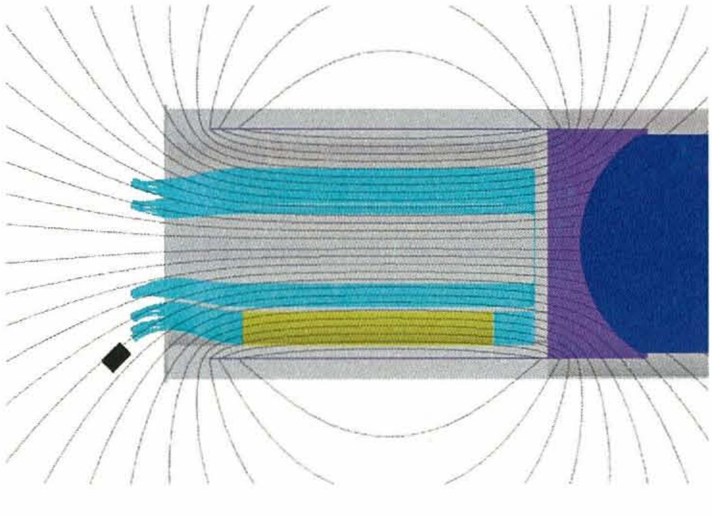

Figure 4.4: The orientation of magnetic field in BESS-Polar II spectrometer.

4.2.5 Fiber connectors

Basically, we have to deal with the Middle TOF as the unit of module because of multi-anode PMT. On the other hand, the installation of the BESS-Polar II Middle TOF is very complicated especially for the treatment of long fiber side. The treatment of the BESS-Polar II Middle TOF with the unit of module seems to be impossible to realize the installation. To install the BESS-Polar II Middle TOF strip by strip, we have to introduce an additional improvement. We developed a fiber connector to the PMT that could be assembled after the individual fiber bundles were routing inside the magnet bore. Figure 4.5 shows the structure of the fiber connectors. The end pieces on each fiber bundle are joined in a fiber connector and are interconnected by a tongue-and-grove technique providing a perfectly flat surface which interfaced the PMT.

4.2.6 Channel assignment to prevent crosstalks

The low energy antiprotons which is detected by the Middle TOF have the opportunity to annihilate and make the multi-track. On the other hand, there are crosstalk effect in the multi-anode PMT. If the Middle TOF cannot reject the crosstalk effect effectively, we cannot clearly determine the multi-track event which comes from annihilation. To restrict the crosstalk effect, we carefully determined the channel assign of fiber bundles which connect the multi-anode PMT. The selection of hit channel in the BESS-Polar II Middle TOF is the hit coincidence of both side readout. Thus, the neighbor channels at one side are assigned as far as possible at the opposite side. Figure 4.6 shows the comparison of channel assign of fiber bundles at each side readout. For example, channel 11 of short fiber side is surrounded by 4 channels. It means there are many crosstalk candidates at the center of fiber bundles. On the other hand, the channel 11 is assigned to the edge of the PMT at the long fiber side. This method makes the efficient crosstalk rejection to determine the true hit channel.

4.2.7 Improvement of cable handling to create spacing for Middle TOF light guide

The radius of fiber bundles is about 10 mm which is wider than the space between the JET/IDC and isogrid. Further more, the fiber bundles of the Middle TOF is crossing at isogrid. The minimum space to go through the fiber bundles is about 22 mm including the structure which bind the fiber bundles. To obtain the sufficient space, we developed compact cable handling scheme for the JET/IDC. The edge of the JET/IDC have gas flow tube, the signale cable of the JET/IDC, and pre-amplifire for the JET/IDC signals. We carefully rearranged all components, and realized the compact handling scheme of the JET/IDC. We obtained the 25 mm space between the JET/IDC and isogrid.

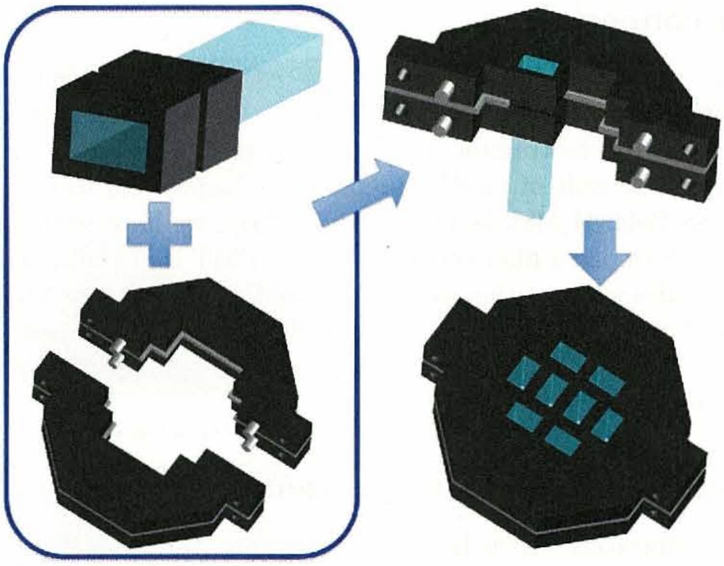

Figure 4.5: The fiber connector of the BESS-Polar II Middle TOF. The end pieces (upper left) on each fiber bundle are joined in a fiber connector (lower left) and are interconnected by a tongue-and-grove technique (upper right) providing a perfectly flat surface (lower right) which interfaced the PMT.

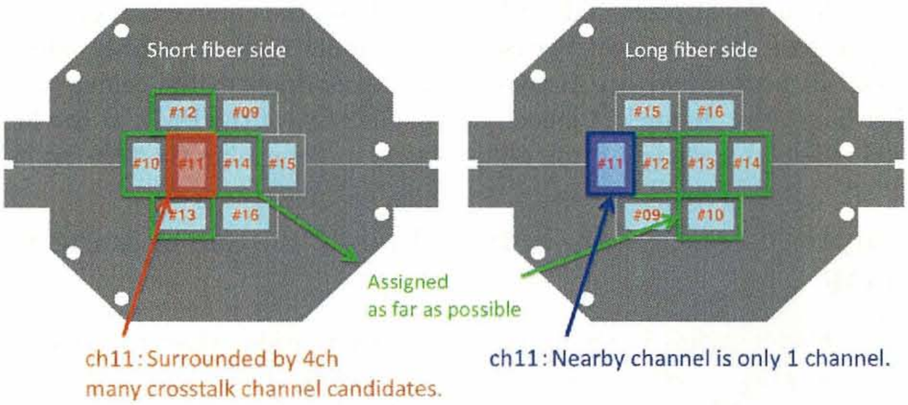

Figure 4.6: The channel assignment of fiber bundles at each readout. The neighbor channels of short fiber side are assigned as far as possible at the long fiber side considering the correlation of all channels.

4.2.8 Routing of fiber bundle for new readout

The routing of fiber bundles from the liquid helium tank side have several restrictions. The fiber bundles have to avoid the fiducial region of BESS-Polar II spectrometer because the interaction between cosmic-ray and the fiber bundle reduce the performance of detectable lowest energy. The fiducial region of cosmic-ray is about 90° at the upper half of BESS-Polar II spectrometer. The fiber bundles also have to avoid the signal cables of the JET/IDC, the gas flow tube, and the guide lane for the installation of the JET/IDC. These components are placed the both side of magnet bore. Figure 4.7 shows the acceptable region for the routing of fiber bundle.

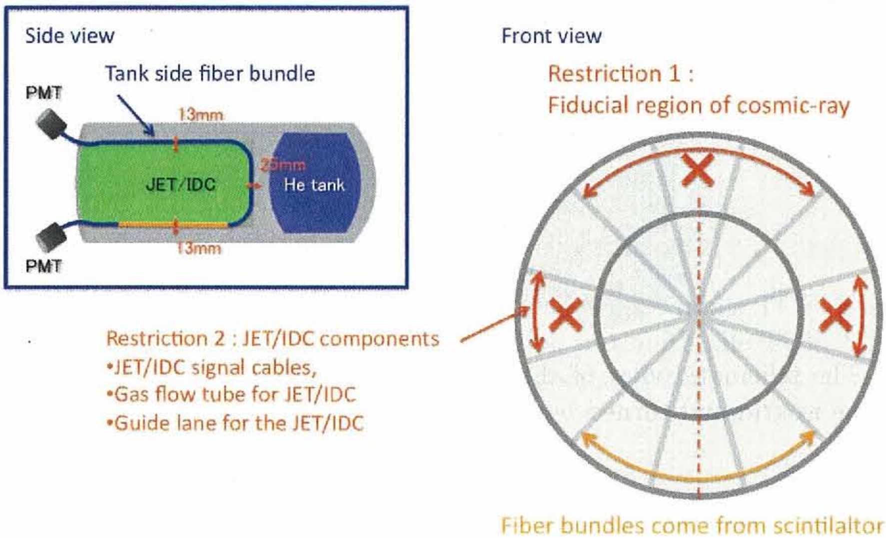

Figure 4.7: The schematic view of routing of fiber bundles. The routing is restricted by the fiducial region of cosmic-rays, the JET/IDC signal cables, and the guide lanes for the installation of the JET/IDC.

The routing of fiber bundles is determined by such kind of restriction with stress-free handling for the fiber bundles. Figure 4.8 shows the schematic view of the BESS-Polar II Middle TOF. The fiber bundles are crossing at the isogrid and turned back to the other side to avoid the restricted region. The isogrid is the Aluminum disk which has the ditches and the grids. From this routing, the length of tank side (long fiber side) fiber bundle is calculated and determined as 3 m. The length of opposite side (short fiber side) fiber bundle is 0.7 m. The length of scintillator is same as the length of the Upper and the Lower TOF which is 0.95 m. Thus, the total length of the BESS-Polar II Middle TOF is 4.65 m.

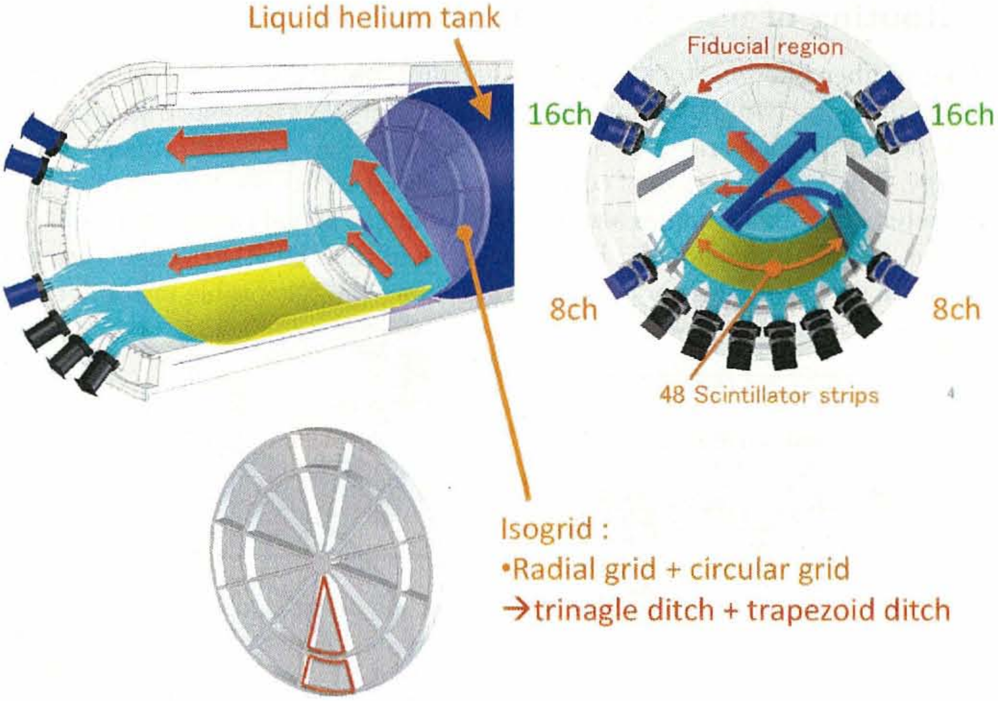

Figure 4.8: The schematic view of the BESS-Polar II Middle TOF. The fiber bundles are crossing at the isogrid and turned back to the other side to avoid the restricted region.

4.3 Installation of BESS-Polar II Middle TOF

To realize the BESS-Polar II Middle TOF as designed in figure 4.8, we installed the tank side fiber bundles with quite complicated scheme. We describe the detail scheme of installation as four part. Figure 4.9 shows the scheme of the installation.

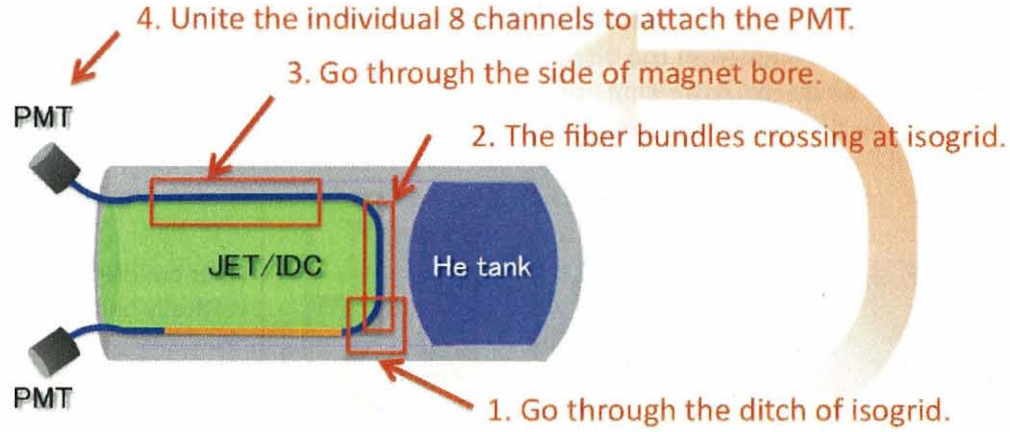

Figure 4.9: The scheme of the installation for the BESS-Polar Middle TOF. Each procedure will be described in this section. After the installation of the Middle TOF, 8 fiber bundles will unite together to connect the PMT as shown in section 4.2.5.

Process 1 : Magnet bore to the isogrid

The first step of installation is to determine the alignment of scintillator. After that, we deal with the long fiber side fiber bundles. The fiber bundles have to go through the vertically crossing point between the magnet bore and the isogrid. Figure 4.10 shows the scheme of installation at vertically crossing point. The fiber bundles go to the ditch of isogrid to avoid vertically bending. The shape of ditch is trapezoid. The width of ditch is not sufficient when the fiber bundles turn back from the ditch. Thus, the fiber bundles make the two layers when come back from the ditch. After that, the fiber bundles are crossing at the center region of isogrid. Thus, the fiber bundles immediately have to make the single layer in 30 ~50 mm.

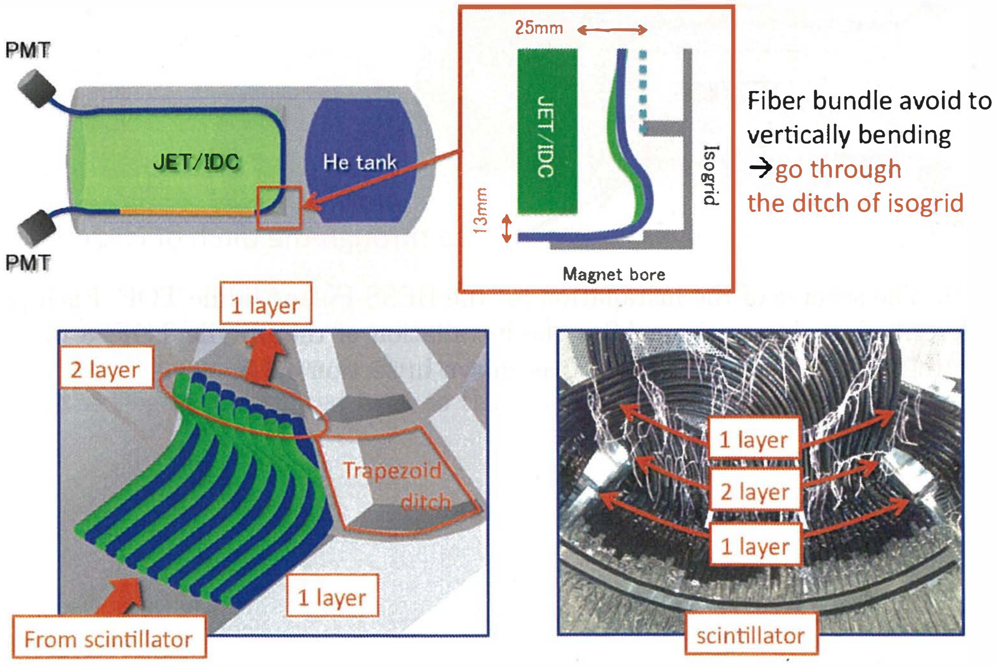

Figure 4.10: The fiber bundles from scintillators go through the narrow space between magnet bore and isogrid. The fiber bundles avoid vertically bending using the ditch of isogrid. The fiber bundles are two layer when the fiber bundles come back from the ditch. Lower right picture shows the actual handling of fiber bundles.

Process 2-1 : Isogrid, 1st layer

The fiber bundles are crossing at the center region of isogrid. At first, we install the left half of the Middle TOF which are placed in the first layer. After that, we install the right half of the Middle TOF which are placed in the second layer.

The fiber bundles have to be bounded to realize the path as designed in Figure 4.8. The thickness of fiber bundles is $\sim$10 mm including the shield of light leak. The total thickness of fiber bundles is $\sim$20 mm because the fiber bundles are crossing at this region. We have to find the scheme to hold the fiber bundles with the very thin materials within remained 5 mm.

We have to hold the fiber bundle with the string around the isogrid. The total number of the holding point is expected to be about 250. The isogrid don't have the jig to hold the quite many kind of strings. We use the 1 mm Aluminum punching metal to hang the strings. We can freely select the position of strings with punching metal and we do not need to make the holes when we change the path of the fiber bundles.

The strings which bind the fiber bundles have several restrictions. The strings have to non-magnetic body because the magnetic field of inside the magnet bore is 0.8 T. The strings have to be fine string because of the narrow radial clearance and the string have to go through 1 mm holes of punching metal with the pincet (tweezer). We searched the many strings and we selected the kite string to bind the fiber bundles.

Figure 4.11 shows the scheme of installation and actual photo of the installation.

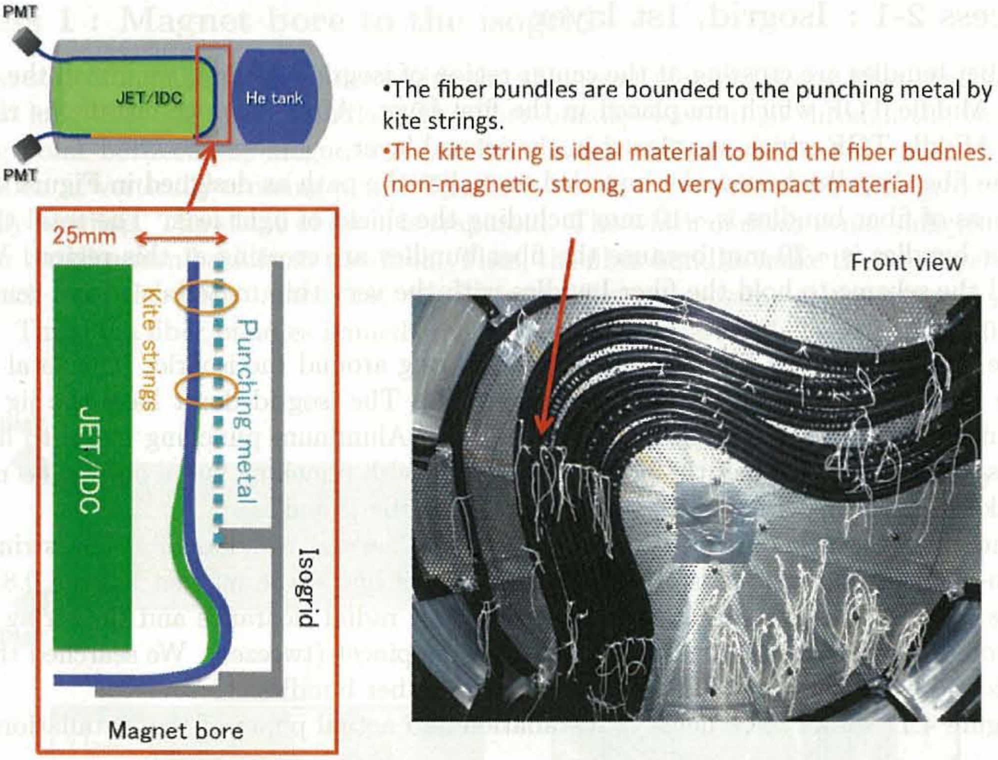

Figure 4.11: The fiber bundles are bound to punching metal by kite string. There are restrictions for the material to bind the fiber bundles. We have to use non-magnetic material because the strength of magnetic field in the spectrometer is 0.8 T. The string must be strong and fine because the space between the JET/IDC and isogrid is 25 mm.

Process 2-2 : Isogrid, 2nd layer

After the installation of the left half of the Middle TOF, we install the right half of the Middle TOF at the second layer. The scheme of second layer is same as first layer. We put the punching metal on the first layer to hold the fiber bundles of second layer. Figure 4.12 shows the scheme of installation and actual photo of the installation.

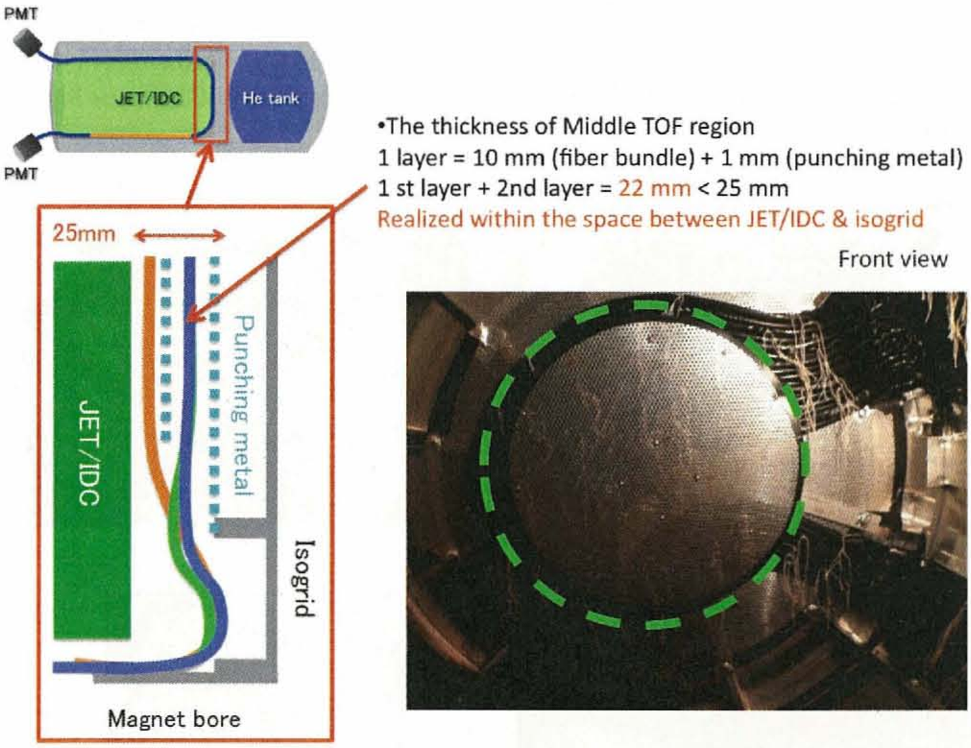

Figure 4.12: The scheme of second layer is same as first layer. The total width of the Middle TOF region is ~22 mm. The axial clearance between the JET/IDC and the Middle TOF is ~ 2 mm.

Process 3 : Side of magnet bore

The fiber bundles come from the isogrid go through the side of magnet bore and avoid the fiducial region of cosmic-ray. There are two paths for the fiber bundles. 32 channels go through the upper right and upper left of magnet bore. 16 channels go through the lower right and lower left beside the scintillator of the Middle TOF. The fiber bundles of upper region have to avoid dropping to the JET/IDC. We also use the kite string and the G10 sheet to hold the fiber bundles. There are many holes on the G10 sheet to go through the kite string. The fiber bundles of lower region is also bounded by G10 sheet with kite string to keep the position as designed. Figure 4.13 shows the scheme of installation and actual photo of the installation.

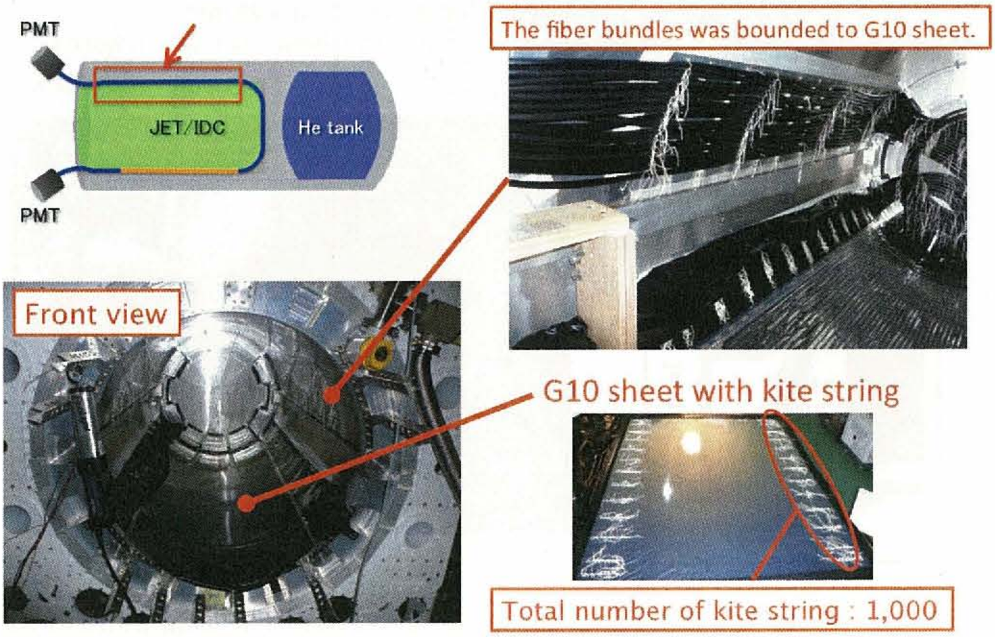

Figure 4.13: The handling of fiber bundles at the side is bounded to the G10 sheet whose thickness is 1 mm. Upper half of fiber bundles is bounded by kite string to avoid dropping to the JET/IDC.

4.3.1 Completion of the Middle TOF installation

We used quite many techniques to realize the double-sided readout Middle TOF in the restricted space. Figure 4.14 shows the actual BESS-Polar II Middle TOF after the installation. The BESS-Polar II Middle TOF was realized as designed.

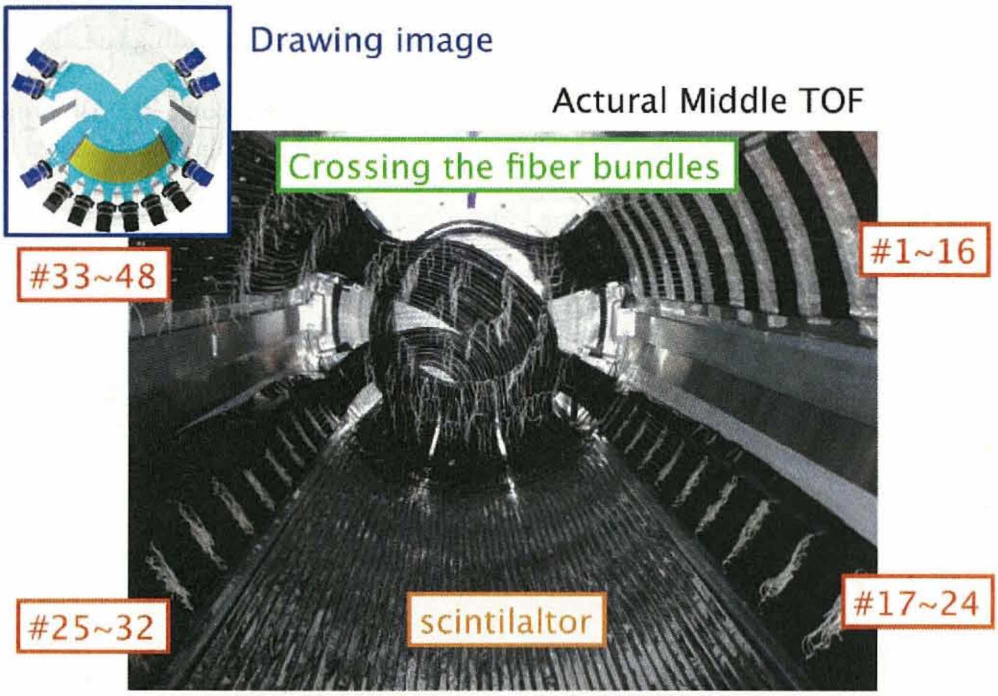

Figure 4.14: The installation of the Middle TOF is finally realized by various effort and technique. The place of fiber bundles is same as the design. The channel assignment of long fiber side is 16 channels for each upper half of fiber bundles, and 8 channels for each lower half of fiber bundles.

Process 4 : General assembly with the JET/IDC, and readout electronics.

After the installation of the Middle TOF, we also installed the JET/IDC without any troubles. Figure 4.15 shows the photo after the installation of the Middle TOF and the JET/IDC. The 8 channel Middle TOF which were individually installed unite each other to attach the PMT as shown in Figure 4.5. All fiber bundles reached the PMTs avoiding the all electronics of the JET/IDC.

We finally realized the double-sided Middle TOF for BESS-Polar II. All processes of installation were required strict spatial restrictions and careful installation as shown in above.

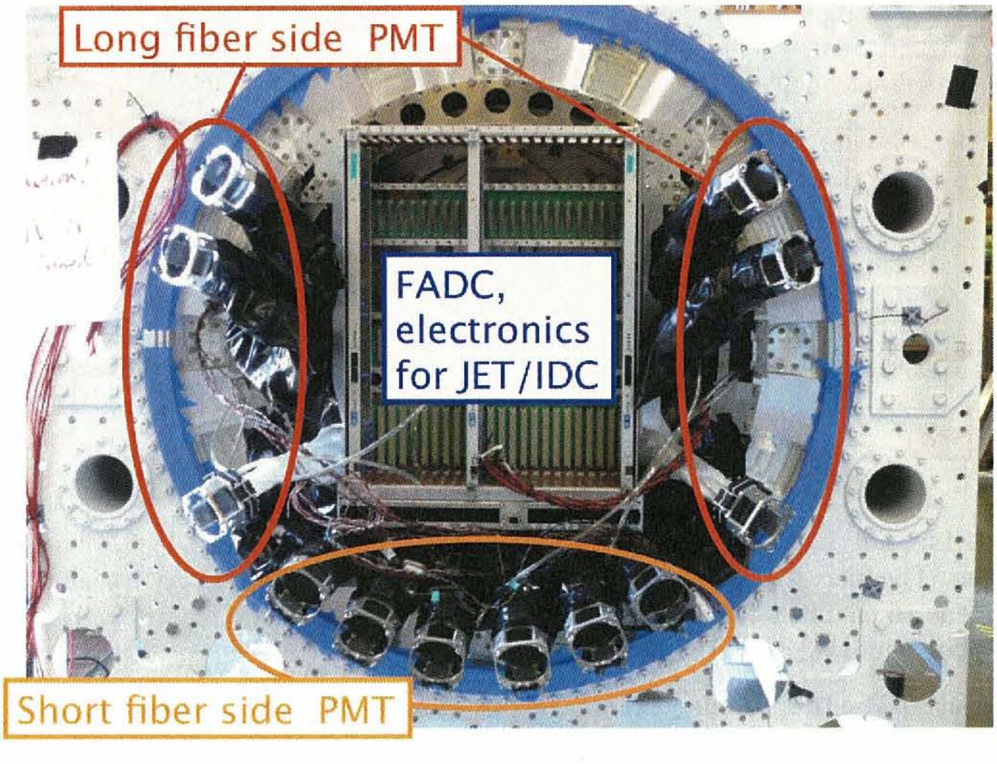

Figure 4.15: After the installation of the Middle TOF, the JET/IDC was installed without any troubles. After the installation of the JET/IDC, the 8 channel Middle TOF unite each other to attach the PMT.

Chapter 5

Balloon Flight

This chapter describes the BESS-Polar II flight. The second BESS-Polar scientific balloon flight was carried out in Antarctica from December 23, 2007 to January 21, 2008.

5.1 Balloon flight condition

Figure 5.1 shows the count rate of Climax neutron monitor and Sunspot number. The BESS-Polar II flight was launched at the solar minimum.

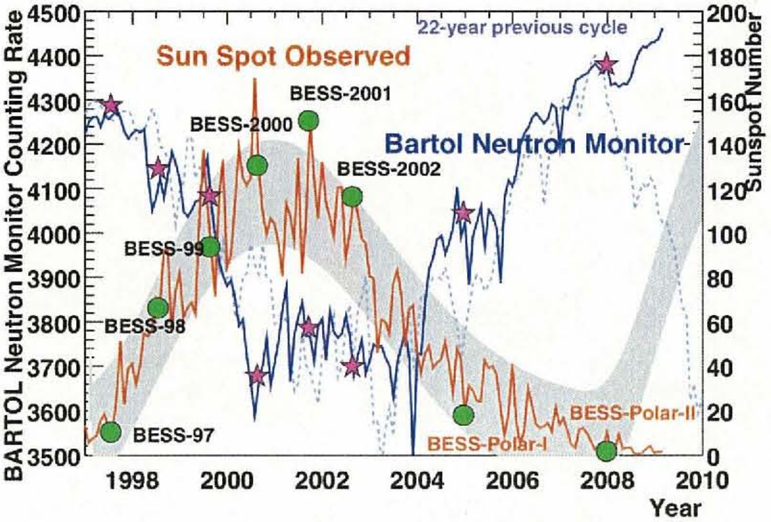

Figure 5.1: Variation of neutron monitor and sunspot number together with the date of past and current BESS flight.

The balloon carrying the BESS-Polar II payload was launched from Williams Field near the U.S. McMurdo Station. The weather condition was calm wind, which is the best condition for the launch. Figure 5.2 shows the launch of BESS-Polar II flight. The launch was succeeded and the BESS-Polar II flight was started without any troubles.

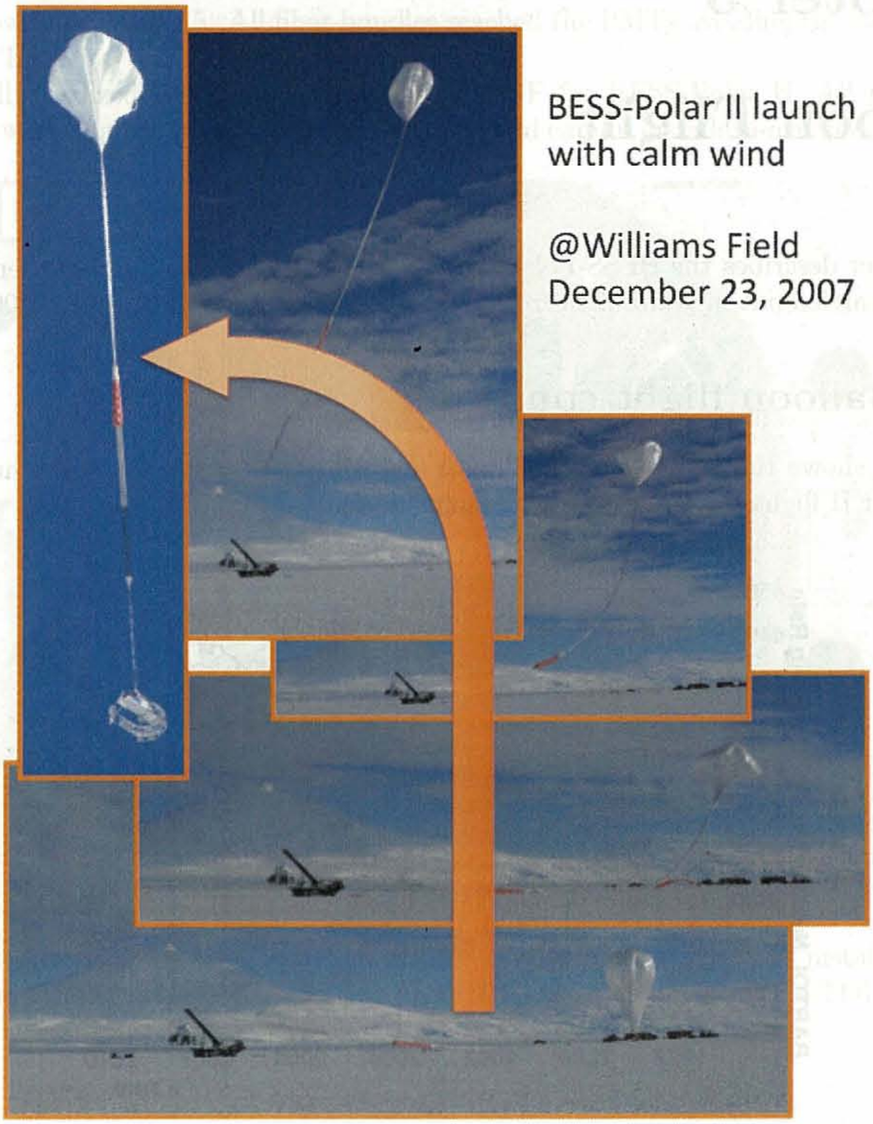

Figure 5.2: The launch of BESS-Polar II flight. The weather condition was calm wind which is the best condition for the launch.

Figure 5.3 shows the trajectory of the BESS-Polar II flight. The payload flew with one and 3/4 circumnavigation over Antarctica in 29.5 days. During the flight, the trajectory was close enough to the South magnetic pole for the geomagnetic cutoff rigidity. The magnetic rigidity cut-off did not exceed 0.6 GV and the majority of the flight was below 0.2 GV. Total observation time was 24.5 days, limited by the data storage capacity and the magnet cryogen life.

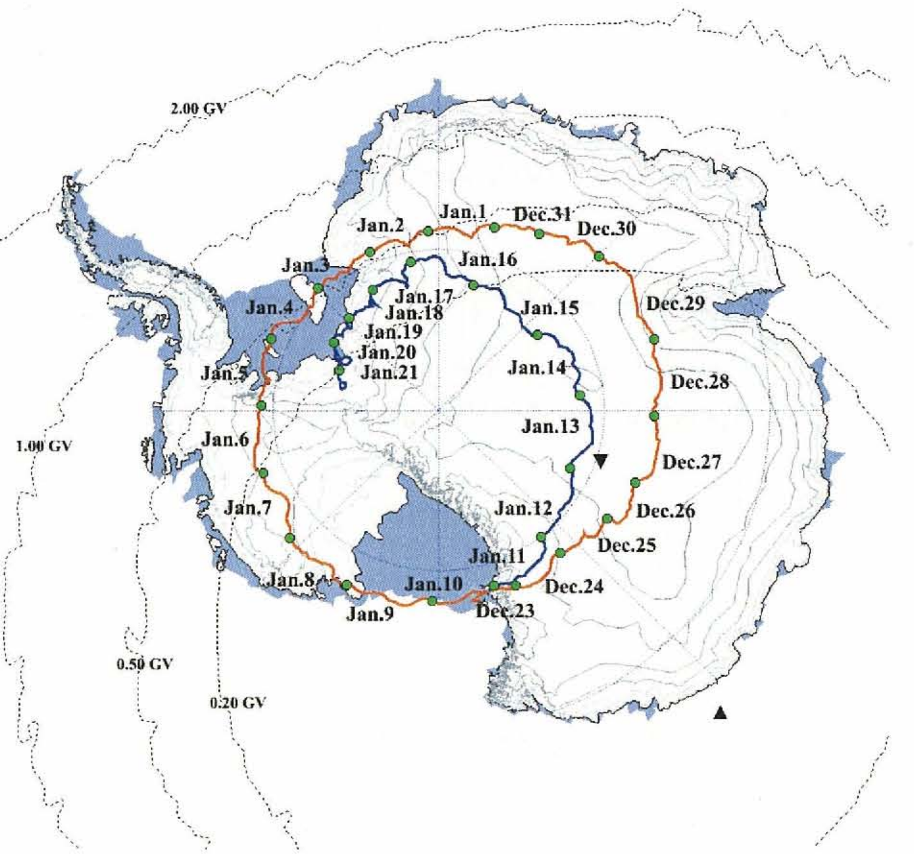

Figure 5.3: BESS-Polar II trajectory. Contour lines indicate geomagnetic cutoff rigidity.

Figure 5.4 shows the pressure and altitude profile during the flight [36]. The balloon was floated at an altitude of 34 km to 38 km. The residual atmosphere was 6 g/cm^2 on average, during the floating.

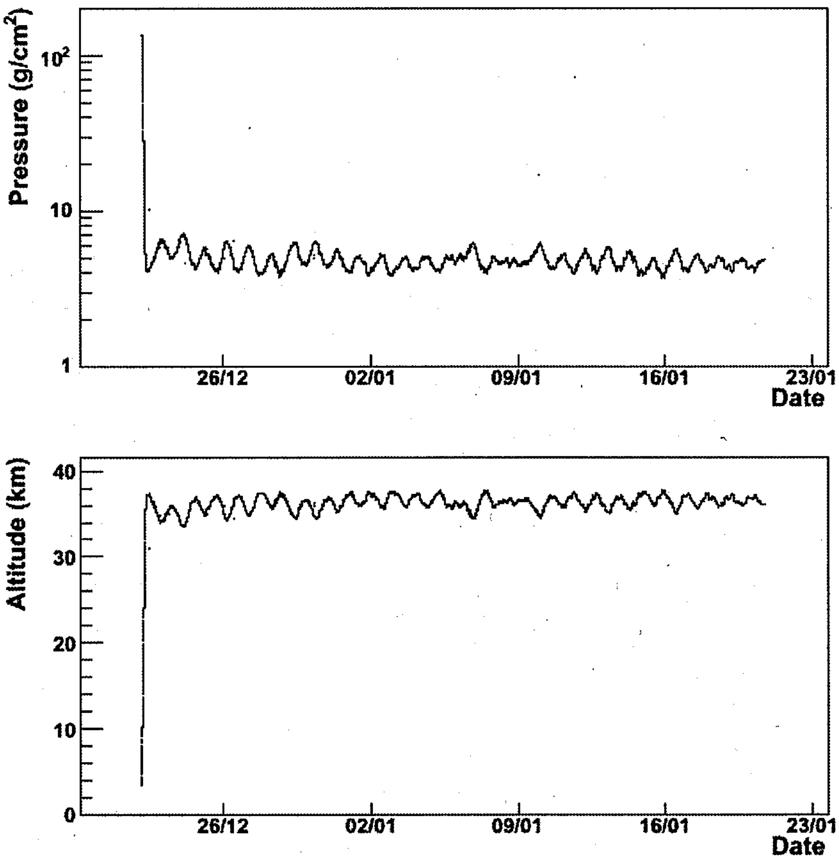

Figure 5.4: Residual atmospheric pressure (top) and atitude (bottom) during the flight. [36]

The balloon flight was terminated on January 21, 2008 and the payload safely landed on the ice field located 370 nautical miles from the south pole. We had a first access to the payload by plane and recovered the data vessel. After two years from the BESS-Polar II flight, the rest of payload was recovered in January 17, 2010.

The total number of cosmic-ray events accumulated in the BESS-Polar II flight was about 4700 million, which occupied to 13.5 terabytes of the HDD storages volume. Figure 5.5 shows the date vs the number of event plot. Table 5.1 summarizes the BESS-Polar II flight 2007/2008. Science observation was successfully performed during the flight.

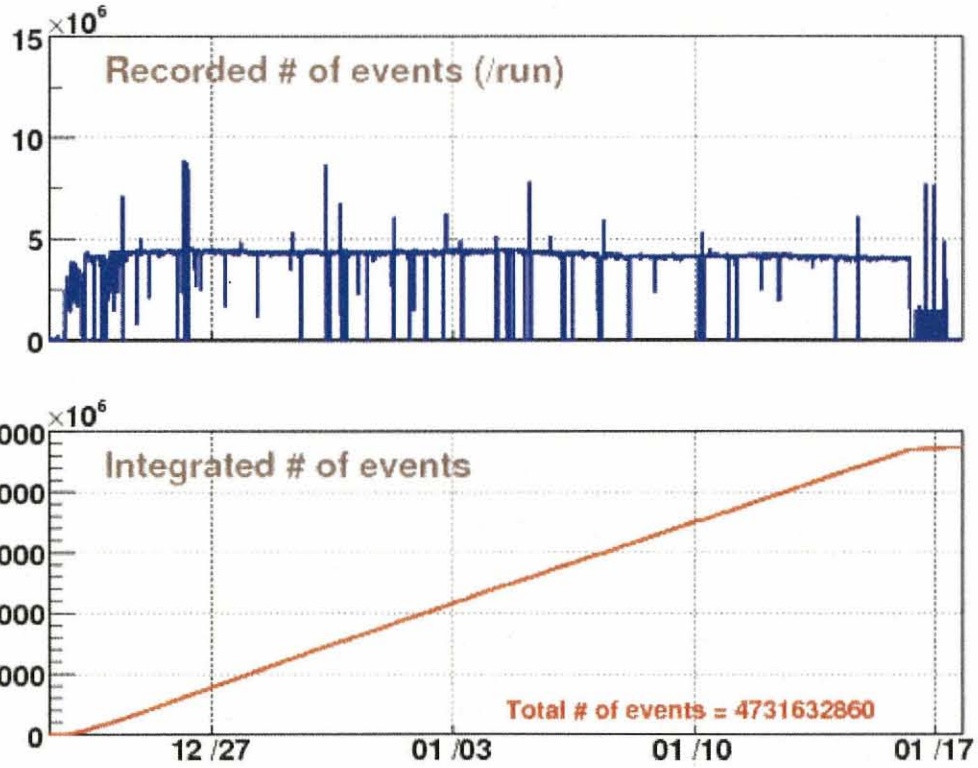

Figure 5.5: (top) Recorded number of events for each run. (bottom) Total event number as a function of date.

Table 5.1: Summary of BESS-Polar II flight.

Total Float Time	29.5 days
Observation Time	24.5 days
Recorded Event	4700 M
Recorded Data Size	13.5 TB
Trigger Rate	2.4 $\sim$ 2.6kHz
Live Time Fraction	0.77
Altitude	34 $\sim$ 38 km
Air Pressure	4.5 $\sim$ 8 g/cm^2

5.2 Status of TOFs during the flight

Some problems came up during the data taking period. However, we could detect the anomaly immediately with the monitor data and took appropriate actions to recover the detector performance.

Middle TOF PMT

One of the PMT for the Middle TOF was damaged during the shipping from USA to Antarctica. The damaged PMT is attached to the long fiber side fiber bundle and dropped the gain. The Middle TOF was installed and finalized in Palestine. All Middle PMTs were not exchanged with spare. The high-voltage power supply (HV) of the damaged PMT was enhanced from 1850 V to 1950 V. The TDC threshold was also changed from 160 mV to 40 mV which is the lower limit of TDC threshold with low noise rate. The TDC trigger efficiency of the Middle TOF is described in next chapter.

The QDC for the Middle TOF had no spare channel. There were two dead channel in the QDC. We assigned the dead channel to the edge of the Middle TOF.

The high-voltage of the Middle TOF was twice turned off during the flight. We monitored the BESS-Polar II payload condition with communication system, and immediately recovered HV of the Middle TOF. Figure 5.6 shows the HV and temperature of the Middle TOF PMT. The Middle TOF was worked well without serious trouble during the flight.

Upper TOF and Lower TOF PMT

Each one of the PMTs for the Upper TOF and Lower TOF was turned off because of High current leak during the flight. These two paddles became single-sided readout because one side of PMT was turned off. TOF counter makes the trigger signal with the coincidence of both side PMT. And we changed the trigger condition for the single-sided readout paddles from the coincidence of two PMTs to the single PMT trigger without coincidence. Some of

PMTs for the Upper TOF and Lower TOF enhanced the trigger rate. However, the signal amplitude of the noise pulses was small compared to a real cosmic-ray events, and, by raising discriminator threshold slightly, we could eliminate them without degradation of the TOF performance. As the result of these effort, we could keep the full acceptance. Figure 5.7 shows the configuration of the TOF PMTs during the flight [37].

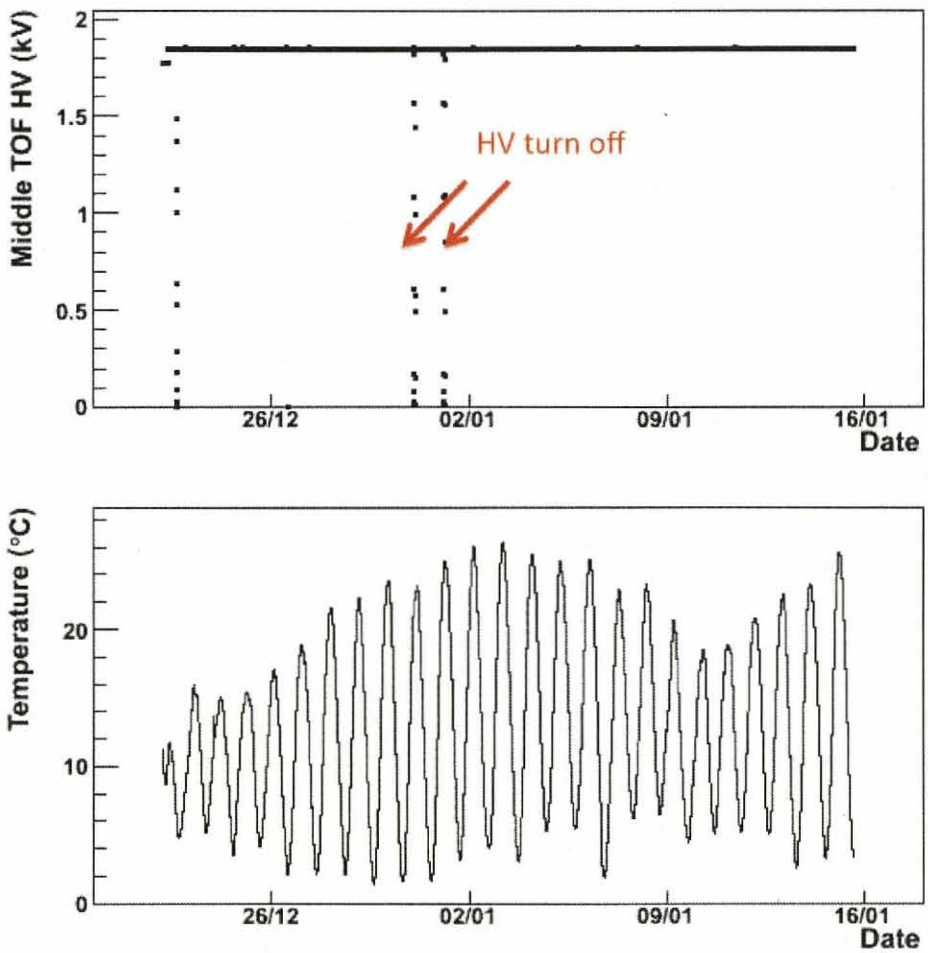

Figure 5.6: Fluctuation of the Middle TOF High-voltage (top) and the Middle TOF temperature (bottom). [37]

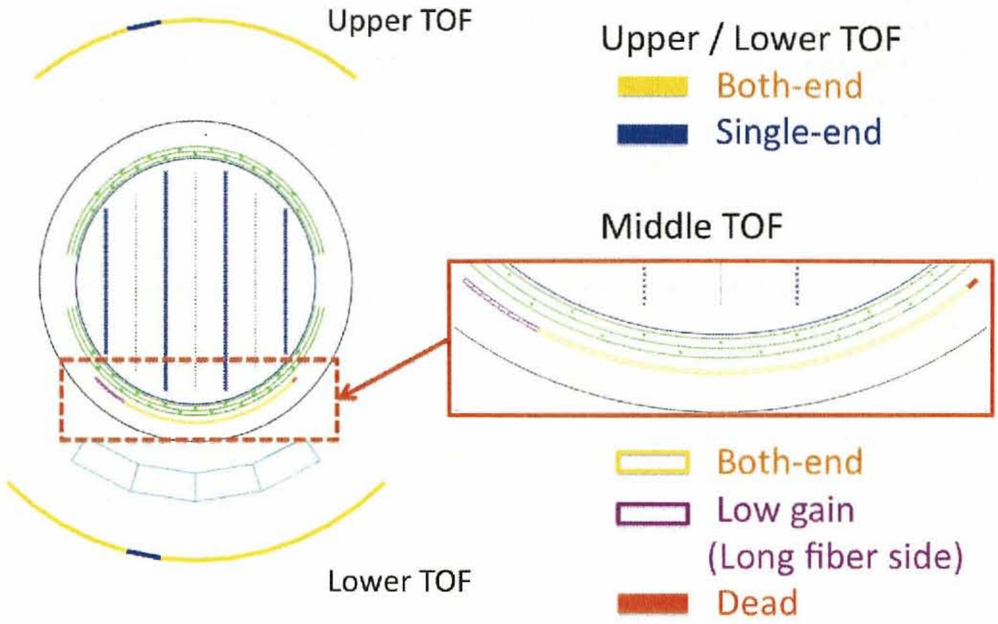

Figure 5.7: Configuration of TOF PMTs during the flight.

Trigger condition

Trigger rate was about 3.1∼ 3.3 kHz (≈2.4 ∼ 2.6 kHz if live-time fraction 0.77 was included). The trigger rate was kept stable through the flight. The BESS-Polar II spectrometer kept the full acceptance during the flight. The total acceptance of BESS-Polar I was about 66% of designed value because 18/44 TPF PMTs were turned off. The flux of cosmic-ray enhanced during the solar minimum. Thus, the trigger rate of BESS-Polar II was higher than that of BESS-Polar I (∼1.4 kHz). The CPU of DAQ system and Flash ADC performance of BESS-Polar II was improved compare to BESS-Polar I. The live time fraction of BESS-Polar II (77%) under the high trigger rate was almost same as BESS-Polar I (80%). We had observed the slight deviation of the trigger rate, which was well correlated with solar wind speed and neutron monitor as shown in Figure 5.8. We observed realtime solar modulation effect to the cosmicray measurement.

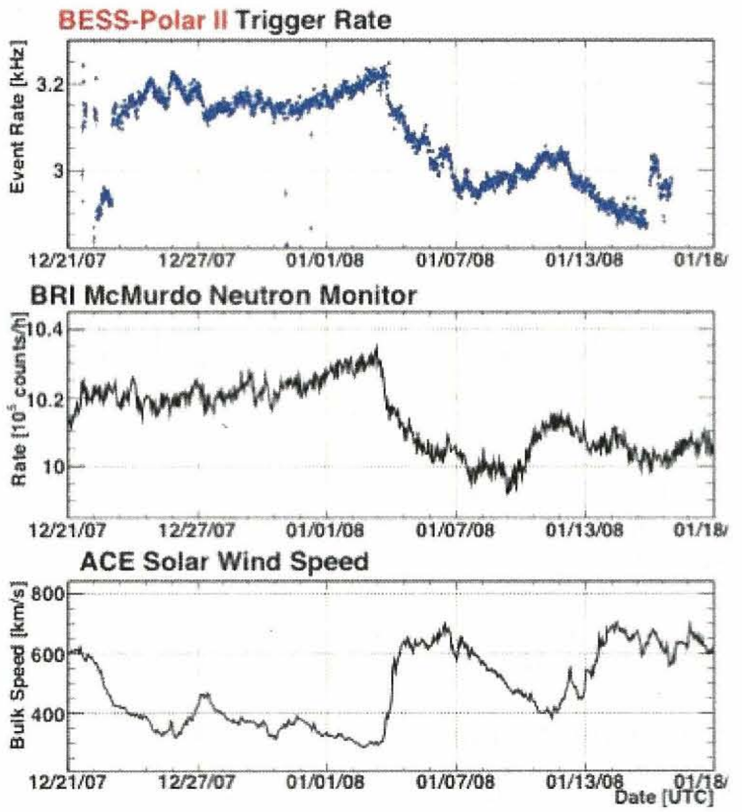

Figure 5.8: Time variations of BESS-Polar II trigger rate (top), neutron monitor (middle), and solar wind speed (bottom).

5.3 Summary of the data taking

The data taking of BESS-Polar II flight was successfully finished even if some detector got the trouble. Following list is the summary of data taking.

1. The number of event was 4700 M event for BESS-Polar iI flight
2. The trigger rate was 2.4~2.6 kHz with high live fraction (77%).
3. The Middle TOF worked well without any serious trouble.
4. The Upper and Lower TOF kept the full acceptance during the flight.

Chapter 6

Performance of Middle TOF

The BESS-Polar II Middle TOF worked well during the flight without serious troubles. In this chapter we show the performance of the Middle TOF with flight data. The statistics for analysis is about ~35 % of flight data.

6.1 Basic performance of Middle TOF

6.1.1 Number of photo-electrons

We calculated the Npe of each readout as follows:

$$N_{\mathrm{pe}} = \left(\frac{\mathrm{Mean}}{\sigma}\right)^2$$

where, Mean and σ are the result of gaussian fit. Figure 6.1 shows the QDC distribution of each readout at the center of axial position. We used the relativistic protons (Rigidity > 10 GV) for the evaluation of Npe. Npe of short fiber side is about 13 p.e. at the center of the Middle TOF. Npe of long fiber side is about 5.5 p.e. which is about half of short fiber side.

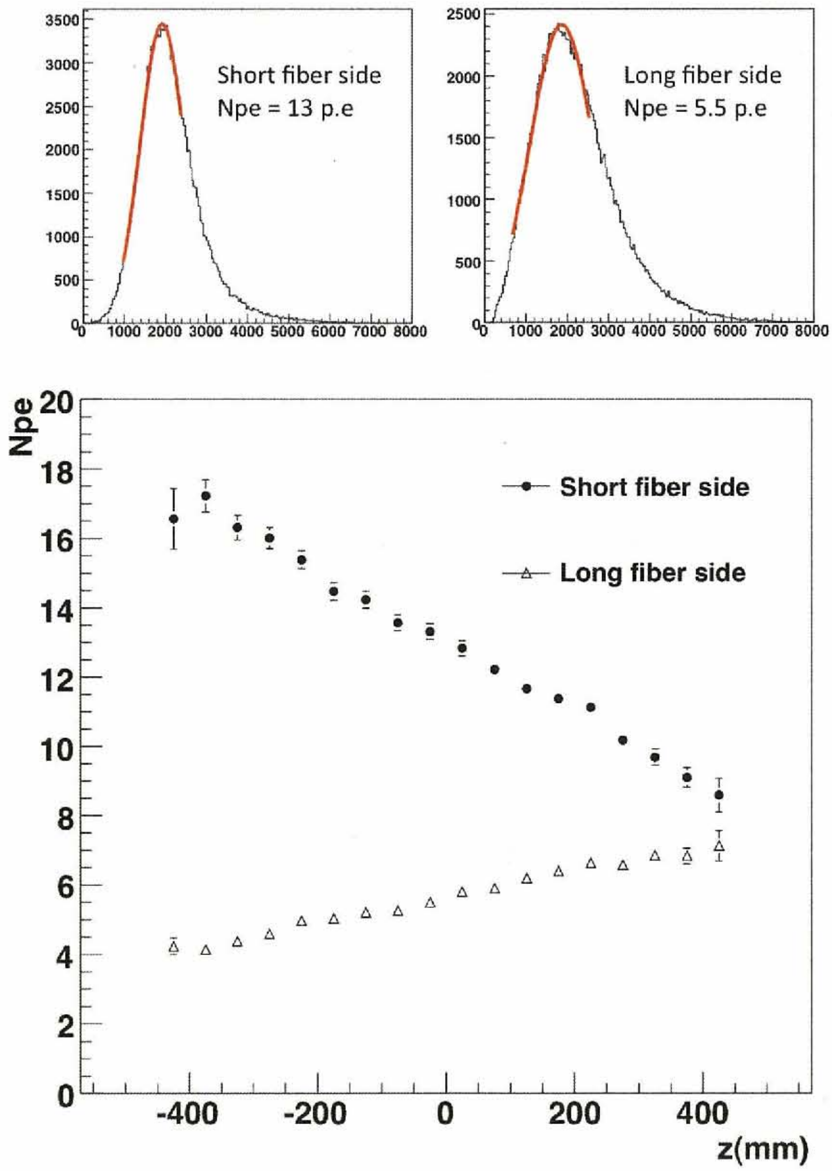

Figure 6.1: (top) QDC distributions of each readout at the center of axial position. The red-solid line is the gaussian fit. (top-left) QDC distribution of short fiber side. (top-right) QDC distribution of long fiber side. (bottom) N_{pe} of MTOF for each readout depends on the axial position.

6.1.2 Trigger efficiency of Middle TOF

Figure 6.2 shows the trigger efficiency of the Middle TOF. The trigger efficiency is evaluated by the single track proton event which is identified by Upper TOF and Lower TOF. We can estimate the trigger efficiency of the Middle TOF because the Middle TOF is placed between the Upper TOF and Lower TOF. Following equation is the definition of trigger efficiency of the Middle TOF.

$$\epsilon_{\mathrm{trig}} = \frac{\text{Middle TOF trigger event in single track protons}}{\text{Single track protons detected by Upper TOF and Lower TOF}}$$

The circle marker indicate the relativistic (Rigidity $>$ 10 GV) protons. The triangle marker indicate the low energy protons (Rigidity $<$ 1 GV) where is used for the identification of the antiprotons with the Middle TOF. The trigger efficiency of the Middle TOF have non-uniformitiy for ϕ direction for the relativistic protons. This is comes from the combination of low QDC gain channel and low scintillating photon channel of long fiber side. The axial position dependence of trigger efficiency comes from the attenuation of Npe. The energy loss of protons enhance around lower than 1 GeV. The Npe of the Middle TOF also enhance for low energy protons. Thus the trigger efficiency of the Middle TOF enhance for low energy protons because the Npe is higher than that of relativistic protons.

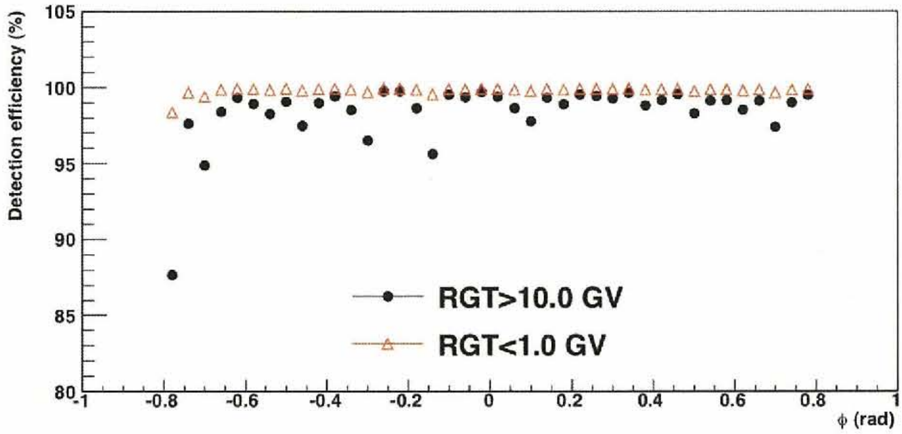

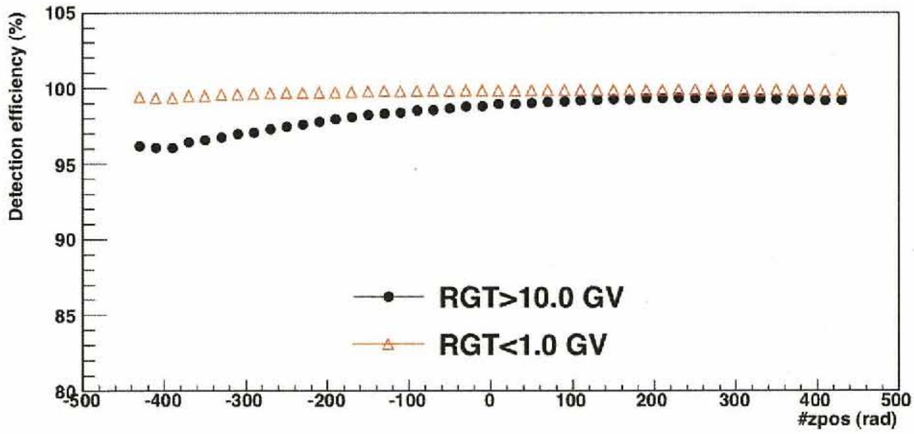

Figure 6.2: Trigger efficiency of the Middle TOF with UL trigger event

6.1.3 Effective velocity of light in the scintillator

Figure 6.3 shows the variation in t_{3c} and t_{4c} over z. The velocity of light in the scintillator is about 165 cm/ns in the Middle TOF. When we calculate the $T_3(z)$ and $T_4(z)$, we use this value.

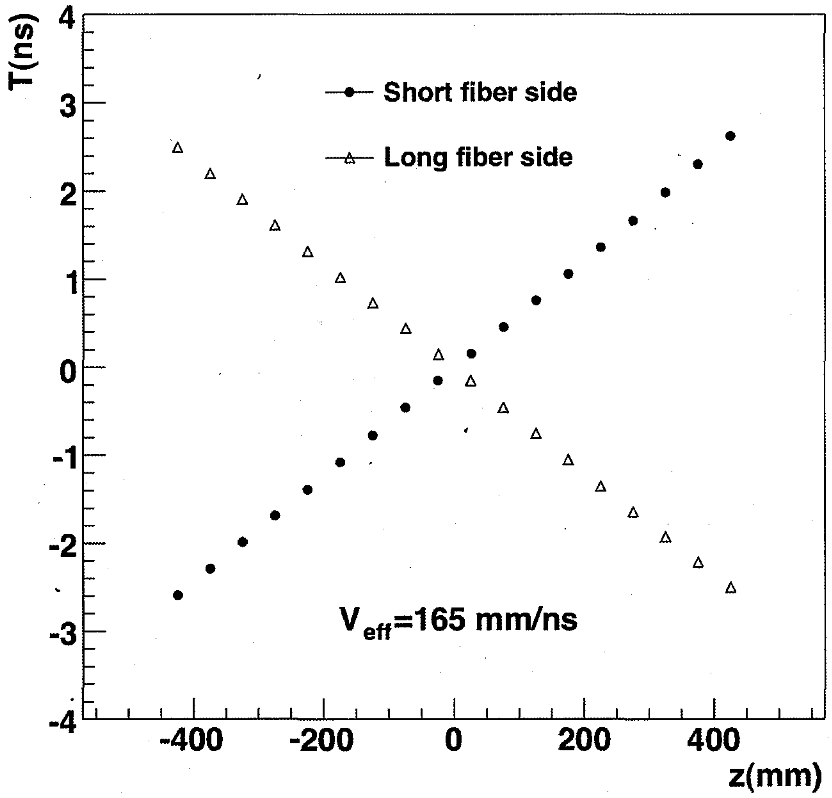

Figure 6.3: Effective velocity of light in the scintillator. The velocity of MTOF is 165 mm/ns.

6.1.4 Time resolution of the Middle TOF

The hit time of a particle is calculated by TOF counter with time-walk correction as described in Equation 3.1.

$$t_{\mathrm{ic}} = t_i - W_i/\sqrt{q_i}$$

The time-walk correction parameter W_i is determined by the scatter plot of $\Delta\mathrm{T}$ and $1/\sqrt{q_i}$. Figure 6.4 shows the scatter plots before and after the time-walk correction for each readout. The difference of $\Delta\mathrm{T}$ around center region ($1/\sqrt{q_i} \sim 0.025$) is about 1.5 ns between before and after the correction.

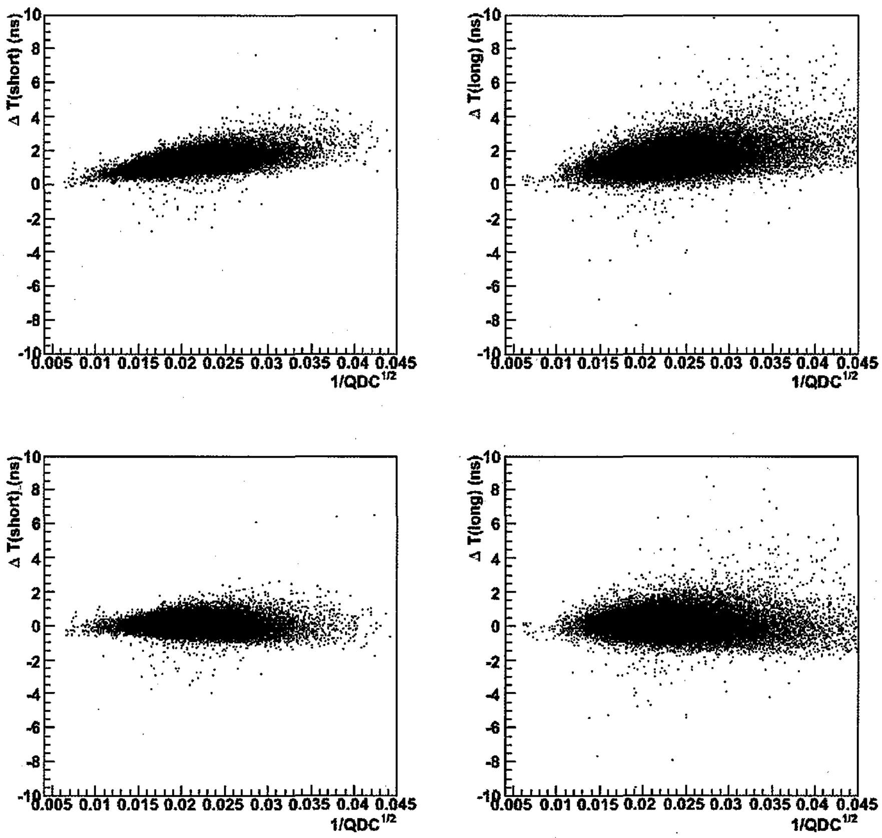

Figure 6.4: Time-walk correction by the scatter plot of $\Delta\mathrm{T}$ and $1/\sqrt{q_i}$ scatter plot. (top-left) Short fiber side before time-walk correction (W_4=0). (top-right) Long fiber side before time-walk correction (W_3=0). (bottom-left) Short fiber side after time-walk correction. (bottom-right) Long fiber side after time-walk correction.

After the time-walk correctin, we can evaluate the performance of time resolution. We use the weight average for hit time of the TOF counter. The weight ratio of each readout is calculated by time resolution of each readout depend on axial position. The weight ratio (wr) is described as follows:

$$\mathrm{wr}_i(z) = \frac{1/\sigma^2(\Delta T_i(z))}{1/\sigma^2(\Delta T_3(z)) + 1/\sigma^2(\Delta T_4(z))}$$
$$\Delta T_i(z) = T_i(z) - T_{trk}$$

The value of weight ratio for each position is derived by the polynomial function. The function of weight ratio is calculated by the fitting with quadratic function. Figure 6.5 shows the time resolution of each side and the weight ratio of each readout. For the general TOF counters, the time resolution of each readout is symmetric for axial position. Thus, the weight ratio is also symmetric. On the other hand, the light guide of the Middle TOF is not symmetric, the weight ratio of short fiber side is much higher than the ratio of long fiber side. The weight ratio of short fiber side near the readout of short fiber side ($\sim$ -450 mm) is about 90%.

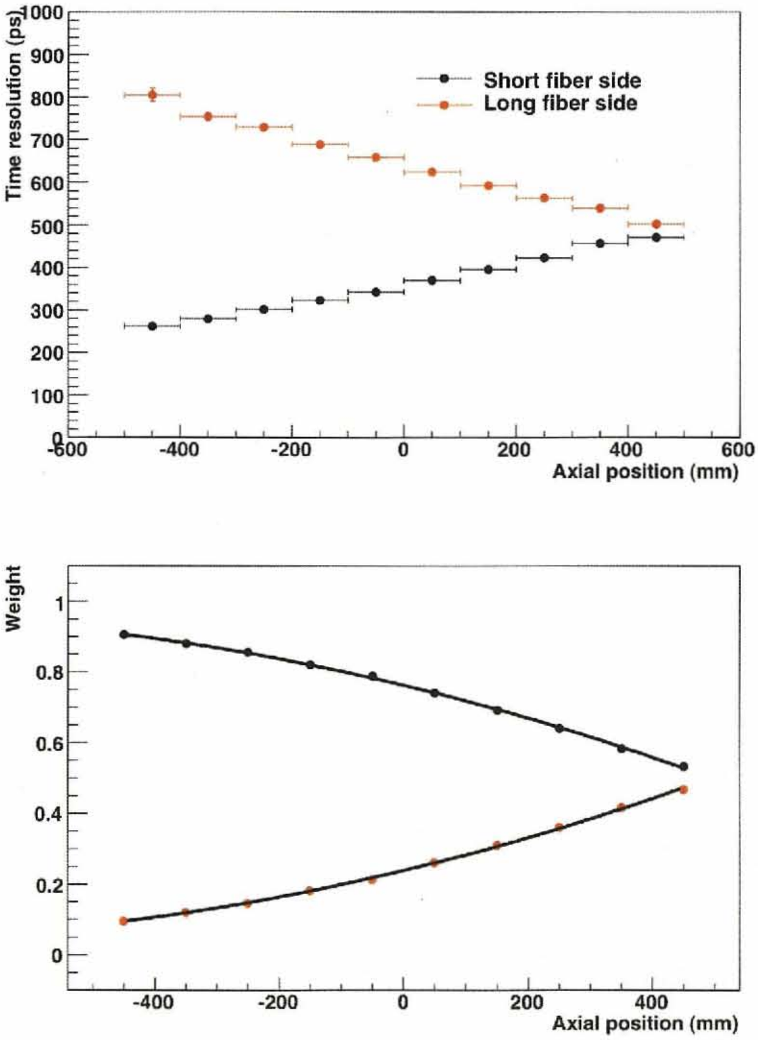

Figure 6.5: The weight ratio of channel 24. (top) time resolution of each side depend on axial position. It is used for the calculation of the weight ratio. (bottom) The weight ratio of each readout. The function of weight ratio is quadratic function as a result of fitting. The weight ratio of short fiber side is much higher than the ratio of long fiber side because the light guide of the Middle TOF is not symmetric. The weight ratio of short fiber side near the readout of short fiber side (~ -450 mm) is about 90%.

After the calculation of weight ratio, we can estimate the time resolution of the Middle TOF. The time resolution of the Middle TOF is calculated by the ΔT resolution of the Upper TOF and the Middle TOF calculated by Equation 3.7. Figure 6.6 shows the ΔT distribution for the relativistic protons. The ΔT resolution is 315 ps, and time resolution of the Middle TOF is calculated as 303 ps.

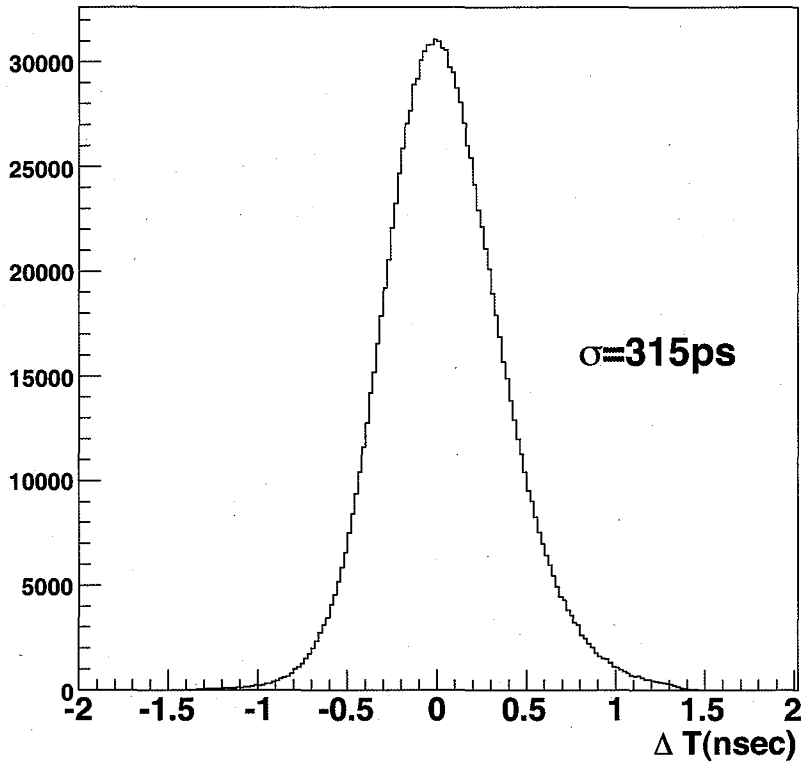

Figure 6.6: ΔT resolution of UM configuration.

Time resolution depend on the axial position

Figure 6.7 shows the time resolution of each side, average, and weighted average. The time resolution of short fiber side changes from 260 ps to 450 ps depend on the axial position. The time resolution of long fiber side is changes from 550 ps to 780 ps. The large difference of time resolution between short fiber side and long fiber side comes from the length of fiber bundles. The time resolution of average is strongly affected by the long fiber side. On the other hand, the time resolution of weighted average changes from 260 ps to 360 ps. The weighted average works well especially for the Middle TOF.

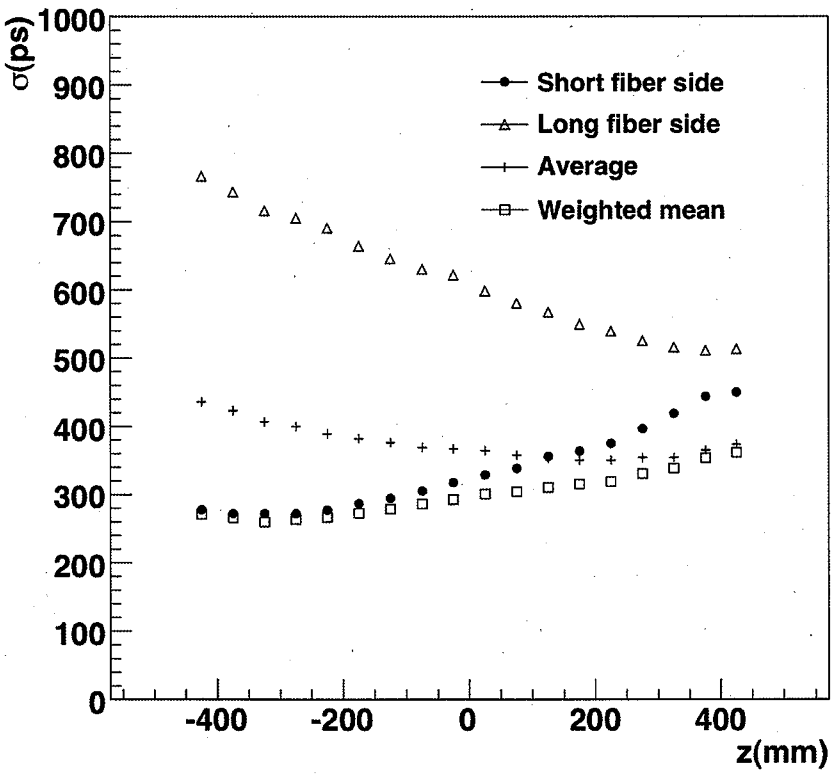

Figure 6.7: Time resolution of the Middle TOF depend on axial position.

Time resolution depend on rigidity

The time resolution of TOF counter basically depends on the N_{pe}. The energy loss of proton enhances around lower than 1 GV as shown in Figure 3.7 (dE/dx Middle TOF). It means the N_{pe} and time resolution of the Middle TOF enhance for low rigidity region. The correlation between N_{pe} and time resolution is as follows:

$$\sigma_M \propto \frac{1}{\sqrt{N_{pe}}}$$

Figure 6.8 shows the time resolution and $1/\sqrt{N_{pe}}$ of each side. To check this correlation, we selected the several rigidity region of proton event and calculated the time resolution and N_{pe}. The time resolution of short fiber side at $1/\sqrt{N_{pe}} \sim 0.25$ is about 100 ps better than the resolution of long fiber side. The difference of time resolution probably comes from the difference of the light guide. The propagation length of scintillating photons in the fiber bundles depends on the injection angle of scintillating fiber. Therefore, the fluctuation of propagation time in long fiber bundles is expected to be higher than short fiber bundles. It makes the reduction of time resolution for long fiber side with same N_{pe}.

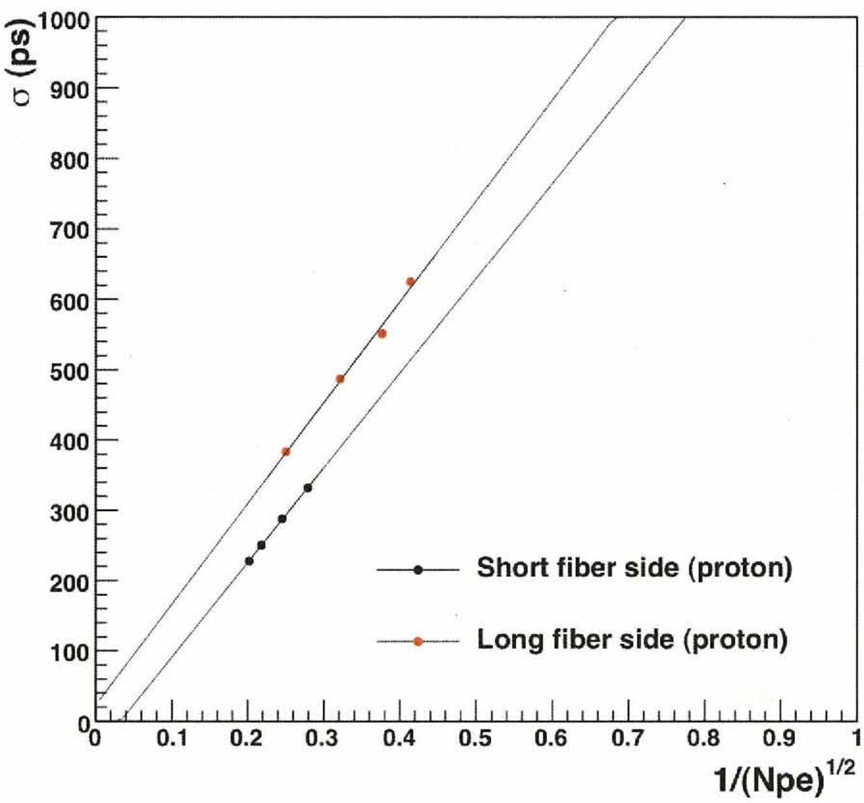

Figure 6.8: The correlation between time resolution and N_{pe} with several rigidity region of proton event.

6.1.5 Axial position resolution of BESS-Polar II Middle TOF

The axial position information of TOF is used for the quality cut to exclude the interaction and noise hit event. The axial position of TOF is calculated by following equation.

$$z_{\mathrm{TOF}} = \frac{t_{1c(3c)} - t_{2c(4c)}}{2} V_{\mathrm{eff}} \tag{6.1}$$

$$dz = z_{\mathrm{trk}} - z_{\mathrm{TOF}} \tag{6.2}$$

dz is the axial position difference between axial position calculated from JET/IDC and TOF. Figure 6.9 shows the dz distribution of the Middle TOF the axial position resolution of the Middle TOF is 45 mm for relativistic protons. The BESS-Polar I Middle TOF cannot acquire the axial position information because the BESS-Polar I Middle TOF is single-sided readout.

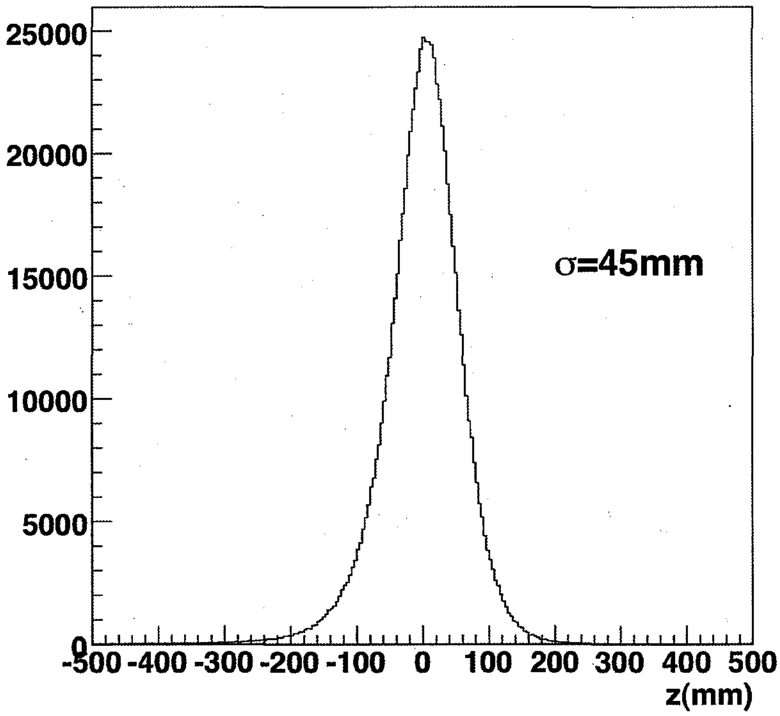

Figure 6.9: The dz distribution of the Middle TOF. The axial resolution of the Middle TOF is 45 mm for relativistic protons.

6.2 Event selection for the particle identification

This section describes the event selection for the identification of antiprotons with the Upper TOF and the Middle TOF. The event selection for the identification of antiprotons is mainly divided in two steps, "pre-selection" and "quality cut". Pre-selection defines the starting samples to undergo the succeeding event selection. And quality cut selects events with good measurement.

6.2.1 Pre-selection

At the first stage of the event selection, allowing cut are implemented to remove un-resonstructable events to obtain fully contained events in the fiducial region without interactions.

1. $\mathrm{N}_{\mathrm{longTK}} = 1$
   The number of long track should be only one. The "long" track is defined as a track where the number of hits inside JET is larger than 60% of $\mathrm{N}_{\mathrm{expect}}$. $\mathrm{N}_{\mathrm{expect}}$ is the number of JET hits expected from the trajectory calculated for each track.

2. $\beta > 0$
   Albedo (up-going) particles are eliminated. Because we intend to identify the antiprotons comes from the space.

3. $\mathrm{N}_{\mathrm{expect}} \geq 32$, $\mathrm{N}_{\mathrm{center}} > 0$
   $\mathrm{N}_{\mathrm{expect}}$ is described above. $\mathrm{N}_{\mathrm{center}}$ is defined as the expected number of hits in the central region of JET chamber. This cut defines the fiducial region in r-ϕ plane to eliminate the track which scratches the most outer region.

4. $|X_{\mathrm{TKU}}| < 55$ mm, $|X_{\mathrm{TKM}}| < 20$ mm
   In the r-ϕ plane the extrapolated trajectory should pass through the top and bottom hit TOF counters. $X_{TKU,M}$ represent the hit position from the center of the hit TOF counter. This condition ensures that the track information and the hit TOF counter are related to the same particle.

5. $|Z_{\mathrm{TKU}}| < 450$ mm, $|Z_{\mathrm{TKM}}| < 450$ mm
   By extrapolating the track trajectory found in the JET chamber, the expected hit positions at the Upper TOF and the Middle TOF are calculated. This cut defines the fiducial region in the yz-plane, and ensure that a particle should pass through the TOF scintillator area.

6. $N_{\mathrm{JET}} < 100$
   Since it is difficult to derive correct information from extremely noisy events, the number of JET hits not concerned with the track is limited.

7. $N_{\mathrm{TOFU}} = 1, N_{\mathrm{TOFM}} = 1$ or 2
   There should be only one hist in the Upper TOF, and one or two hits in the Middle TOF. The different selection for the Middle TOF is applied to save events with crosstalk.

6.2.2 Quality cut

The main purpose of following "quality cut" is to ensure correct measurements for the appropriate estimation of the incident energy.

1. $\chi^2_{r\phi} < 8$, $\chi^2_{yz} < 12$
   The quality of trajectory fitting is checked by using the reduced chi-square.

2. $\mathrm{dz_{TKU}} < 100$, $\mathrm{dz_{TKM}} < 200$
   Expected hit position in the TOF counter along the z-coordinate can be determined from extrapolation of the trajectory found in JET chamber (Z_{track}), and also determined by using the time difference between two signals from the both ends of the TOF counter (Z_{UTOF}, Z_{MTOF}). Two values of the hit position should be consistent.

Table 6.1 shows the summarizes the event selection for two configurations. Figure 6.10 and Figure 6.11 show the distribution of each cut parameters.

Table 6.1: Summary of the event selection.

Pre-selection	
Number of long track	$\mathrm{N_{longTK}} = 1$
Expect hits in JET	$\mathrm{N_{expect}} \geq 32$, $\mathrm{N}_{center} > 0$
x hit position in UTOF	$\lvert X_{\mathrm{TKU}}\rvert < 55$ mm
x hit position in MTOF	$\lvert X_{\mathrm{TKM}}\rvert < 20$ mm
z hit position in TOF	$\lvert Z_{TKU,M}\rvert < 450$ mm
Hits other than track	$\mathrm{N_{JET}} < 100$
Albedo rejection	$\beta > 0$
Quality cut	
χ^2 in trajectory fitting	$\chi^2_{r\phi} < 8$, $\chi^2_{yz} < 12$
UTOF hit consistency	$\mathrm{dz_{TKU}} < 100$ mm
MTOF hit consistency	$\mathrm{dz_{TKM}} < 200$ mm

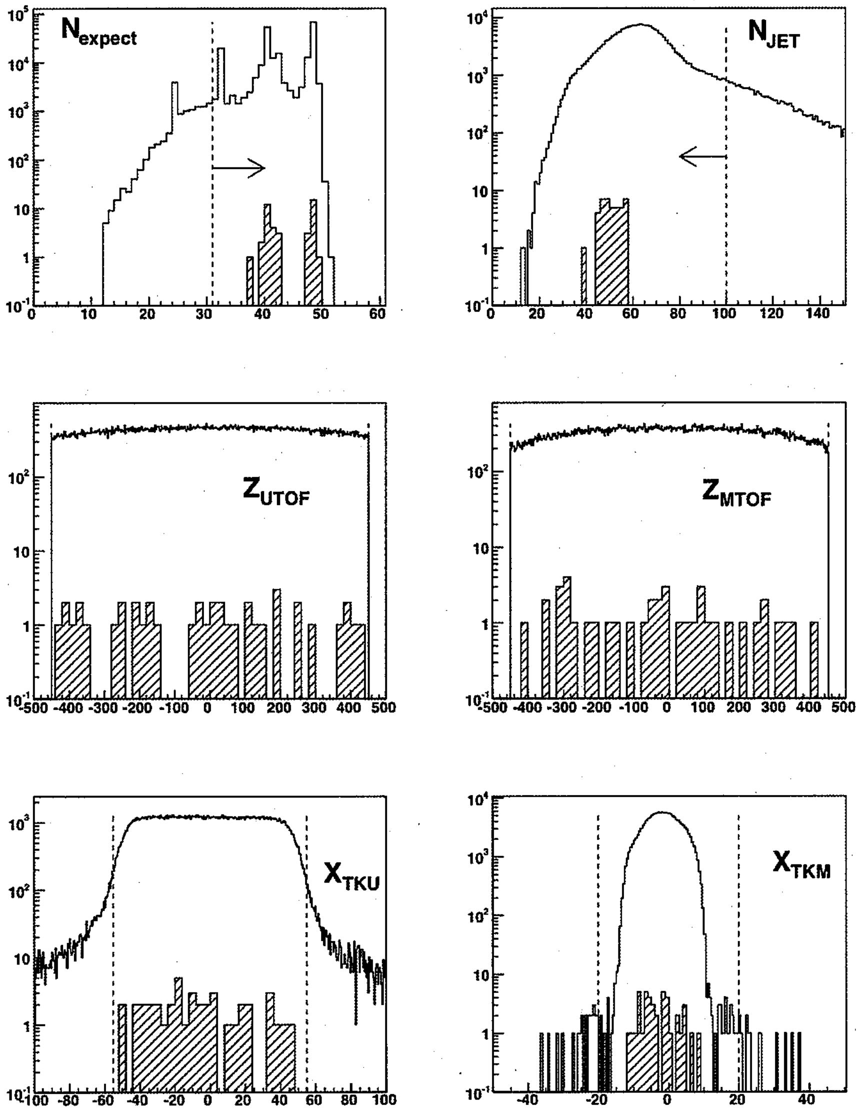

Figure 6.10: Distribution of pre-selection cut parameters for antiprotons (filled histogram with 35% statistics of BESS-Polar II flight) and proton (open histogram with 1 run).

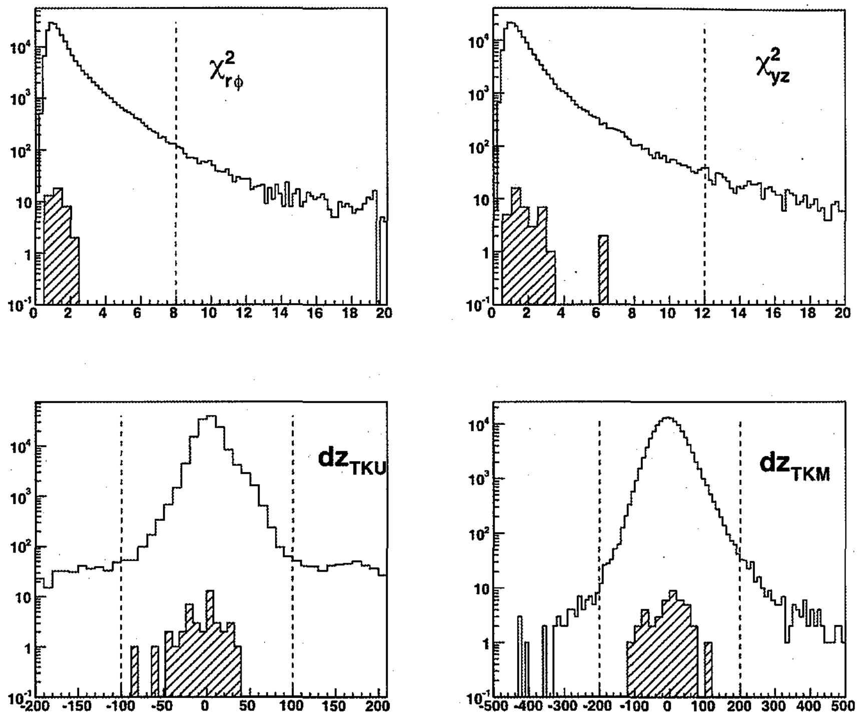

Figure 6.11: Distribution of quality cut parameters for antiprotons (filled histogram with 35% statistics of BESS-Polar II flight) and proton (open histogram with 1 run).

6.3 Identification of antiprotons

In this section, we describe the identification of antiprotons after the above event selection. We applied following cuts for the identification of antiprotons.

6.3.1 dE/dx-band cut

Figure 6.12 shows the scatter plots of dE/dx vs rigidity at the Upper TOF, the Middle TOF, and JET. It is clear to observe bands of proton, muon/pion/electron, deuteron, and He. We utilize the band structures in Figure 6.12 to extract antiprotons among other species with charge $|Z| = 1$. The solid line define boundaries of the dE/dx-band cut. We require that antiprotons as well as protons must have dE/dx in this boundaries. As for low energy antiprotons, they occasionally annihilates in the lower half of the detector or inside the counter itself. In this case, dE/dx in the Middle TOF may be different from the calculated proton's values, since another particles than the incident particle transverse the scintillation counters. Therefore, boundaries for the Middle TOF counters are loosen in the lower rigidity region.

6.3.2 Identification of cosmic-ray antiprotons

Particle mass are related to rigidity R, β and charge Z as

$$m = ZeR\sqrt{1/\beta^2 - 1} \tag{6.3}$$

Since we already selected $|Z| = 1$ particles with "dE/dx-band cut", we can identify antiproton candidates by using rigidity and β. Figure 6.13 shows the identification plot (ID-plot) of BESS-Polar II with the Upper TOF and the Middle TOF. The statistics is 35% of BESS-Polar II flight data. The minimum kinetic energy of antiprotons for BESS-Polar II is ~0.11 GeV. We realized the detection of low energy antiprotons as we expected.

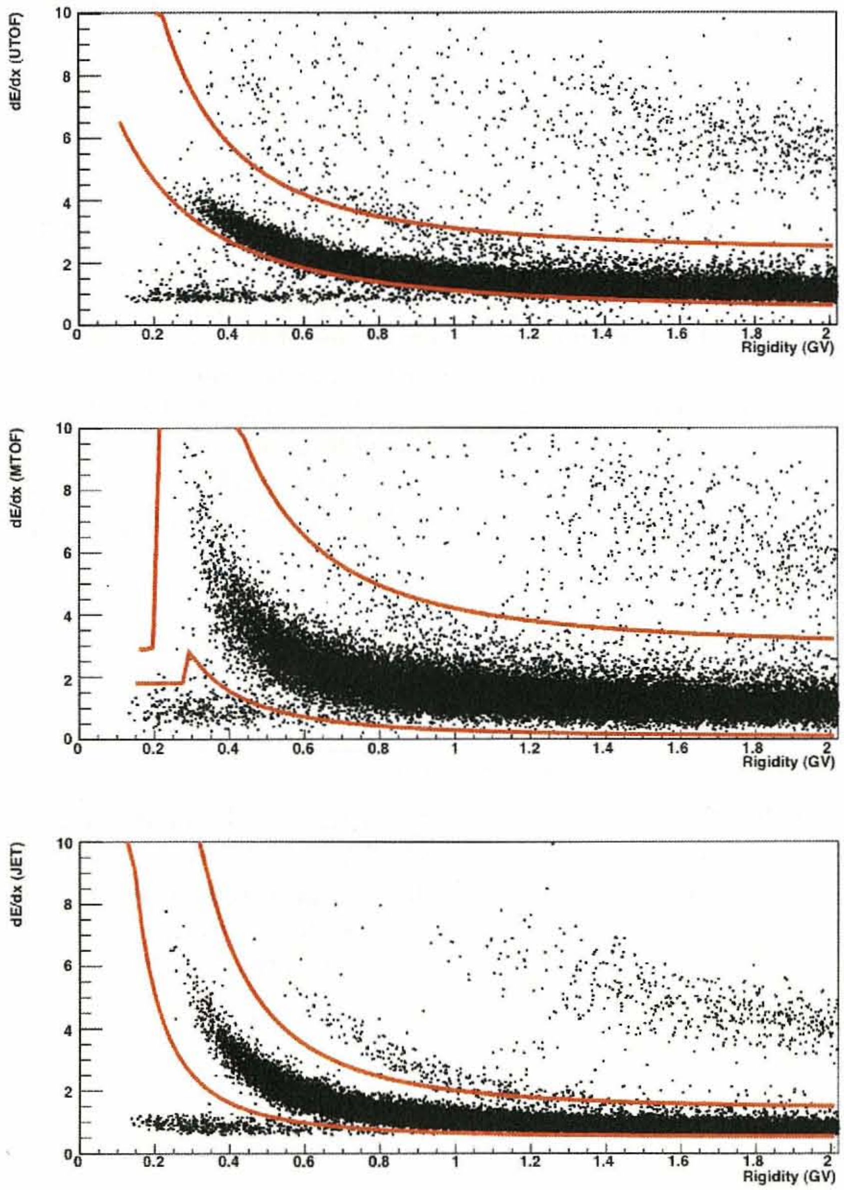

Figure 6.12: dE/dx vs Rigidity plots in each detector. Solid lines represent selection boundaries for proton. (top) dEdx distribution of Upper TOF, (middle) Middle TOF, and (bottom) JET/IDC.

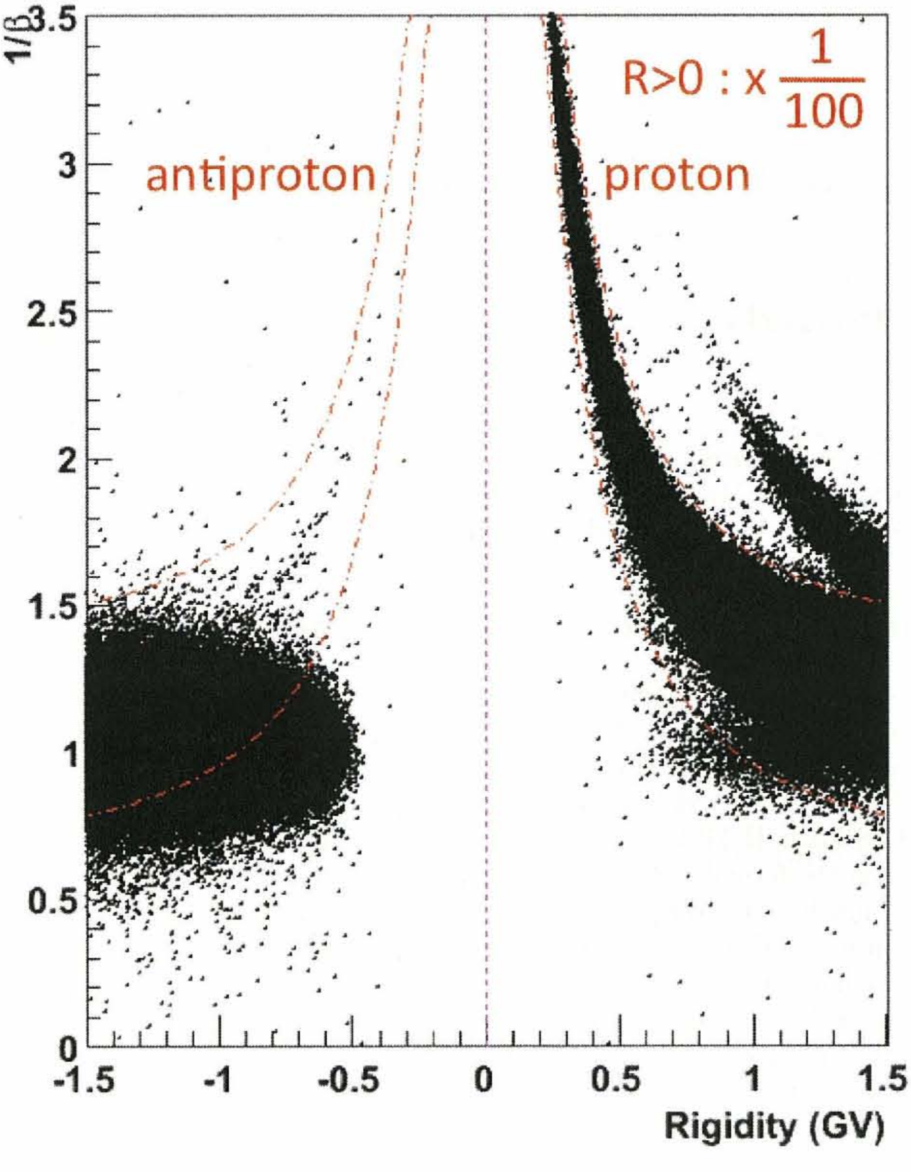

Figure 6.13: The particle identification plot of BESS-Polar II with the Upper TOF and the Middle TOF. The statistics is ~35 % of BESS-Polar II flight data. The dashed lines indicate the proton identification band. The antiproton candidates are placed within this band. In this ID-plot, the positive charge particles (R > 0) are selected once every 100 events.

Chapter 7

Discussion

In this chapter, we discuss improvement of the BESS-Polar II Middle TOF in comparisons with the BESS-Polar I Middle TOF. All the improvements achieved have been based on the double-sided readout in the BESS-Polar II Middle TOF.

7.1 Improvement of time resolution

Figure 7.1 shows the ΔT resolution of BESS-Polar I and the BESS-Polar II Middle TOF. The ΔT is defined by (T_{MTOF} - T_{UTOF}) - T_{trk} as already described in the formulae 3.7. The ΔT resolution of BESS-Polar II is 315 ps, and much better than that of BESS-Polar I case.

Figure 7.2 shows the axial position dependence of time resolution of the BESS-Polar I and the BESS-Polar II Middle TOF. The time resolution is calculated by $\sigma(\Delta T)$ and σ_U as described in the formulae 3.10. As shown in the figure, the BESS-Polar II Middle TOF has achieved much better time resolution at whole position, and the position dependence is drastically improved to be much smaller.

Figure 7.3 shows the time resolutions for each rigidity. The enhancement of $\mathrm{N_{pe}}$ at low rigidity region makes the higher time resolution. For the low rigidity region ($\sim$0.5 GV) where we identify the antiprotons with the Middle TOF, the time resolution is about 240 ps which is better than relativistic protons.

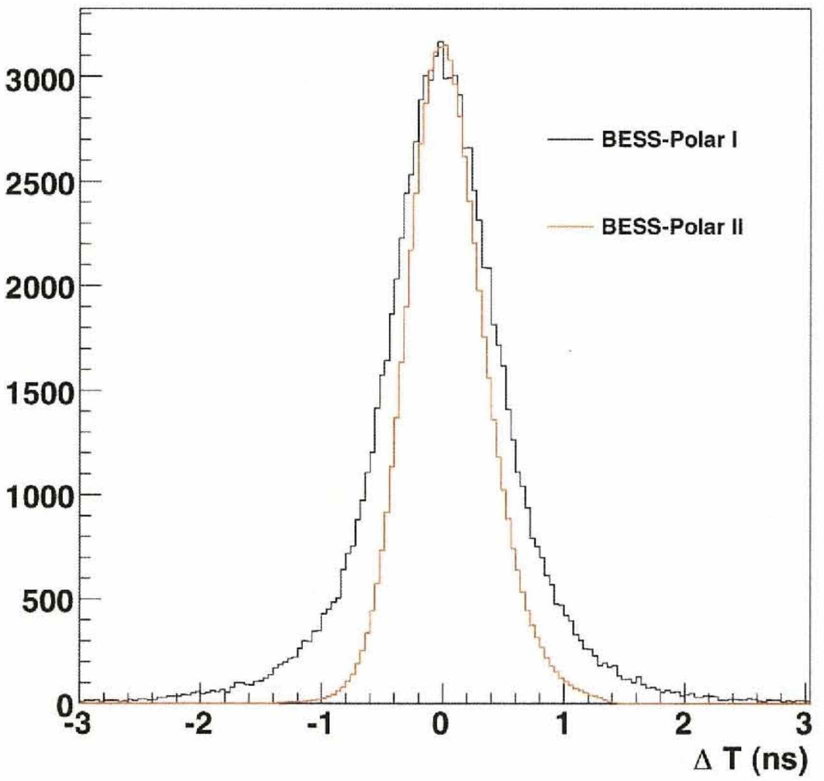

Figure 7.1: ΔT resolution of the BESS-Polar I Middle TOF and the BESS-Polar II Middle TOF. The ΔT resolution of BESS-Polar I is 480 ps. The ΔT resolution of the BESS-Polar II Middle TOF is 315 ps.

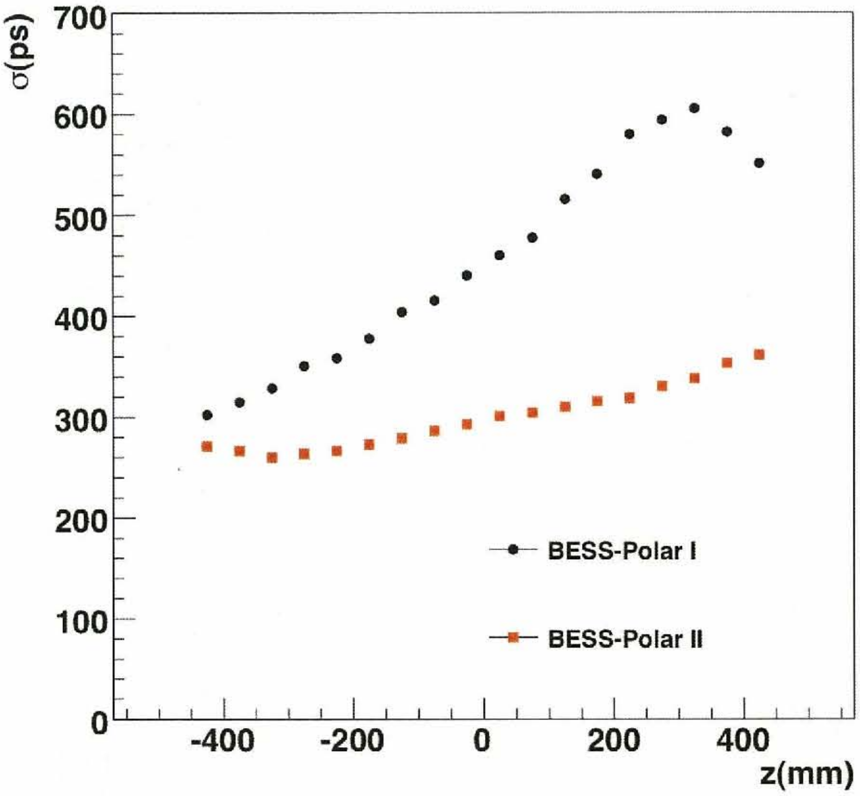

Figure 7.2: Time resolution of BESS-Polar I and the BESS-Polar II Middle TOF depend on axial position. The time resolution of the BESS-Polar II Middle TOF always better than that of the BESS-Polar I Middle TOF. The position dependence of time resolution is clearly better than the BESS-Polar I Middle TOF. These improvements come from the selection of scintillator and fiber bundle, and the weighted average with double side readout.

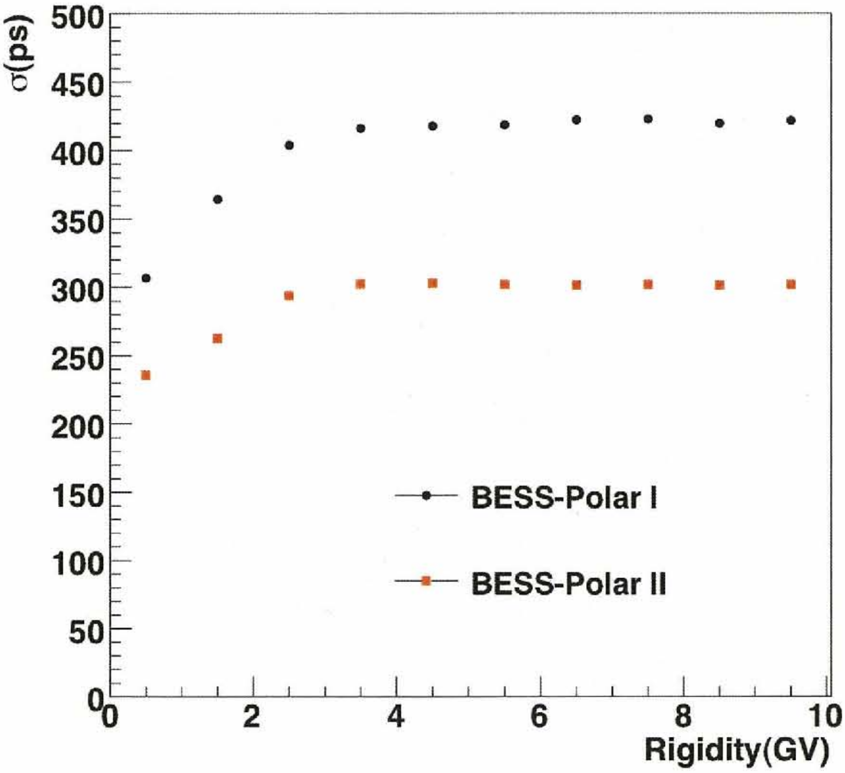

Figure 7.3: The correlation between time resolution and protons with several rigidity region of proton event. The enhancement of N_{pe} at low rigidity region makes the higher time resolution.

7.2 Improvement in the quality of particle identification by using axial position information

The BESS-Polar II Middle TOF newly provides us the information of the axial hit position. This information is very useful to enhance the quality of event selection. The consistency of axial position information between the JET/IDC and the Middle TOF is very important to confirm the quality of track reconstruction and the calculation of the hit time. If the axial position of the JET/IDC is true, we can derive the correlation of dz cut and $\Delta \mathrm{T}_i$ of the Middle TOF. The dz is described as follows using equation (3.2), (3.3), and (6.1):

$$dz = \frac{V_{\text{eff}}}{2}(T_3 - T_4) = \frac{V_{\text{eff}}}{2}(\Delta T_3 - \Delta T_4) \tag{7.1}$$

$$\Delta T_i = T_i - T_{\text{UTOF}} - T_{\text{trk}} \tag{7.2}$$

Therefore, the boundary of dz cut (|dz| <200 mm) has linear correlation between ΔT_3 (Long fiber side) and ΔT_4 (Short fiber side). Figure 7.4 shows the scatter plot of ΔT_3 and ΔT_4. As shown in Figure 7.4, there are events which have the large $\Delta T_{3(4)}$ and the small $\Delta T_{4(3)}$ (~ 0). Such kind of events which are not consistent with the hit time between two readout are clearly excluded by the dz cut.

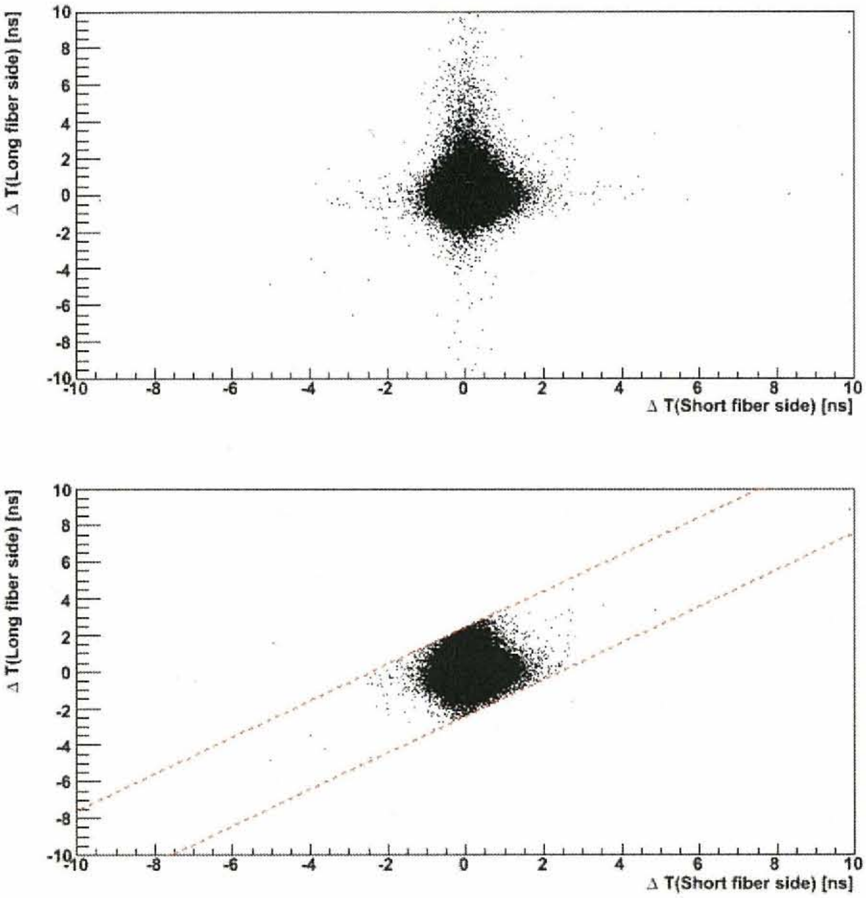

Figure 7.4: The scatter plot of ΔT_3 and ΔT_4. (top) without dz cut. (bottom) with dz cut. The red-dash lines indicate the boundary of dz cut as described in equation 7.1. If we use dz cut, we can clearly exclude the events which are not consistent with the hit time between two readout of the Middle TOF.

The excluded events by dz cut are categorized into two types as follows.

1. $\Delta T_3 > 0$: ΔT_3 distribution have the tail for $\Delta T_3 > 0$ region.

2. $\Delta T_i << 0$: One side of ΔT_i is quite smaller than the other side of ΔT.

At first, we describe the first type of events. It is very difficult to understand the tail of ΔT_3. Figure 7.5 shows the ΔT_i distributions of each readout. If we think about the behavior of the scintillating photons in the fiber bundle, we can guess the reason of this tail.

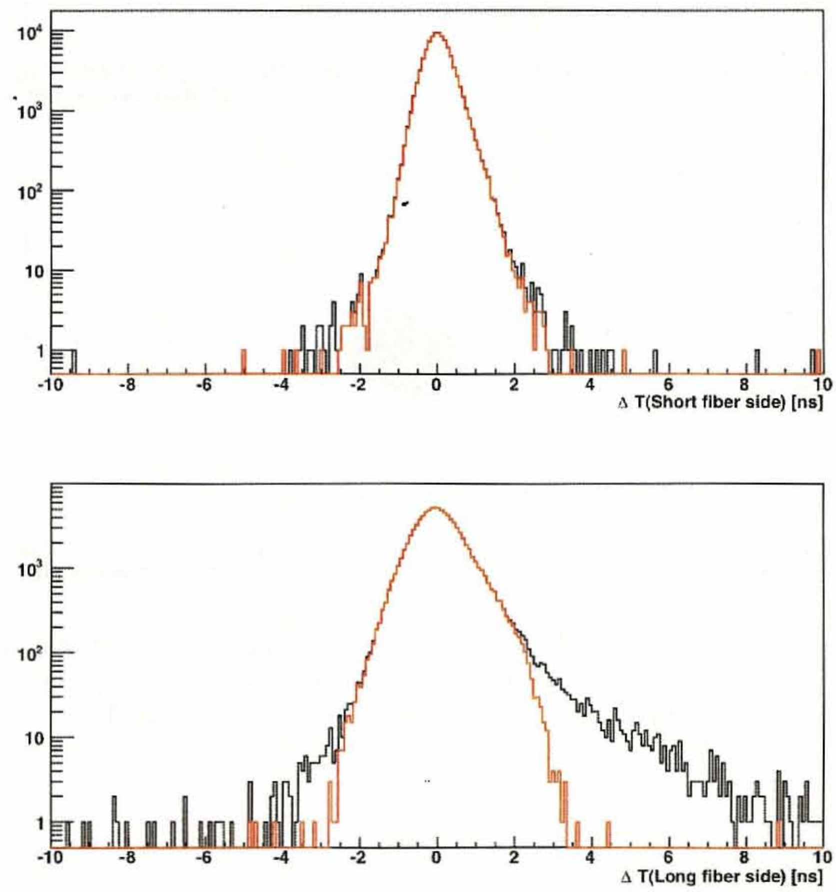

Figure 7.5: The ΔT_i distributions of each readout. (top) Short fiber side readout. (bottom) Long fiber side readout. The black lines indicate the distribution without dz cut. The red lines indicate the distribution with dz cut. There are large tail for long fiber side readout.

The path length of scintillating photon in the fiber bundles strongly depends on the injection angle of the fiber. The propagation time of scintillating photons in the fiber bundles depends on the injection angle. The maximum injection angle is calculated as follows.

$$\theta_{\text{max}} = \sin^{-1}\left(\frac{n_{\text{clad}}}{n_{\text{core}}}\right) = 24.5^{\circ}$$
$$n_{\text{core}} = 1.59, \quad n_{\text{clad}} = 1.49$$

We can expect the maximum time difference of the propagation time in fiber. Table 7.1 shows the expected propagation time in the each fiber bundles. The difference of propagation time of long fiber side is 4 times larger than that of the short fiber bundles.

Table 7.1: The propagation time in the fiber bundles depends on the incident angle.

	700 mm fiber side readout	3000 mm fiber side readout
Injection angle 0°	3.72 ns	15.9 ns
Injection angle 24.5°	3.97 ns (+0.25 ns)	17.0 ns (+1.1 ns)

There are two difference between the short fiber side and the long fiber side. The first difference is the length of fiber bundles. The second difference is the N_{pe}. If we check Figure 6.8, the time resolution of the long fiber side is much worse than that of the short fiber side for the same N_{pe}. One of the reason is the fluctuation of propagation time in the fiber as shown in Table 7.1. The fluctuation of the propagation time in the long fiber is 1.1 ns which is four times worse than that of the short fiber side. If there are sufficient scintillating photons from scintillator, the faster scintillating photons make the TDC trigger. However, N_{pe} of long fiber side is about 5.5 photo-electron for the relativistic particles. The possibility of faster scintillating photons in the long fiber is smaller than that of the short fiber side. The long fiber and the low N_{pe} probably make the tail of ΔT distribution. Even if we correct the time-walk effect, we cannot correct the fluctuation of the propagation in the long fiber. Figure 7.6 shows the schematic view of this problem.

We have to reject such kind of events because we identify each particles by rigidity and $1/\beta$ which is derived by Time-of-Flight. If we do not exclude the tail, we get the background contamination for the identifications of each particles.

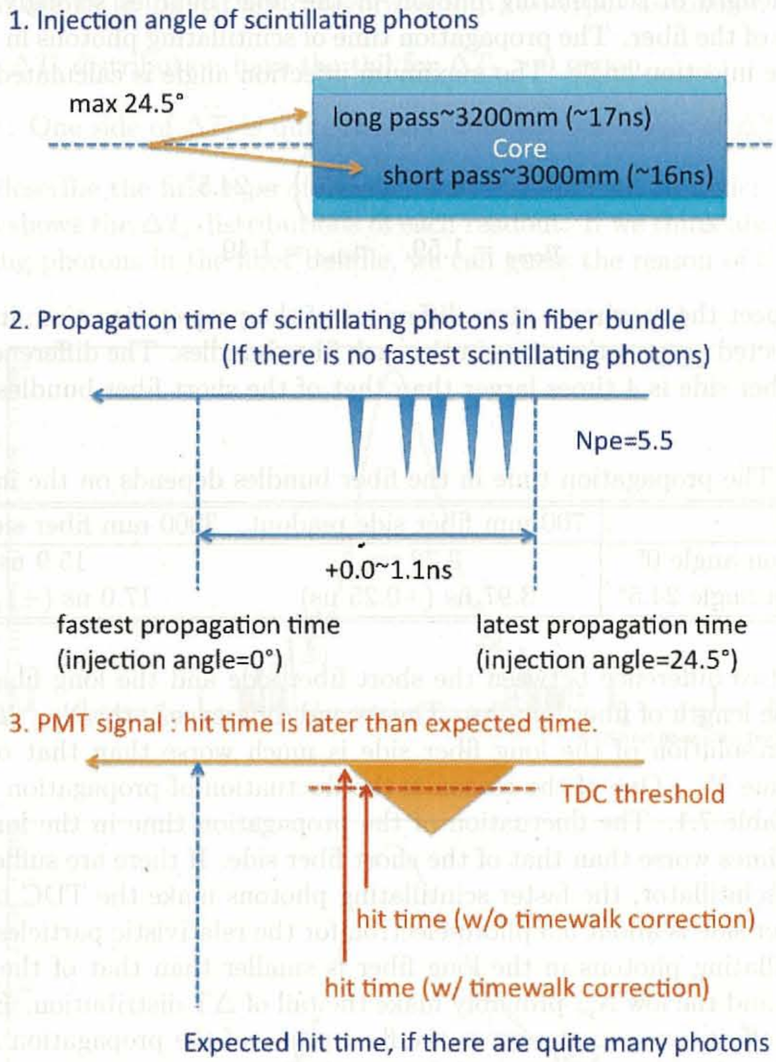

Figure 7.6: The schematic view of the measurement of hit time with low N_{pe} and long fiber bundle. If the injection angles of all scintillating photon are much larger than 0 degree, the hit time with time-walk correction is slower than ideal hit time. We cannot correct the fluctuation of the propagation time in the long fiber. Such kind of events probably make the tail of ΔT_3 distribution.

If there are high N_{pe} for the long fiber side, the tail of long fiber side should be reduced because the possibility of the fast propagation time in all scintillating photons probably enhance. Figure 7.7 shows the ΔT_3 distributions for each rigidity. For the low rigidity region, the N_{pe} is higher than the relativistic region because the energy loss of the protons enhance at the low rigidity region. The tail of ΔT_3 almost vanish for low rigidity region which is used for the particle identification of antiprotons by the Middle TOF.

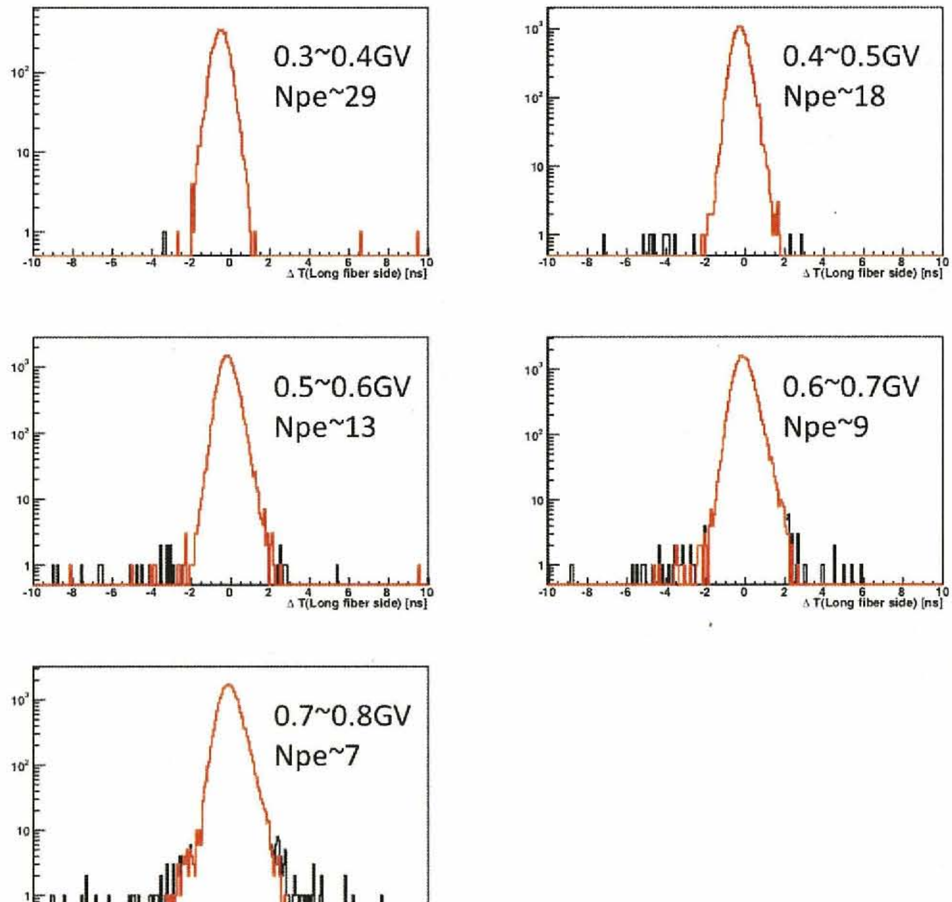

Figure 7.7: The ΔT_3 distributions depend on rigidity. (black) without dz cut. (red) with dz cut. For the low rigidity region, the N_{pe} is higher than the relativistic region. The tail of ΔT_3 vanish for the low rigidity region which is used for the particle identification of antiprotons by the Middle TOF.

The other type of events probably come from the noise trigger event. Figure 7.8 shows the one example of the noise trigger candidate. The ΔT_4 (short fiber side readout) is almost zero. On the other hand, the ΔT_3 (long fiber side readout) is much faster than the ΔT_4. For such kind of events, there is no consistency between $z_{\rm trk}$ and $z_{\rm MTOF}$. The noise trigger event is clearly excluded by the dz cut.

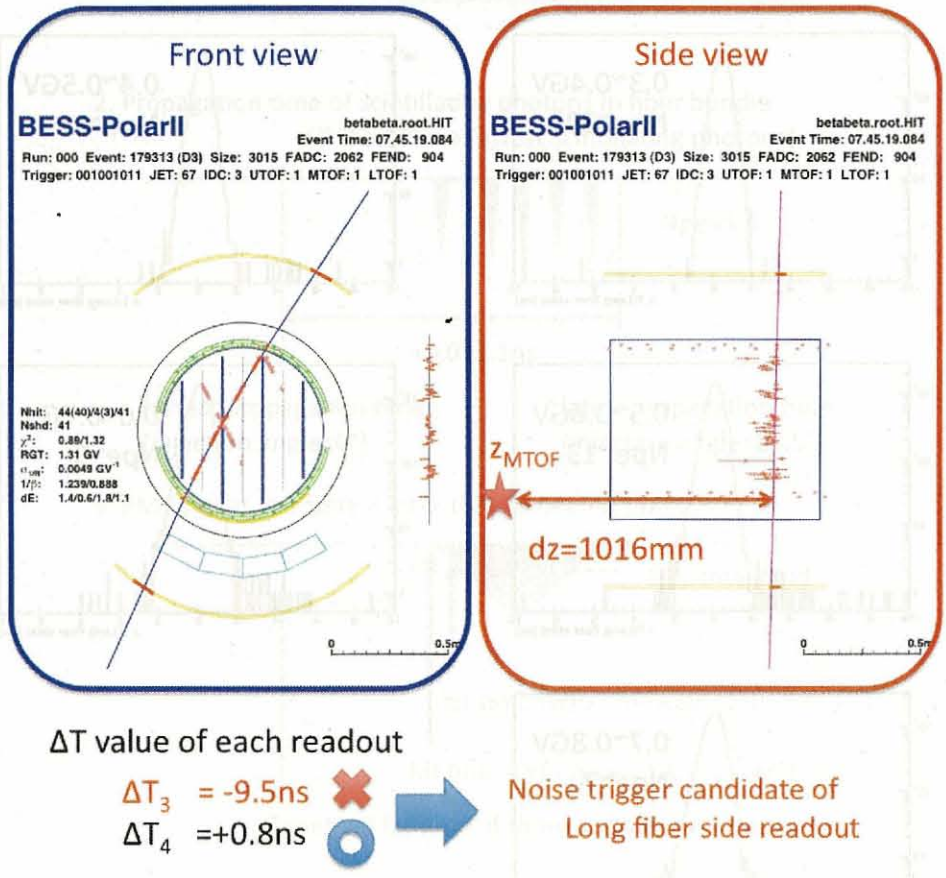

Figure 7.8: The example of noise trigger event. The ΔT_4 (short fiber side readout) is almost zero. On the other hand, the ΔT_3 (long fiber side readout) is much faster than the ΔT_4. Such kind of events have quite large dz value, it is very easy to exclude noise trigger event by dz cut.

Table 7.2 shows the effect of dz cut using the plots of Figure 7.7. For the relativistic particles, the rejected events are about 2 % of the total event (before the dz cut). The tail events of ΔT are 1.9 % of the total event. The noise trigger candidates are only 0.1 %.

For the low rigidity particles, the time resolution of the Middle TOF enhance and the tail of ΔT_3 vanish. Thus, the dz cut exclude the noise trigger event for the low rigidity region without strongly rejecting the signal region. The dz cut is very effective to reject the noise trigger events of the Middle TOF.

Table 7.2: The effect of dz cut. For the low rigidity region, the ratio (with dz cut/without dz cut) is >99.5 % for the low rigidity regions.

	without dz cut (events)	with dz cut (events)	ratio (with dz cut/without dz cut)
0.3-0.4 GV	4230	4226	99.9 %
0.4-0.5 GV	12143	12123	99.8 %
0.5-0.6 GV	17830	17795	99.8 %
0.6-0.7 GV	21456	21403	99.7 %
0.7-0.8 GV	24419	24321	99.5 %
5 GV $\sim$	82552	80881	98.0 %

Figure 7.9 shows the particle identification plots. ID-plot without dz cut shows the events which appear to exceed light speed. Such kind of events is probably noise trigger event because the Time-of-Flight is much faster than expected value. These events are efficiently rejected by dz cut as shown in the ID-plot with dz cut. The quality of particle identification is improved by dz cut of the Middle TOF.

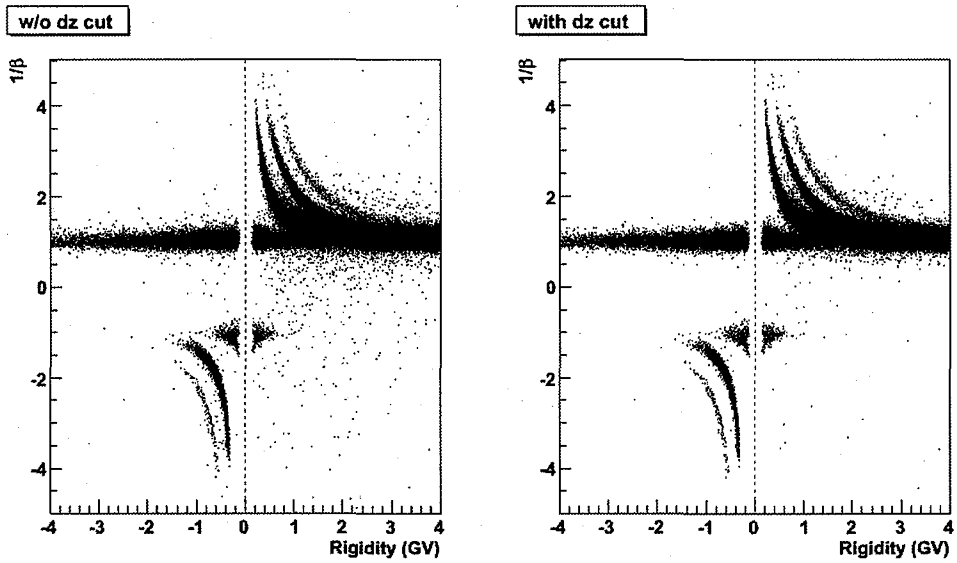

Figure 7.9: The particle identification plots (ID-plots) of BESS-Polar II with the Upper TOF and the Middle TOF. (left) ID-plot without dz cut, (right) ID-plot with dz cut. There are events which exceed the light speed (around $1/\beta \sim 0$). These events are efficiently rejected by dz cut as shown in the ID-Plot with dz cut.

7.3 Improvement in antiproton identification

Figure 7.10 shows the identification plot of BESS-Polar I and BESS-Polar II. The proton band of BESS-Polar II becomes much thinner than that of BESS-Polar I because of the improvement of time resolution. The event quality of BESS-Polar II is improved, it is a effect given by the dz cut.

Both improvement comes have been resulted from the double-sided readout of the Middle TOF in BESS-Polar II.

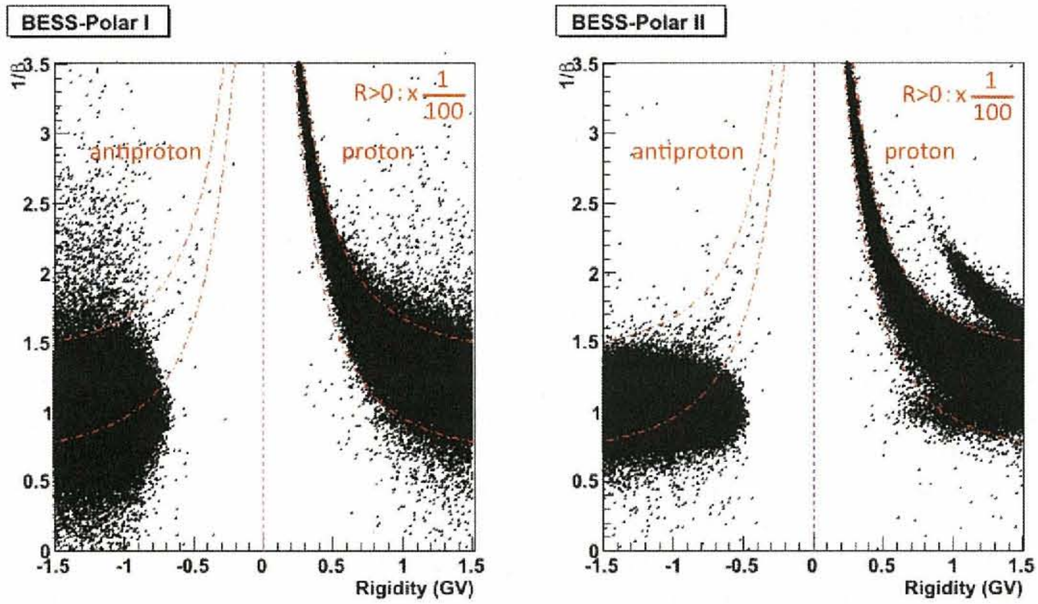

Figure 7.10: The particle identification plot of (left) BESS-Polar I and (right) BESS-Polar II with the Upper TOF and the Middle TOF. The statistics of BESS-Polar I is all flight data. The statistics of BESS-Polar II is ~35% of flight data. The dashed lines indicate the proton identification band. The antiproton candidates are placed within this band. In these ID-plots, the positive charge particles (R > 0) are selected once every 100 events.

Chapter 8

Conclusion

The BESS-Polar experiment has been carried out with an important objective to search for novel sources of primary antiprotons such as evaporation of Primary Black Holes (PBHs) with Hawking's radiation and annihilation of neutralino dark matter, in a detectable lowest energy region in cosmi-rays with long duration balloon flight in Antarctica. The Middle TOF counter in the BESS-Polar spectrometer has taken an essential role to realize detection of the lowest energy antiproton at a level of 0.1 GeV.

Based on experiences integrated in the BESS-Polar I experiment with a single-sided, signal readout in the Middle TOF, we have designed and developed entirely new Middle TOF counters with double-sided signal readout with much improving the performance in terms of axial information and the spatial information. We finally realized the double-sided readout Middle TOF with overcoming much difficulty in layout and the installation of the light-guides because of extremely limited space available.

The BESS-Polar II experiment was carried out with a NASA long duration balloon flight over Antarctica in December 2007 through January 2008. During this successful flight, the BESS-Polar II superconducting spectrometer collected 4.7 billion cosmic-ray events without any online event selection cuts and it acquired about five time statistics compared with the previous flight. BESS-Polar II Middle TOF was worked well as expected during the flight.

The BESS-Polar II Middle TOF realized the improvement of time resolution. The time resolution of the BESS-Polar II Middle TOF is 306 ps which is about 140 ps better than that of the BESS-Polar I. Furthermore, the BESS-Polar II Middle TOF acquired the axial position information because of the double-sided readout. The consistency of axial position between JET/IDC and the Middle TOF enhance the quality of the time measurement. The rejected events are about ~ 0.5 % of the events before the dz cut. One of the rejected events by the consistency of axial position are the noise trigger event. If there are the noise trigger event, there are possibility to mistake the identifications of each particles. The axial position information of the Middle TOF is very important to keep the reliability of Time-of-Flight.

The BESS-Polar II Middle TOF successfully contributed to realize the lowest energy antiproton measurement as a level of 0.1 GeV in cosmic-ray, and it has been critically important to search for novel source of primary antiprotons in cosmic rays.

Bibliography

[1] I. V. Moskalenko et al., Astrophys. J. 565 (2002) 280.

[2] S. W. Hawking, Mon. Not. R. Astron. Soc. 152, 75 (1971).

[3] K. Yoshimura et al., Adv. Space Res. 27 (4) (2001) 693

[4] S.W. Hawking, Commun. Math. Phys. 43 (1975) 199.

[5] K. Maki, T. Mitsui, S. Orito, Phys. Rev. Lett. 76 (1996) 3474.

[6] T. Sjöstrand, Comput. Phys. Commum. 82 (1994) 74.

[7] L. Bergström, et al., Astrophys. J. 526 (1999) 215.

[8] T.K. Gaisser, R.K. Schaffer, Astrophys J. 394 (1992) 174.

[9] T. Mitsui, Ph.D. thesis, University of Tokyo, 1996.

[10] I.V. Moskalenko, et, al., Astrophys J. 565 (2002) 280.

[11] T. Mitsui et al., Phys. Lett. B 389 (1996) 169.

[12] A. Yamamoto et al., Adv. Space Res. 42 (2008) 442.

[13] A. Yamamoto et al., Adv. Space Res. 30 (2002) 1253.

[14] J. W. Mitchell, et al., Nucl. Phys. B (Proc. Suppl.) 134 (2004) 31.

[15] T. Yoshida, et al., Adv. Space Res. 33 (10) (2004) 1755.

[16] A. Yamamoto et al., Adv. Space Res. 30 5 1253 (2002).

[17] Y. Ajima et al., Nucl. Instrum. Methods A 443 (2000) 71.

[18] S. Haino et al., Nucl. Instrum. Methods A 518 (2004) 167.

[19] S. Orito, et al., Phys. Rev. Lett. 84 (2000) 1078.

[20] A. Yamamoto et al., Phys. Lett. B 670 (2008) 103.

[21] K. Yoshimura et al., Adv. Space Res. 42 (2008) no.1664.

[22] Jane H. MacGibbon, Phys. Rev. Lett 44 (1991) 2.

[23] F. Halzen et al., Nature 353 (1991) 807.

[24] B.J. Carr, J.H. MacGibbon, Phys. Rep. 307 (1998) 141.

[25] J.W. Bieber, et, al, Phys. Rev. Lett 83 (1999) 674.

[26] L.A. Fisk, J. Geophys Res. 76 (1971), 221.

[27] K. Abe, et al., Phys. Lett. B 670 (2008) 103.

[28] N. Thakur et al., 31st Int. Cosmic Ray Conf. (Łódź), OG1.5 (2009).

[29] Y. Matsukawa, M.S. thesis (In Japanese), University of Kobe, 2008.

[30] W.B. Atwood, Time of flight measurements, SLAC-PUB-2620, October 1980.

[31] T. Tanimori et al., Nucl. Instr. and Meth. 216 (1983) 57.

[32] E. Chen et al., hep-ex/9606007.

[33] K. Sakai, private communication.

[34] M. Sasaki et al., Proc. 31st Int. Cosmic Ray Conf. (Łódź), OG1.51403 (2009).

[35] A. Kusumoto, M.S. thesis (In Japanese), University of Kobe, 2008.

[36] K. Sakai, private communication. He checked the residual atmospheric pressure and the altitude with the all flight data.

[37] K. Sakai, private communication. He rechecked the detector status with the all flight data.

[38] K. Yoshimura, et al., Phys. Rev. Lett. 75 (1995) 3792.

[39] A. Moiseev, et al., Astrophys. J. 474 (1997) 479.

[40] H. Matsunaga, et al., Phys. Rev. Lett. 81 (1998) 4052.

[41] S. Orito, et al., Phys. Rev. Lett. 84 (2000) 1078.

[42] T. Maeno, et al., Astropart. Phys. 16 (2001) 21.

[43] Y. Asaoka, et al., Phys. Rev. Lett. 88 (2002) 051101.

[44] R. Shinoda, M.S. thesis (In Japanese), University of Tokyo, 2008.

[45] V. Karimaki, Comput. Phys. Commun. 69 133 (1992).

[46] K. Sakai et al., 31st Int. Cosmic Ray Conf. (Łódź), OG1.5 (2009).

Appendix A

Progress of BESS experiment

A.1 Antiproton measurement with BESS experiment

BESS experiment carries out 9 flights [38–43] in 1993-2002 with continuous improvement in the instrument before the BESS-Polar experiments. Following is the improvement of BESS experiment.

1. Improvement of the time-of-flight resolution
2. Background elimination with a threshold-type aerogel Cherenkov counter
3. Data acquisition system and larger data storage capacity for better statistical accuracy
4. Rigidity resolution improvement with a new development of tracking chambers. (2001$\sim$)

Table A.1 summarizes 8 of these 9 flights for the antiproton measurements. Through 2002, total 16 hours of observation time and more than 2400 cosmic-ray antiproton have been identified.

As described above, antiproton measurement is the ideal probe for the "novel exotic sources". Though there were some identifications of a flatter spectrum from those sources in the low energy data from 1995 and 1997, large statistical errors could not allow a firm conclusion. Figure A.1 shows the antiproton spectra of BESS 95+97. The improvement of the statistics is inevitable for the antiproton measurement as the probe to its origin.

A.2 BESS-Polar experiment

The BESS long duration flight in Antarctica, BESS-Polar was prepared to extend the BESS scientific objectives under ideal ballooning environment at Antarctica. It aims at extremely sensitive measurements of low energy antiprotons to search for any novel primary origin and

Table A.1: Summary of BESS experiment.

Year	93	94	95	97	98	99	2000	2002
Float time (hours)	17.5	17.0	19.5	20.5	22	34.5	44.5	16.5
Observation (hours)	14	15	17.5	18.3	20.0	31.3	32.5	11.3
Number of event ($\times 10^6$)	4.0	4.2	4.5	16.2	19.0	16.8	15.0	11.8
Data volume (GB)	4.5	6.5	8.0	31	38	41	38	56
TOF resolution (ps)	300	300	100	75	75	75	75	75
Silica-aerogel index	none	none	none	1.032	1.020	1.020	1.020	1.020
$\overline{p}$ observed	6	2	43	415	384	668	558	147
$\overline{p}$ energy range (GeV)	0.18-0.5	0.18-0.5	0.18-3.6	0.18-4.2	0.18-4.2	0.18-4.2	0.18-4.2	0.18-4.2

at the same time to study the cosmic-ray propagation model. The BESS experiment, large geometrical acceptance, may maximize the advantage of long duration flights in Antarctica with a very low rigidity cut-off.

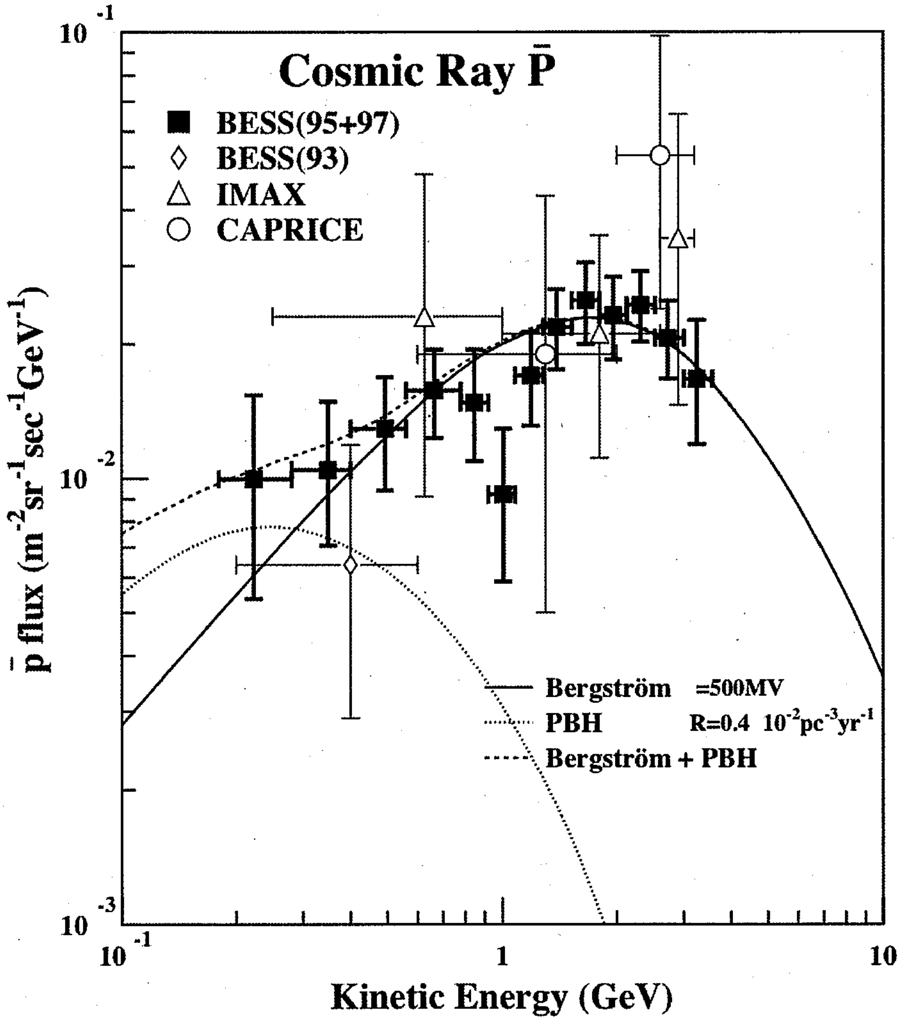

Figure A.1: BESS antiproton spectra (1993, 1995+1997) together with previous data and model calculation of secondary spectra

Appendix B

Experimental apparatus

This chapter provides an overview of the employed apparatus. In order to realize long duration and precise measurement over Antarctica, almost all of BESS-Polar II detector was newly developed [21]. We use hereafter a cylindrical coordinate system : r, ϕ, and z, and a Cartesian coordinate x, y, z, where y and z are the vertical axis and the axis of the solenoid, respectively.

B.1 Detector Layout

B.1.1 Detector Configuration

The detector components were arranged concentrically as shown in Figure B.1. A particle traversing the apparatus passes through, from outside to inside, a plastic scintillator hodoscope (TOF), a superconducting solenoid (MAG), two layers of inner drift chambers (IDC), before entering a central jet-type drift chamber (JET). An aerogel Cherenkov counter (ACC) sites between cryostat and the lower TOF hodoscopes. Furthermore, thin plastic

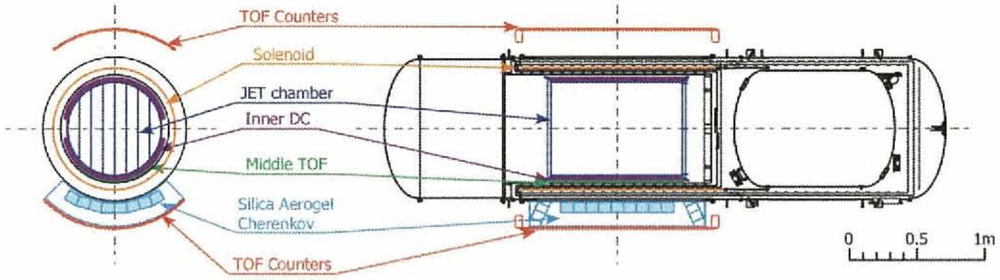

Figure B.1: Cross sectional view of BESS-Polar II spectrometer scintillator hodoscope (MTOF) is placed between lower IDC and the magnet bore for the detection of the lowest energy particle. Among these components, JET/IDC, and MTOF are contained in a magnet whose wall is also used as the pressure vessel. The upper and lower TOF counter and ACC are placed outside of the pressure vessel, i.e., in the vacuum during the flight.

The most distinctive feature of the BESS-Polar II detector is the cylindrical configuration with a solenoid magnet. Solenoid magnet configuration has been disfavored in previous cosmic ray experiments because of the unavoidable material in the particle passage. However, a thin superconducting solenoid developed at KEK enabled us to adopt this concentric configuration, which has many advantages in application to the cosmic ray measurements, as well as in the high energy collider experiments.

This cylindrical configuration gives a large geometrical acceptance while keeping the whole detector size compact. The uniform magnetic field of 0.8 T over the large tracking volumes assures an almost constant geometrical acceptance for a wide energy region. The acceptance changes only a few percent from the lowest detectable energy ($\sim$ 100 MeV) up to greater than 100 GeV. A large and transparent tracking system can be installed inside the solenoid. This tracking system can fully 'visualize' the incident track or any interaction inside the apparatus (Figure B.2). The detector performance changes little for various hit positions and incident angles. This characteristic is essential in the reliable determination of the absolute flux of the cosmic radiation.

B.1.2 Particle Identification

Particle identification in the BESS-Polar experiment is performed by mass reconstruction according to the relation

$$m = ZeR\sqrt{1/\beta^2 - 1}$$

The rigidity, momentum per charge (R≡pc/Ze), is precisely measured by the reconstructed particle trajectory. The velocity, β, is derived from the path length and the time-of-flight between the upper and lower/middle TOF. the The energy deposit in the TOFs provides the magnitude of the charge, Z, and additional information on the velocity according to the relation.

$$dE/dx \approx (Ze/\beta)^2 f(\beta)$$

The sign of charge is determined by the deflection measured by the JET/IDC and the particle direction, up-going or down-going, determined by the TOF. The mass is finally calculated from these measurements.

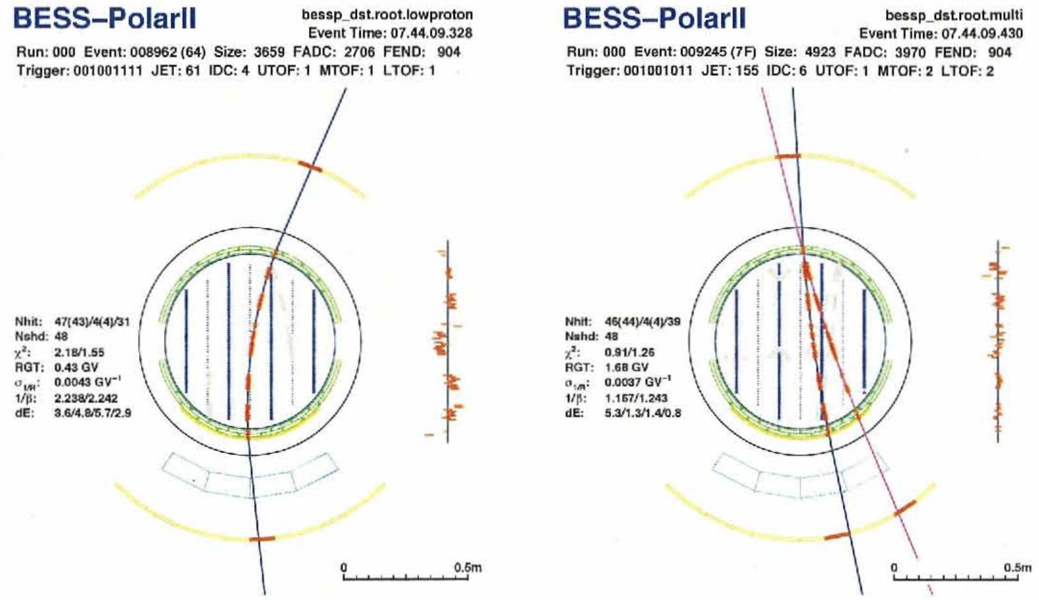

Figure B.2: Examples of event display collected during the flight. left : a typical single-track event. right : two track event showing the interaction.

B.1.3 Requirements as a balloon borne instrument

The requirements specific to a balloon-borne experiment necessarily limit the performance of the detector. Weight and power consumption are the primary issues. Since the lifting capacity of the balloon is limited, a heavier weight payload results in a lower balloon level altitudes, and more residual atmosphere above the instrument. Most of the electronics on board were specially designed for this experiments [34]. The functions of each module was carefully selected and minimized in order to simplify the circuits and to reduce their power consumption while keeping the signal processing speed as fast as possible. Low power consumption also benefits the temperature control of the payload. The local temperature near certain power consuming components increases when those components point to the sun and might reach the maximum tolerable level. The optimization of heat insulation and ventilation to stabilize the temperature inside the vessel becomes a difficult task for high power dissipation. For electronics outside the pressure vessel, or in the vacuum, the lower power consumption is more serious issue because of the difficulty in radiation. Furthermore, to avoid the increase of weight by primary battery for a long flight more than 10 days, we adopt solar battery system for the power source. Stray magnetic field is another issue. Since a magnet return yoke is too heavy to be loaded in the payload, a dipole magnetic field remains around detector. Any detector components sensitive to the magnetic field should be property treated. Detailed descriptions are given in the relevant sections.

As a balloon payload, the apparatus should be robust enough to withstand the impacts of launching, parachute opening and landing. It was estimated that a 10 G acceleration is applied to the detector. The support structure of each detector component was designed so that the shock of 10 G acceleration does not cause any fatal damage. As for the suspension system of the superconductor, we have performed mechanical analysis and have confirmed that the operating magnet did not quench during 10 G impact test.

B.2 Superconducting Solenoid

The superconducting solenoid magnet is the core component of the magnetic rigidity spectrometer [16,44]. The magnet was newly developed for the long duration flights over Antarctica and designed to provide uniform magnetic field in a large solid-angle acceptance while minimizing incoming particle interaction with the magnet wall material. The structure of BESS-Polar II solenoid magnet is based on BESS-Polar I solenoid magnet. The amount of material in the coil and its cryostat (2.46 g/cm^2) has been reduced to half of those in the BESS spectrometer (4.22 g/cm^2) before BESS-Polar I experiment. The superconducting coil was wound with aluminum-stabilized NbTi/Cu superconductor in two layers (flat-wise + low-wise in the central area, low-wise + low-wise in the axial ends), as shown in Figure B.3.

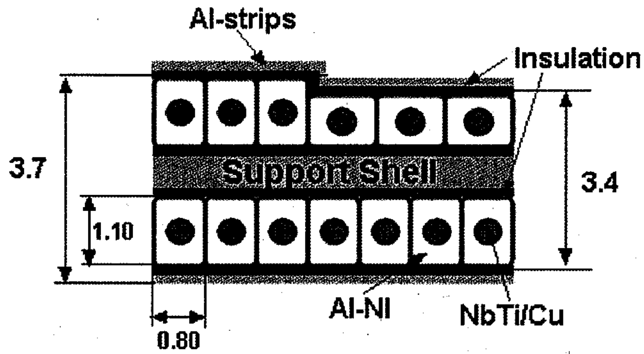

Figure B.3: Schematic cross-section of the superconducting solenoid.

A central magnetic field of 0.8 T was generated with a field of uniformity of 10 % in the central tracker (JET/IDC) with a wall transparency of 0.1 radiation length. The liquid helium reservoir of 520 liters was attached for long duration flight, and the lifetime of liquid helium was extended to more than 20 days (10 days in the BESS-Polar I magnet).

The solenoid coil was successfully tested up to a central magnetic field of 1.0 T and was operated at 0.8 T in the scientific balloon flight. Major parameters of solenoid magnet are summarized in B.1, in comparison with BESS-Polar I magnet.

Table B.1: Main Parameters of BESS-Polar II superconducting solenoid magnet in comparison with BESS-Polar I magnet

Dimensions	BESS-Polar	BESS Polar II
Coil diameter	0.9 m	0.9 m
length	1.4 m	1.4 m
thickness	3.38 mm	3.38 mm
Cryostat diameter	1.06 m	1.06 m
length	2.9 m	3.2 m
Central filed	1.0 T (0.8 T*)	1.0 T (0.8 T*)
Current	571 A (380 A*)	571 A(380 A*)
Wall thickness	2.46 g/cm^2 per wall	2.46 g/cm^2 per wall
Conductor	NbTi/Cu	NbTi/Cu
LHe Capacity	400 liters	520 liters
LHe lifetime	10 days	21 days

* In balloon operation

B.3 Tracking

B.3.1 JET Chamber

JET was located inside the warm bore (0.8 m in diameter and 1.1 m in length) of the solenoidal magnet, providing a particle trajectory in r-ϕ plane by drift time measurement and in z direction by charge division readout. Originally JET and IDCs were designed for the BESS-TeV experiment before BESS-Polar I, and also used in the BESS-Polar I and BESS-Polar II experiment with some improvements.

A schematic view of JET is shown in Figure B.4, and its parameters are summarized in Table B.2. The sensitive volume of JET is a cylinder of 1 m length and 620 mm in diameter.

JET is subdivided into four sections in vertical by cathode planes in which gold-plated aluminum wires of 200 μm in diameter are stretched at 4.0 mm interval. At the center of each section, there is a signal wire plane in which sense wires (gold-plated tungsten-rhenium alloy, 20 μm in diameter) are equally spaced at 8.0 mm intervals alternated with potential wires (gold-plated aluminum, 200 μm in diameter). Each of two central (side) sections contains 77 (51) sense wires. The sense wires are staggered by $\pm$300 μm from the center plane defined by the potential wires to resolve left-right ambiguity. The maximum drift distance of one section is 86.3 mm.

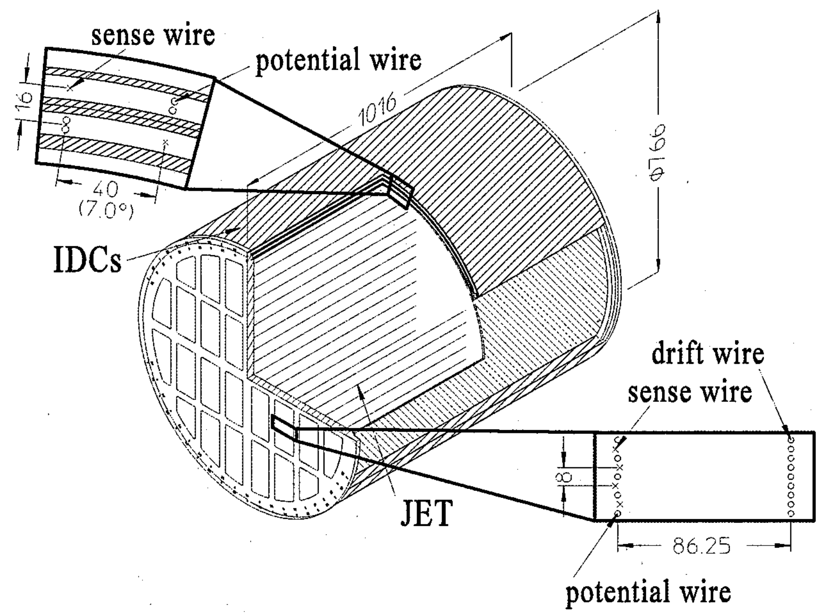

Figure B.4: Schematic view of JET and IDCs

The high voltages of the potential and cathode wires were -2.85 kV and -10.30 kV respectively. The sense wires are kept at ground potential. The electric field strength in the drift region is about 0.85 kV/cm, which corresponds to the maximum drift time of 13 mus using a pure CO_2 gas.

Every wire is positioned and fixed by a feed-through, that is located in a hole drilled through the end plate. The feed-through has a bush for positioning, a brass lead for soldering and a poly-phenylene oxide (PPO) sleeve for electrical insulation. The inner diameter of the bush is 270 μm for potential/cathode wires and 80mum for sense wires. The wire tensions are adjusted to be half their elastic limits to allow for deformation of the chamber due to temperature variation and acceleration impact.

In order to reduce weight and material, the wall of the cylinder was constructed with a composite panel. This panel consists of a core with 3 mm thick and two skins with 0.1 mm thick. The core was made of a thermoplastic foam, based on the azimuth were etched on the inner surface of the cylinder. Resistors connect the neighboring strips with proper resistance to form a uniform drift electric field.

The end plates were made of 25 mm thick GFRP, rigid enough to support a total wire tension of 3.1 kN. To reduce the weight many reprocess of depth 15 mm were scooped out in the end plates. Inside the end plates, G10 boards with copper-etched field shaping patterns were glued to complete the field cage. The total weight of JET is about 90 kg including IDCs.

Table B.2: Parameters and performances of tracking chambers

JET	
Shape and Size	Cylindrical, 690 mmϕ $\times$ 1016 mm
Sense wires	W/Re (Au plated), 20 μmϕ, 256 wires
Wire spacing	8.0 mm (y), Staggering of $\pm$300 μm (x)
Potential wires	Al (Au plated), 200 μmϕ, 292 wires
Wire spacing	8.0 mm
Cathode wires	Al (Au plated), 200 μmϕ, 465 wires
Wire spacing	4.0 mm
Maximum sampling hits	48
Maximum drift length	86.25 mm
spatial resolution	135 μm (x), 4.0 cm (z)
IDC	
Shape and Size	Arc-shaped, R = 354-374 mm, $\lvert\phi\rvert < 78.8°$, L = 1016 mm
Sense wires	W/Re (Au plated), 20 μmϕ, 9/8 wires
Wire spacing	14.0°
Potential wires	Mo (Au plated), 120 μmϕ
Spatial resolution	140 μm (ϕ), 1.0mm (z)

B.3.2 Inner Drift Chambers

IDCs, located just inside the cryostat, provide hit positions in the z-direction with high precision through diamond-shaped vernier strip readout as well as in the azimuthal direction through drift time measurement. IDCs are arc- shaped drift chambers with identical double layer structure except for their dimensions. A schematic view of IDC is shown in Figure B.4 and main parameters are summarized in Table B.2.

Each chamber is composed of four composite panels. The endplate is common with JET. The skins of the composite panels, copper-plated GFRP sheets, electrically isolate the two layers. The sensitive volume of each layer is 10 mm thick and is divided into cells by alternately stretched sense and potential wires. The wires are fixed by the same feed-throughs as used in JET at an interval of 7.0° in azimuth for IDC, corresponding to a half-cell size of about 45 mm. The wire position in one layer is shifted by a half-cell pitch with respect to the other layer. By adopting this double layer configuration and making a coincidence of the two overlapping cells, the left- right ambiguity can be automatically resolved.

Field shaping strips of 1.5 mm in width are etched on the inner surface of the copper-plated GFRP sheet at a 3 mm interval. The strip pattern on opposite side of IDC layer is slightly shifted so that the direction of the electric field is tilted by 5.5° with respect to the drift (azimuthal) direction in order to compensate for the Lorentz angle arising from the magnetic field of 0.8 T.

Vernier-cathode-strip pairs of 6.3 mm width are etched on both sides of the sense wires. As shown in Figure B.5, each pair consists of a diamond-shaped inner strip and an outer strip with complementary shape. A cycle length of the pattern is 97 mm for inner layer and 113 mm for outer layer. The strip patterns on opposite sides are shifted by a quarter pitch along the z-direction to give a precise hit coordinate. There are four strips in total associated to a single sense wire, which are read out separately.

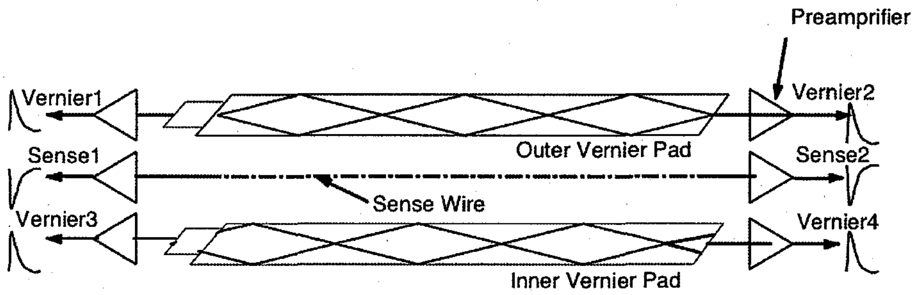

Figure B.5: Read-out scheme for IDC signals

B.3.3 Performance

The transverse and total rigidity of a particle is determined by fitting the three-dimensional hit positions measured by the drift chambers. Energy loss in the chamber gas is also measured using the charge information of the JET. To obtain hit position in r- plane, the drift velocity is calibrated using the flight data.

Rigidity Measurement

The JET and the IDCs determine the rigidity of a track. In the first step of the track reconstruction, if several consecutive hit points, which have enough charge and pulse width, are found inside JET, they are defined as segment. For each wire group, linear fitting is applied and left-right ambiguities are resolved comparing χ^2 of that fitting for hit position candidates at left and right sides. Next, out of every possible combinations of track segments, candidates of longtrackareextractedapplyinganalyticcircular fitting [45]. Then hit points near the sense wires which aren't included in segments are merged to the long track at this time if they are close enough. Hit points of IDCs are also merged after resolving left-right ambiguities in this step. These procedures are iterated with adding new hit points close to the track and dropping deviant ones.

In a similar way to the r-ϕ fitting, iterative fitting is applied in r-z plane to the selected hits in the JET and the IDCs. Since the IDCs provide only the z-positions within a vernier

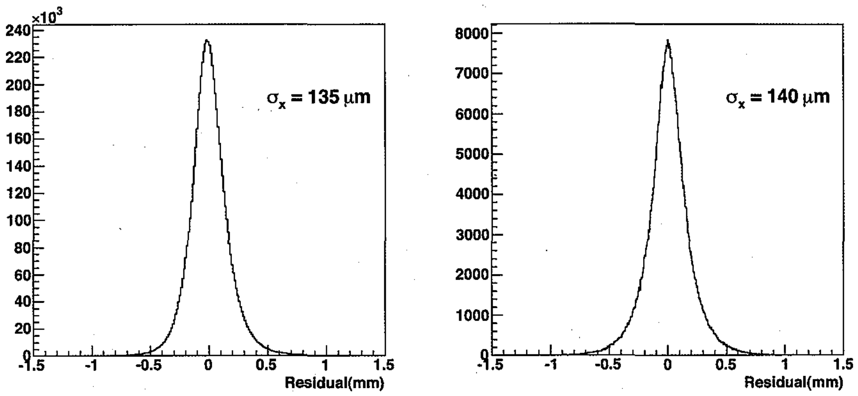

Figure B.6: Fitting residual for JET(left) and for IDC(right) in r-ϕ plane.

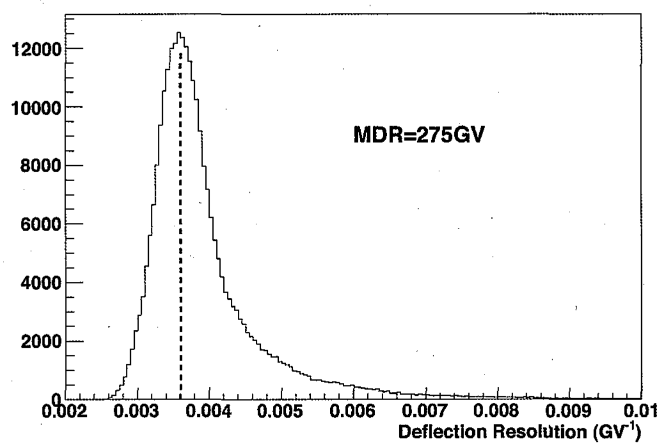

Figure B.7: Distributions of error in inverse of transverse rigidity during the flight.

strips pattern cycle of around 100 mm, all possible combinations are examined to find the true position which gives the minimum χ^2 value. Together with r-ϕ fitting, 3-dimensional tracks are reconstructed. finally.

The transverse rigidity, RT , is obtained by the r-ϕ fitting, and total rigidity, R, can be calculated as R = RT / cos θ. where θ is a dip angle defined as an angle between the total rigidity vector and r-ϕ plane. cosϕ was obtained from the z-component of the reconstructed 3-dimensional track.

Based on the residual distributions shown in Figure B.6, the overall spatial resolutions of the JET and the IDCs in r- plane are respectively estimated to be 135 m and 140 m. These position resolutions in r-ϕ plane of the tracking system enable transverse momentum measurement with a resolution of $\Delta p_T/p_T = 0.36 p_T(\mathrm{GeV/c})\%$, giving the maximum detectable rigidity (MDR) of 275 GV/c as shown in Figure B.7.

z-position Measurement

The z-coordinate of a hit position is obtained by using the charge division of the JET, and the vernier strip readout for the IDCs.

First we roughly determine hit positions along the sense wires of the JET by the charge division method. The z-coordinate of a hit position is derived from the charges read out at both ends of the hit wire (Q_a and Q_b). Hit position (z) is given by

$$\frac{z}{L} = \frac{(R+r)Q_b - rQ_a}{R(Q_a + Q_b)}$$

where L and R are the length and the resistivity of the sense wire and r is the input impedance of the preamplifier. We obtained the z-position resolutions of 37 mm for single-charged particles (left side of Figure B.8), by the JET.

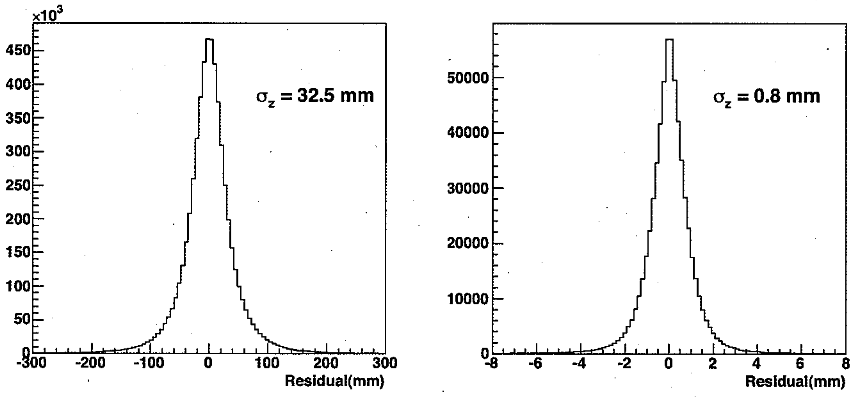

Figure B.8: Residual distribution of the JET and IDC along the z-coordinate

In combination with JET, we use the vernier strips of the IDCs to get the z-coordinate precisely. The hit position along the z-axis is measured using the signal charges induced on the associated vernier-strip pairs. We define a normalized charge ratio, ϵ, for a pair of vernier-strips, A and B.

$$\epsilon_{I(O)} = \frac{Q_{AI(O)} - Q_{BI(O)}}{Q_{AI(O)} + Q_{BI(O)}}$$

where $Q_{AI(O)}$,$Q_{BI(O)}$ denote the charges induced on A and B of the inner vernier-pad pair (outer vernier-pad pair). The ϵ parameters are linearly related to the z-axis position of the avalanche point. Figure B.9 shows a scatter plot of ϵ_I vs ϵ_O for the IDC vernier strips. A circuit along the round-square locus corresponds to a vernier-strip pattern cycle of 97 mm (113 mm) along the z-axis. We can derive the z-coordinate of a hit position by comparing a measured ϵ pair with the numerically calculated values. The deviations of the measured ϵ values from the calculated line are translated to the z-position resolution, giving the resolution of 0.8 mm by the IDC vernier strips as shown in right side of Figure B.8. The performance of the tracking system is summarized in Table B.2.

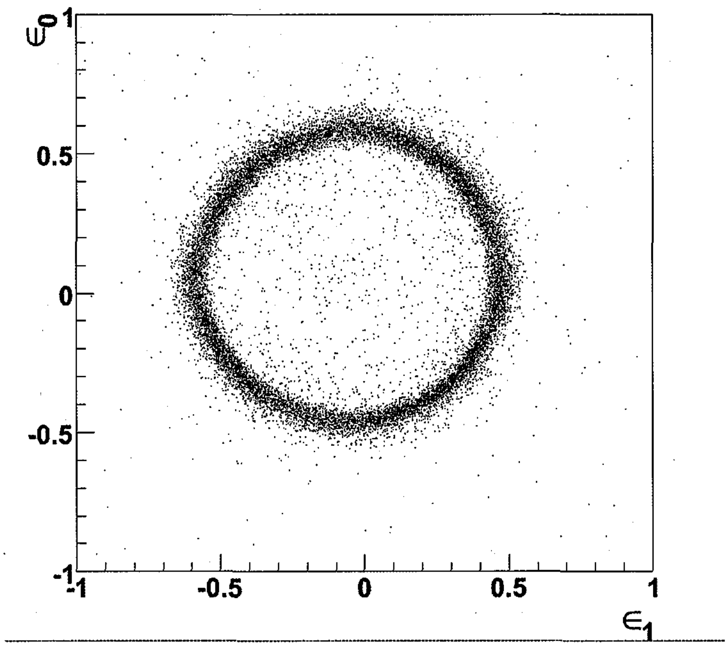

Figure B.9: Scatter plot of the ϵ parameter of the inner (ϵ_I) and outer (ϵ_O) pad.

Energy Loss Measurement

The pulse height measurement of the JET provides independent and redundant information as to particle identification. However, it was found that the dE/dx resolution of the JET deteriorates, particularly in the higher signal charge region, due to the space charge effect. After a detailed study of the effect, a correction method for saturation was obtained as follows.

The saturation strongly depends on the inclination angle ϕ_{y-z} between the track and the z-direction, and also slightly depends on the inclination angle $\theta_{r-\phi}$ of the track in the r-ϕ plane. Using pure helium and proton samples, the energy deposit is derived from the two-dimensional function of the θ_{y-z} and the measured charge, and then corrected for the $\theta_{r-\phi}$ dependence. The correction for the drift length is then applied to obtain the energy loss dE. In order to remove the Landau tail and delta ray effects, a truncated mean method is adopted. The points in lower 10 % and higher 20 % are eliminated, and the mean dE/dx is calculated using the rest of the hit points. Figure B.10 shows the dE/dx measured by the JET during the flight. We can clearly distinguish clusters of protons, muons/pions/electrons, deuterons, and heliums. The truncated mean method effectively removes the higher tail of the dE/dx distribution.

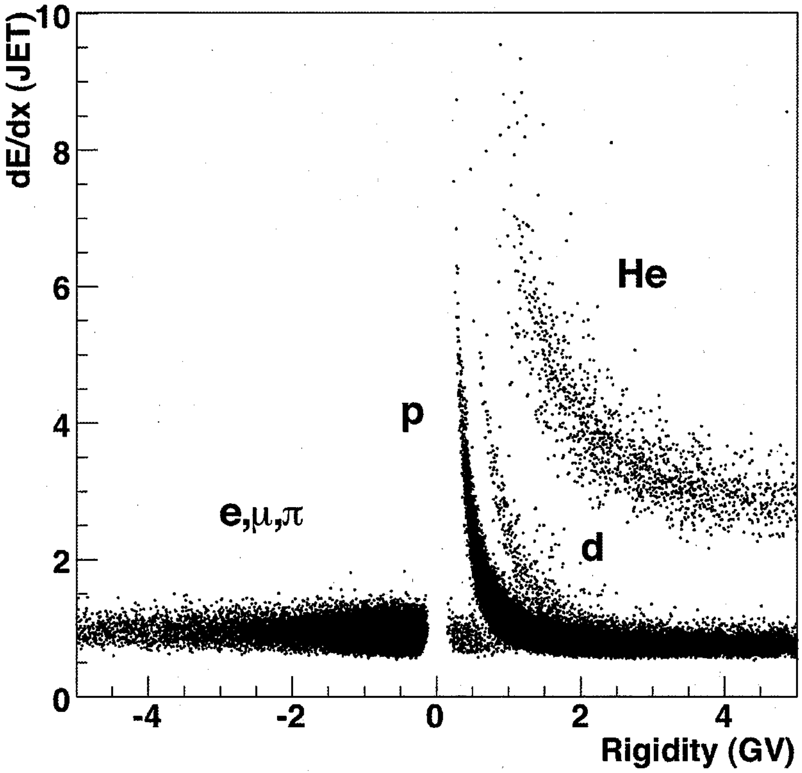

Figure B.10: dE/dx measurement by JET.

B.4 Time-of-Flight

B.4.1 TOF hodoscopes

The TOF hodoscopes consist of ten upper- and twelve lower- plastic scintillation counter paddles (945 × 100 × 12 mm, Eljen EJ-204). A lightguide (Figure B.11) made of UV-transparent acrylic plate(Mitsubishi Rayon) is affixed to the scintillator connecting each end of a counter to a 2.5-inch. fine-mesh magnetic-field-resistant photomultiplier tube (PMT), i.e., a Hamamatsu R6504S assembly type. To minimize the loss of photo-electrons in the PMT caused by the magnetic-field, PMTs are placed tangential to the acrylic plate such that the angle between their axis and magnetic field lines is minimized.

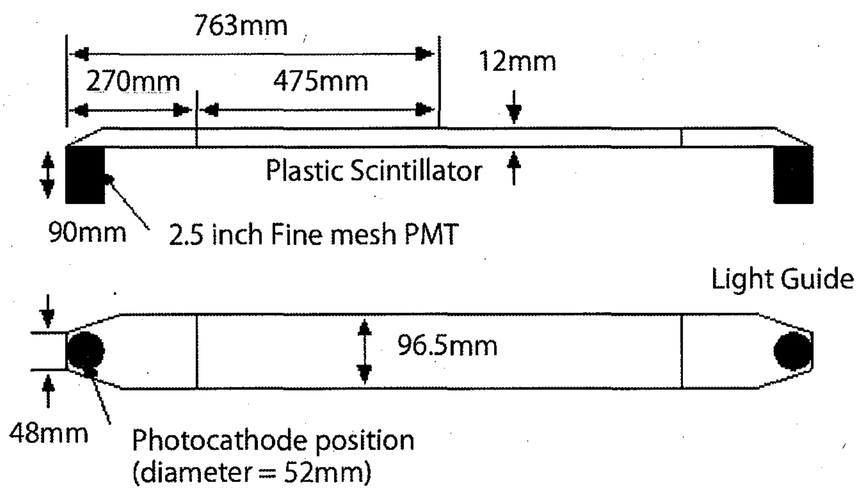

Figure B.11: Overview of a TOF counter for BESS-Polar.

The 2.5-inch FM-PMT (Hamamatsu R6504S) has the bi-alkali (Sb-Rb-Cs, Sb-K-Cs) photocathode of which the effective diameter is typically 52 mm. Electrons are accelerated by parallel electric fields between the dynodes; hence allowing the device to be used in a magnetic field if the direction of the magnetic field is parallel to the PMTs longitudinal axis. PMT and counters itself were placed in the vacuum since BESS-Polar spectrometer had no outer pressure vessel. The signal from the anode provides timing information and those from 13th and 18th dynodes are used to obtain the energy loss (dE/dx) of incident particles.

B.4.2 Electronics and signal Processing

The output signals from the counters were used for two different purposes: timing measurement and charge measurement. To avoid the interference in the electronics with each other, three signals extracted from the anode and dynodes (13th and 18th) were utilized for the above purposes, respectively.

The anode signals were used to issue START pulses for timing measurements, because they have the largest pulses suitable for the discrimination.

The time-to-digital converter (TDC) incorporate fast discriminators and common-stop time digitizers directly coupled to the anodes of PMT and measure arrival time of signals from TOF.

Threshold levels were set to 12 mV, that are about 1/60 compared to the anode pulse-heights of minimum ionizing particles (MIPs). TDC modules had a full range of 150 nanoseconds and a resolution of better than 43 picoseconds.

Every 13th and 18th dynodes signal is distributed, to the charge-to-digital converters (QDC), and integral charge of them were measured.

B.4.3 Principle of timing measurement

We discuss here on the hit time of a particle and time-of-flight, i.e., its difference between upper and lower layers of TOF counters of the BESS spectrometer including the details of their deriving processes. In the following discussion, PMTs number are assigned 1 and 2 as shown in Figure B.12.

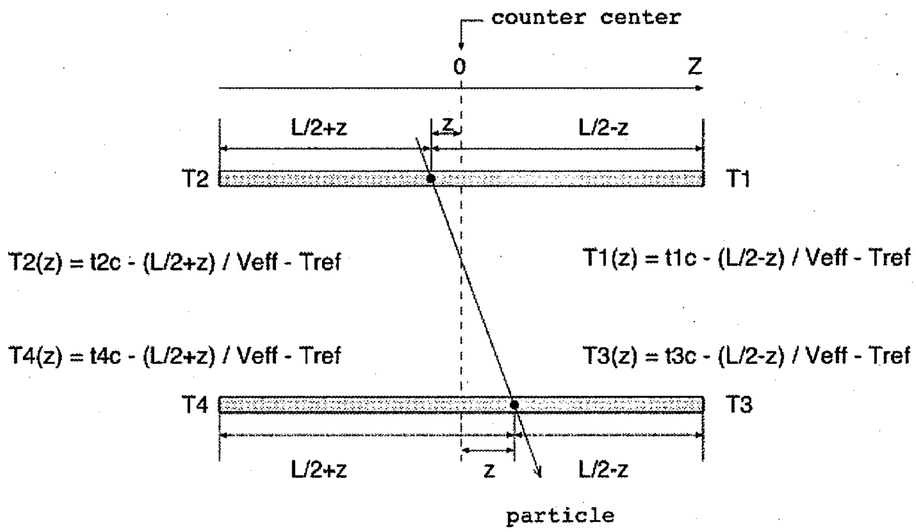

Figure B.12: The definition of z coordinate and hit time.

PMT signals have the time jitter associated with pulse heights, so called the 'time-walk' effect. Therefore the measured TDC time must be corrected for the time-walk effect (the time-walk correction). The time-walk corrected timing for PMT i, tic is expressed as,

$$t_{ic} = t_i - W_i/\sqrt{q_i} \tag{B.1}$$

where t_i, q_i and W_i are respectively the measured TDC time, the measured charge of the PMT signal, and a correction parameter fitted from data. Using the time-walk corrected timings for each PMT, we then define the hit time based on the hit position and the timing information. The hit position of the counter is defined using z coordinate along the counter's longitudinal direction as shown in Figure B.12 where the counter center is defined as z = 0. The hit time of a particle in this paper is the timing based on the reference timing, Tref which is subtracted as the offset timing and determined by the TDC common stop. We define the hit time for PMT1,2 of a counter, T1(z) and T2(z) to be

$$T_1(z) = t_{1c} - \left(\frac{L}{2} - z\right)/V_{\text{eff}} - T_{\text{ref}} \tag{B.2}$$

$$T_2(z) = t_{2c} - \left(\frac{L}{2} + z\right)/V_{\text{eff}} - T_{\text{ref}} \tag{B.3}$$

where $t_{1c,2c}$, and T_{ref} are respectively the time-walk corrected timings, reference timings; while z is the hit position of the counter, L the length of the counter including light guides, and V_{eff} the effective velocity of light in the scintillator. The measured rms of $T_1(z)$ and $T_2(z)$ are denoted as σ_1, σ_2, respectively. We use $1/\sigma_1^2$ and $1/\sigma_2^2$ as the weight of the combination of $T_1(z)$ and $T_2(z)$, respectively, for hit time measurements.

We then construct the weighted average of hit time measurements, $T_{w.a}(z)$ as follows:

$$T_{\text{w.a}}(z) \equiv \frac{T_1(z)/\sigma_1^2 + T_2(z)/\sigma_2^2}{1/\sigma_1^2 + 1/\sigma_2^2} \tag{B.4}$$

For upper and lower TOF counters of the BESS spectrometer, the hit times are calculated as combined timing of two PMTs of a TOF counter by using Eq.(B.4) together with z-position. The TOF of the BESS spectrometer obtained from the data for TOF counter PMTs, Ttof , is expressed as,

$$T_{\text{tof}} = T_L - T_U \tag{B.5}$$

where T_U and T_L are weighted averages (Eq. (B.4)) of the upper and lower layers of TOF counters, respectively.

B.4.4 Performance of TOF System

TOF data were analyzed with incident angle correction of the QDC counts using scintillator path length, time-walk correction, and correction of timing z-dependence.

Figure B.13 shows the ΔT distribution fitted by pure Gaussian resolution function with no tail. The ΔT is the difference between the TOF obtained from the data of TOF PMTs, $T_{\rm tof}$ (Eq. (B.5)), and the TOF expected from the tracking information, $T_{\rm trk}$, i.e.,

$$\Delta T = T_{\rm tof} - T_{\rm trk} \tag{B.6}$$

$$T_{\rm trk} = \frac{L}{c}\beta_{\rm trk}(R,m) = \frac{L}{c}\frac{p}{E} = \frac{L}{c}\sqrt{(ZR)^2/((ZR)^2+m^2)} \tag{B.7}$$

where L is the path length of the incident particles from upper to lower layer, Z the electric charge of the incident particles, R the rigidity of the incident particles, and c the velocity of light. Due to the error in R being small, the error in $T_{\rm trk}$ (Eq. (B.7)) is also small and the rms of ΔT represents the resolution of the TOF hodoscopes.

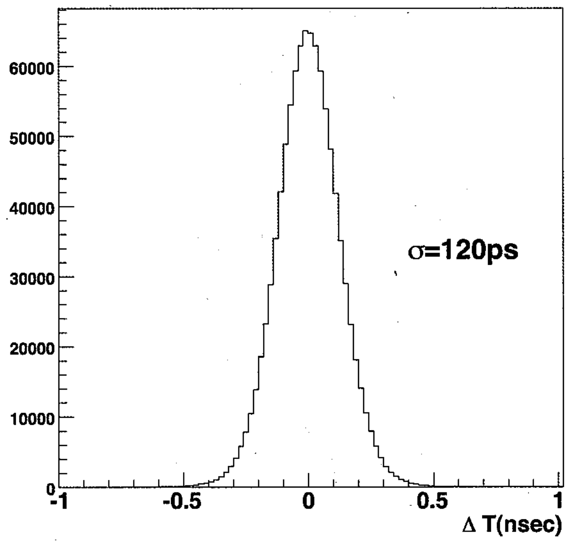

Figure B.13: The ΔT distribution of Upper TOF and Lower TOF for BESS-Polar II.

B.4.5 dE/dx measurement

QDC data were normalized for the gains of the PMTs and the QDCs after subtracting its pedestals. The dE/dx in a scintillator was obtained from the average of each PMT signals which was calculated by dividing by the transverse length in the scintillator and by correcting for the attenuation of light in the scintillator. Figure B.14 shows scatter plot of dE/dx versus rigidity measured in the chambers for each scintillators.

B.4.6 Middle TOF counter

In addition to the upper and lower TOF counters, a newly developed thin detector, the so called middle-TOF (MTOF), was installed on the lower half of the solenoid bore to detect low energy particles. This MTOF consists of 48 plastic scintillator bars. Each bar has a cross section of 5.6×13.3 mm read by eight anode photomultipliers (Hamamatsu R6504MODX-M8) through light guide of clear fiber (KURARAY CLEAR-PS 1.0 mm SQ) from double end.

Dynode signals are coupled to the TDC modules through an inverting amplifier with a gain of ten and bandwidth of more than 1 GHz. To reduce the power consumption of electronics, dynode signals of consecutive 8 scintillator bars are read out together while anode signals are individually coupled to the QDC modules. Other features, signal processing or principal of timing measurement are same as upper and lower TOF counters.

The signals from MTOF is fed into the trigger system as a substitute for the lower TOF's signal in the lower energy region. The BESS-Polar II spectrometer keeps sensitivity for the lowest energy antiprotons, down to 0.1 GeV, which stop at MTOF counter after penetrating 4.5 g/cm^2 material of the upper half of the spectrometer.

Figure B.15 shows the ΔT of middle TOF counter in the relativistic energy region, and Figure B.16 shows scatter plot of dE/dx versus rigidity in the middle TOF counter.

The development of MTOF is shown in chapter 4 and the detail of performance is shown in chapter 6.

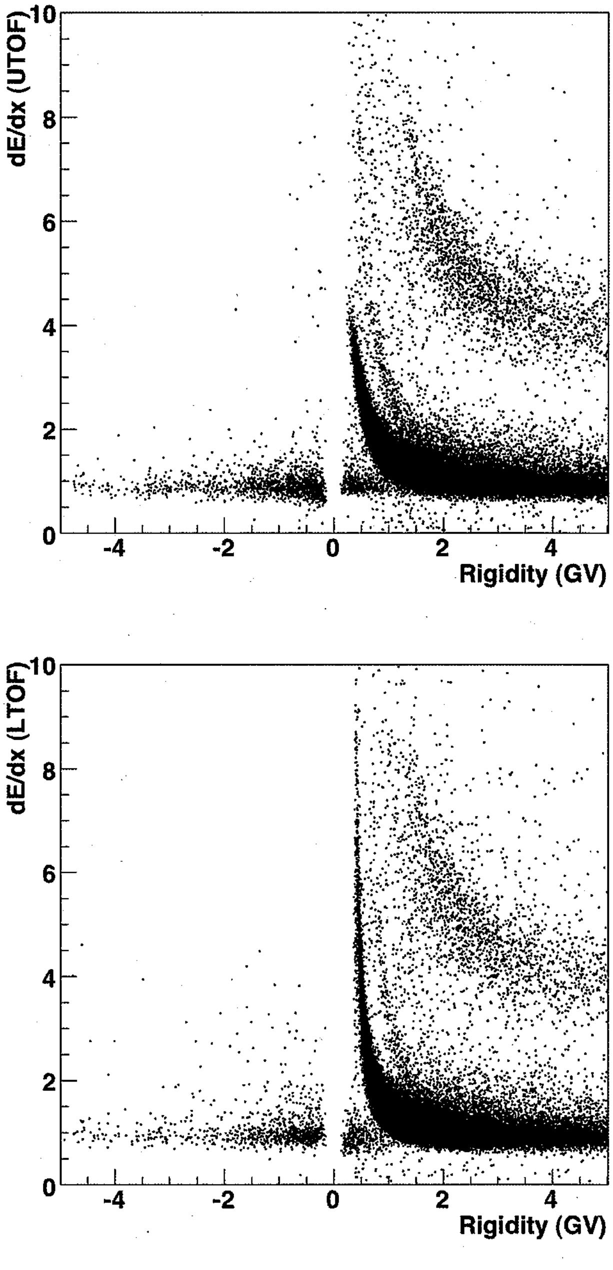

Figure B.14: dE/dx measurement by Upper TOF and Lower TOF

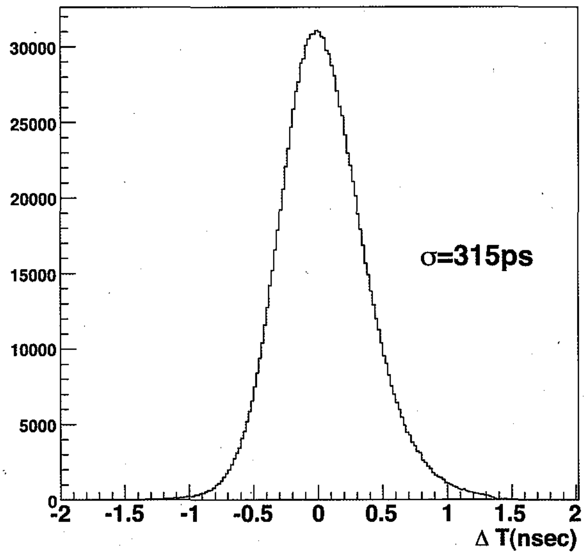

Figure B.15: Δ T distribution of UTOF and MTOF configuration.

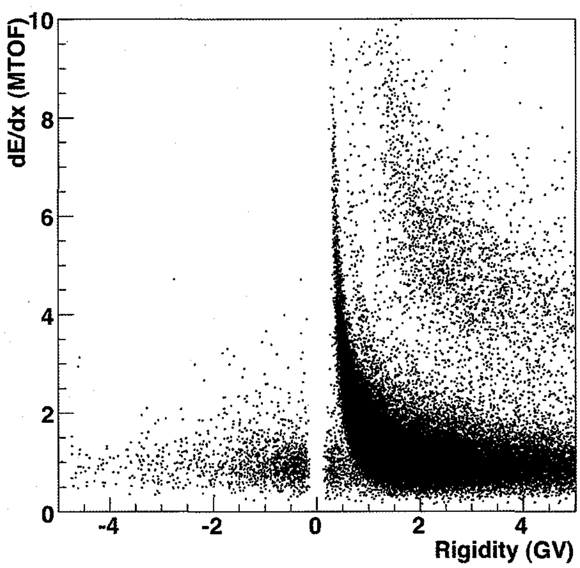

Figure B.16: dE/dx measurement by MTOF

B.5 Aerogel Cherenkov Counter

A Cherenkov counter with a silica aerogel radiator (aerogel Cherenkov counter) has been developed in order to improve particle identification capability.

The counter consists of a large diffusion box containing aerogel blocks viewed by 48 PMTs densely arranged at the both ends. Figure B.17 shows the inside of the diffusion box without readout PMTs. The top and bottom of the diffusion box were covered with the Carbon Fiber Reinforced Plastic (CFRP) plate to reduce the material in the area where incident particles pass through. The unit's weight and the amount of material were minimized using an thin aluminum plate as the main structure. In consideration of operating the counter in a 0.2-T fringe magnetic field, 2.5-in. FM PMTs were used, the same as the TOF hodoscopes. As a Cherenkov radiator, we selected silica aerogel having a refractive index of 1.03 [46].

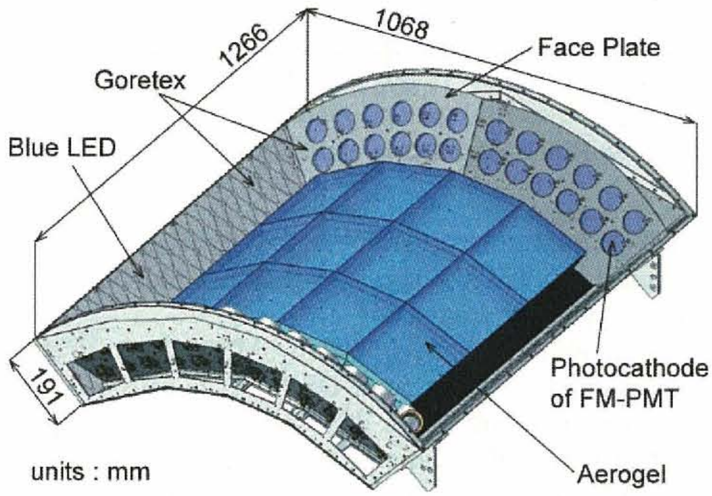

Figure B.17: Overview of the Aerogel Cherenkov counter.

B.6 Data Acquisition System

In the BESS-Polar experiment, owing to the large storage space of 16 Tbytes of HDD, no event selection was needed during the flight. Figure B.18 shows the BESS-Polar DAQ system.

The time-to-digital converter and discriminator modules (TDC/Discriminator) discriminate signals from TOF and MTOF, and send hit patterns of those detectors to a trigger boards. The trigger board generates event trigger in accordance with those hit patterns. A trigger signal is sent to all other modules to start data digitization. Charge of incident particles in TOF/ACC/MTOF are digitized by charge-to-digital converter (QDC) modules.

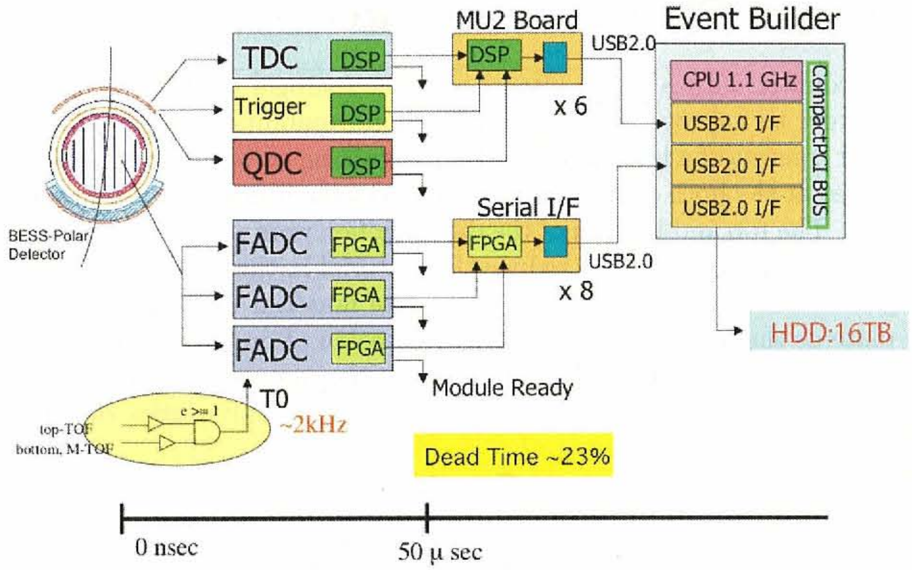

Figure B.18: Block diagram of the BESS-Polar II DAQ system.

These modules (TDC/Discriminator, ADC, and Trigger) have a digital signal processor (DSP) units on each board (TI TMS320) so that they can individually proceed digitization processes and prepare for the next trigger.

All data from these modules are assembled by MU2 (McBSP to USB 2.0 converter) modules. A MU2 module receives data from DSPs via multichannel buffered serial ports (McBSPs), and then transmit them to the data processing part via USB 2.0. Data from JET/IDC are sent to FADC modules and sent to the next data processing part.

Acquired data from MU2 and FADC are processed by DAQ programs on the Compact-PCI boards, and in here the event data are finally constructed. All cosmic-ray event data which issue trigger during the flight are stored on 16 hard disk drives, with a capacity of 1 TB. Compact- PCI boards are also connected to the following communication boards by TCP/IP to transfer some event data to the ground station.

B.6.1 Communication Subsystem

The communication subsystem manages communication between the payload and the ground station by a satellite link. Commands from the ground station are received by a PC/104 based system via the Support Instrument Package (SIP), and are sent to all other modules after interpretation. Some of event data are also sent to the ground station via the SIP.

B.6.2 Monitor Subsystem

The monitor subsystem handles the monitor-data which are sent from various sensors distributed in the payload for house-keeping purpose. The transducers generate voltage outputs according to the measured values of temperature, pressure and altitude of the payload. In the flight we monitored temperatures, pressures, a magnet status, a chamber high voltage status, high voltage status of TOF and Cherenkov counter PMTs in the vacuum and the GPS receiver and clinometers. The data are transmitted to the ground station and are utilized to monitor and check the detector status during a flight. They are also recorded on the HDD for the off-line analysis.

B.6.3 Scheme of communication using satellites

During the flight, we could communicate with payload by sending the command from the ground station for the control of detectors. For this communication, we used two satellite lines (TDRSS and Iridium) and line-of-sight (LOS) communication, and TDRSS lines was mainly used for the monitoring and sending commands after payload went out of LOS range. Figure B.19 and Table B.3 shows the feature of these three communication lines.

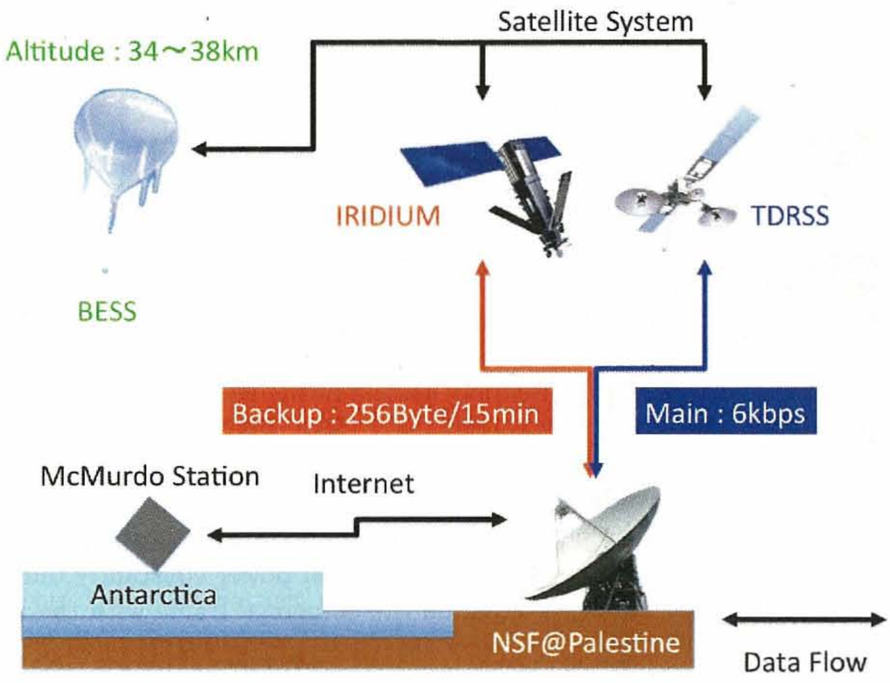

Figure B.19: Schematic view of communication system during the flight.

Table B.3: Summary of communication system during the flight.

Link	TDRSS	Iridium	LOS
Uplink	Scheduled	Backup	
Downlink	6 kbps	255 bytes/15min	83.33 kbps

B.7 Power Distribution System

B.7.1 Solar-Battery System

A solar battery system is adopted to provide electric power for the frontend electronics and data acquisition system, since the primary lithium battery used the BESS flights before BESS-Polar I flight are too heavy to maintain all power consumption for more than 20 day. On the other hand, in the summer at Antarctica, there are nights with the midnight sun and payload can always see the sun. So a solar battery system can work efficiently as a stable power sources. Figure B.20 shows the schematic view of the power supply system in the previous BESS and BESS-Polar respectively.

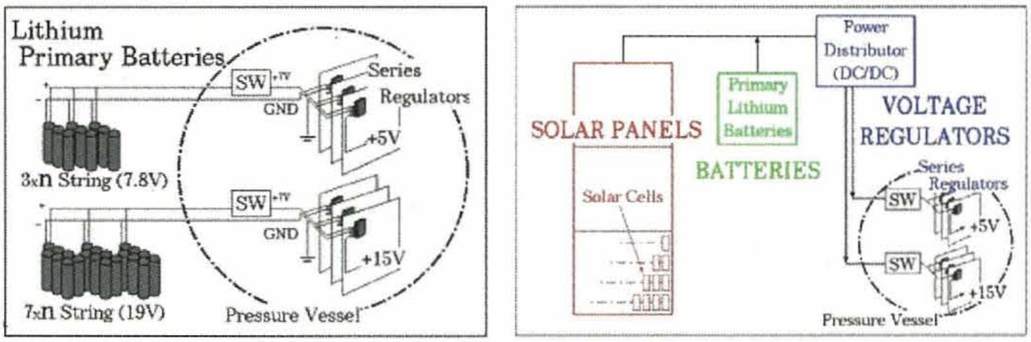

Figure B.20: Schematic view of power supply system in the BESS flight (left) and the BESS-Polar II flight (right).

For the safe operation, we didn't adopt the pointing system of solar battery panel for the sun, but ninety solar battery panels are mounted on a omni-directional octagonal frame around the payload. They can provide 450 W electrical power constantly during the flight. Figure B.21 shows the solar battery system on the octagonal frame with the BESS-Polar II payload.

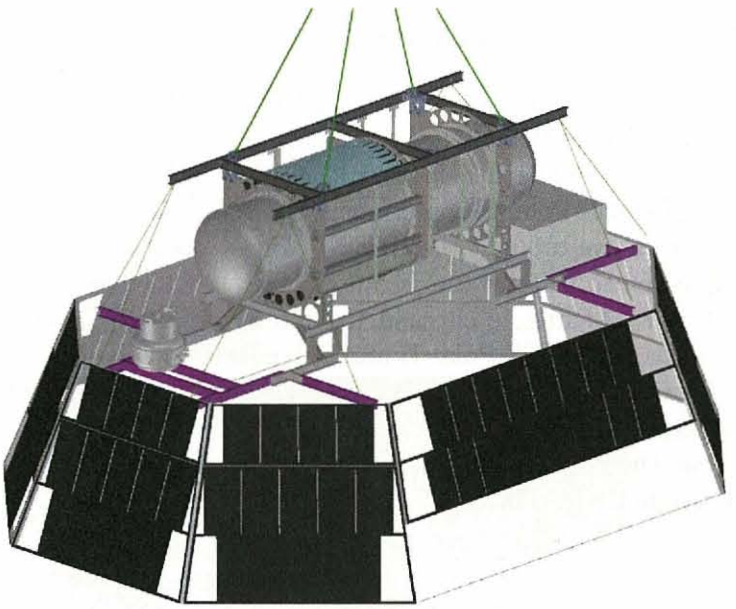

Figure B.21: Schematic view of Solar Battery System.

B.7.2 Primal batteries

Though solar battery system is adopted for the power source, a bank of primary (non-rechargeable) lithium batteries (Eternacell sulfur dioxide cells) to drive BESS-Polar spectrometer for only 12 hours are also mounted as insurance against the accidents, such as the lost of the one third of the solar battery panels on a side by the shock of the launching or accidents during the flight. They have high energy density (~35 Ah / 300 g), high current capability (3 A continuous), wide operating temperature range (-40 to 85°C) and relatively stable output voltage (-2.8 V). Battery cells were stacked in series to comply with voltage requirements of the electronics. Battery packs with 16 cells in series were used for 40 V supply allowing for some voltage drop of the battery and the voltage drop in regulators and cables.

B.7.3 DC-DC converter

The power from the solar battery are fed to the power bus lines of the dedicated crates after conversion into the proper voltages by the DC-DC converter system inside the shield box. This system consists of DC-DC converter of VICOR VI-J series which has a converting efficiency of 70-80 %. Since the DC-DC converter is strongly affected by magnetic field, it was installed as far as possible from the solenoid. The magnetic field at the position was about 70 Gauss.

B.8 Integration of BESS-Polar II spectrometer

In this section, we introduce the short history of BESS-Polar II experiment.

Each component of BESS-Polar II spectrometer was developed in Japan and USA from January, 2005. We integrated each detectors in NASA/GSFC from Jan 2007. Figure B.22 shows the progress of BESS-Polar II experiment.

After the integration, we brought the BESS-Polar II spectrometer to Columbia Scientific Balloon Facility (CSBF) to acquire the permission of balloon flight over Antarctica. There were two test in CSBF. At first, e checked the integration of BESS-Polar II spectrometer between the magnet part of BESS-Polar II and Solar-Battery system. Figure B.23 shows the schematic view of integration for BESS-Polar II spectrometer. After that, we checked the compatibility between BESS-Polar spectrometer and the equipment to attach the balloon. The second test was the communication system between BESS-Polar II spectrometer and satellite with the magnetic field of BESS-Polar II spectrometer.

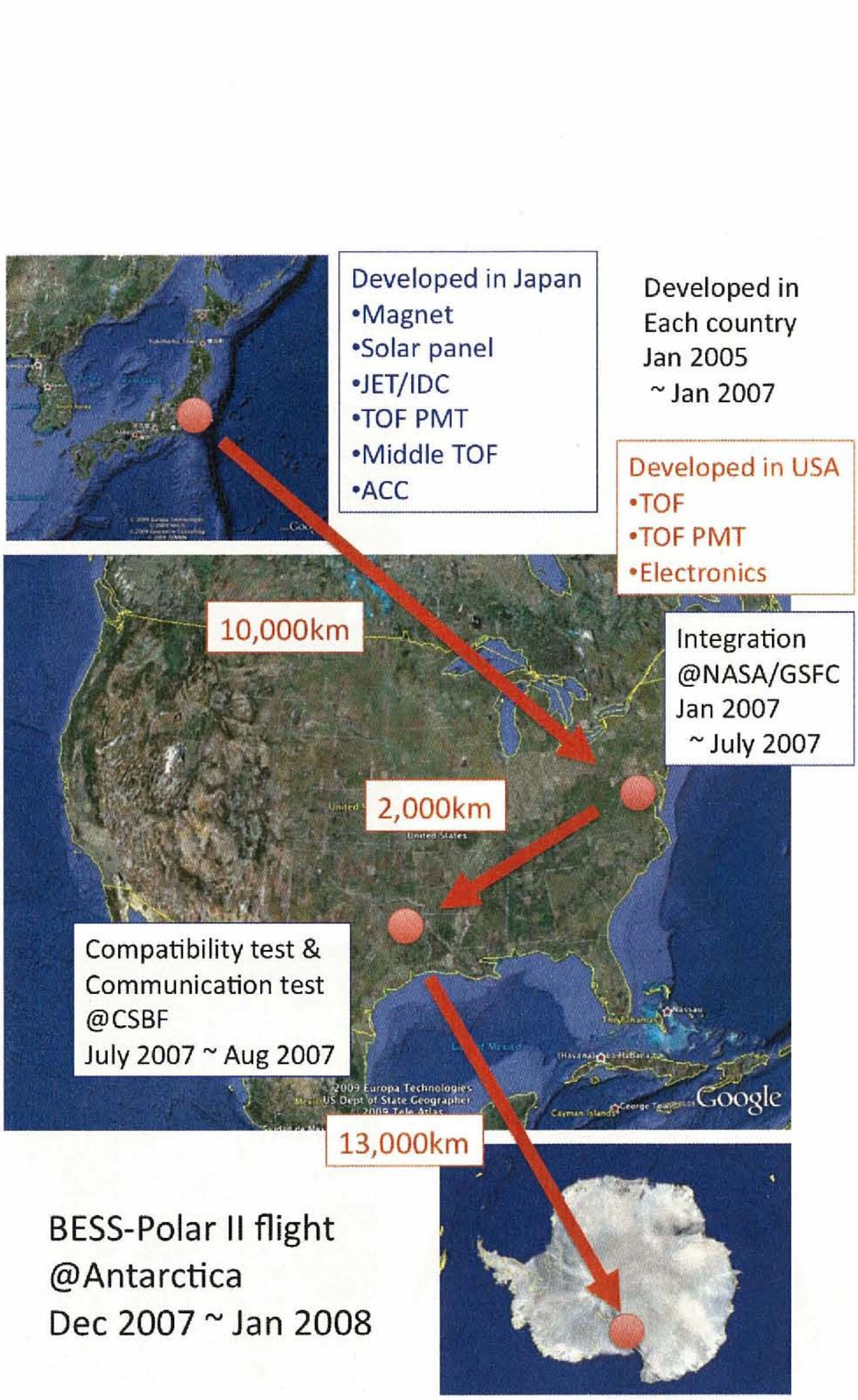

Figure B.22: The progress of BESS-Polar II experiment.

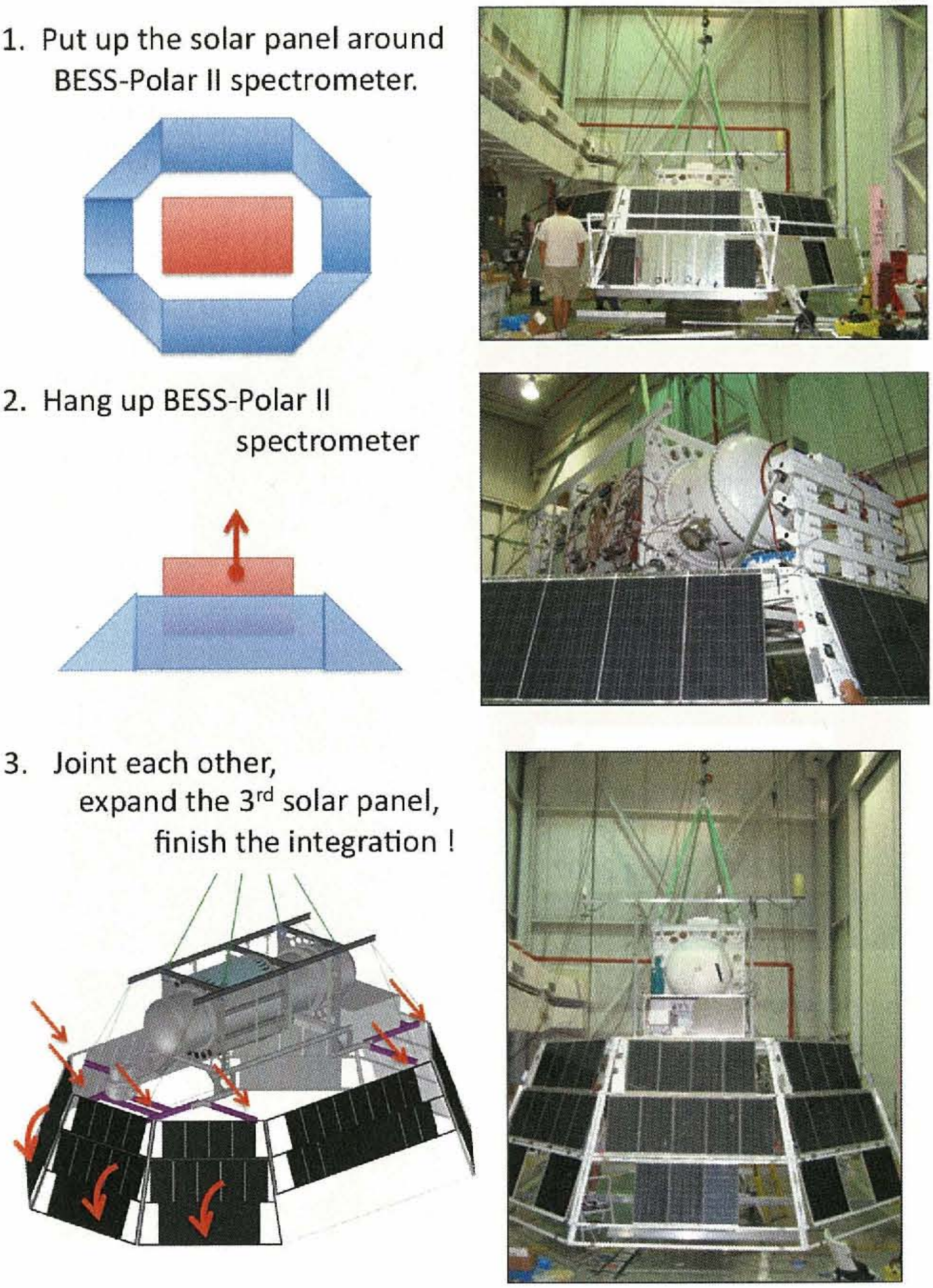

Figure B.23: The integration scheme of BESS-Polar II spectrometer with photos of actual work.